


Spring 2015

Catalysis of Stark-Tuned Interactions Between Ultracold Rydberg Atoms

Aye Lu Win
Old Dominion University

Follow this and additional works at: https://digitalcommons.odu.edu/physics_etds

 Part of the [Atomic, Molecular and Optical Physics Commons](#), and the [Quantum Physics Commons](#)

Recommended Citation

Win, Aye L. "Catalysis of Stark-Tuned Interactions Between Ultracold Rydberg Atoms" (2015). Doctor of Philosophy (PhD), dissertation, Physics, Old Dominion University, DOI: 10.25777/dj2f-9r86
https://digitalcommons.odu.edu/physics_etds/94

This Dissertation is brought to you for free and open access by the Physics at ODU Digital Commons. It has been accepted for inclusion in Physics Theses & Dissertations by an authorized administrator of ODU Digital Commons. For more information, please contact digitalcommons@odu.edu.

**CATALYSIS OF STARK-TUNED INTERACTIONS
BETWEEN ULTRACOLD RYDBERG ATOMS**

by

Aye Lu Win
B.A., Simpson College, 2005
M.S., Old Dominion University, 2008

A Dissertation Submitted to the Faculty of
Old Dominion University in Partial Fulfillment of the
Requirements for the Degree of

DOCTOR OF PHILOSOPHY

PHYSICS

OLD DOMINION UNIVERSITY
May 2015

Approved by:

Charles I. Sukenik (Director)

Jozef Dudek (Member)

Alexander L Godunov (Member)

Svetozar Popovic (Member)

John Tweed (Member)

ABSTRACT

CATALYSIS OF STARK-TUNED INTERACTIONS BETWEEN ULTRACOLD RYDBERG ATOMS

Aye Lu Win

Old Dominion University, 2015

Director: Dr. Charles I. Sukenik

We present the study of the catalysis effect in the resonant energy transfer between ultracold ^{85}Rb Rydberg atoms. We have investigated the energy transfer process of $34p + 34p \rightarrow 34s + 35s$, and observed Stark-tuned Förster resonances. When additional Rydberg atoms of $34d$ state are included in the interaction, an increase in the population of $34s$ states atoms is observed. Although the $34d$ state atoms do not directly participate in the resonant energy transfer that produces $34s$ state atoms, they add an additional interaction channel $34p + 34d \rightarrow 34d + 34p$ that is resonant for all electric fields. We have also investigated the time dependence of the resonant interactions of $34p + 34p \rightarrow 34s + 35s$, compared the experimental results with the numerical simulations of simple models, and found them to be in good agreement.

Copyright, 2015, by Aye Lu Win, All Rights Reserved.

To May May Daw Khin Aye and Phay Phay U Tin Maung Ohn for your love and support, for all that I have learned and continue to learn from you.

ACKNOWLEDGEMENTS

I would like to thank my advisor Dr. Charles I. Sukenik for giving me the opportunity to work with him. This work would not have been possible without his guidance, understanding and enthusiasm for the experiment. I would like to thank Dr. Will Williams for his enthusiasm for the experiment. I would also like to thank my dissertation committee members Dr. Jozef Dudek, Dr. Svetozar Popovic, Dr. John Tweed, and Dr. Alexander L. Godunov for their insightful discussions. I would like to thank Dr. Dodge and Dr. Vuskovic for their invaluable leadership. I would like to express my thanks to Dr. Havey for giving me my first opportunity to work in an ultracold atomic laboratory. I would also like to thank Dr. David Olsgaard for his enthusiasm for physics, and for giving me my first key to a laboratory where I enjoyed spending hours, and also for the wonderful times with his family while I was in Simpson College. I would like to express my gratitude to Dr. Lora Friedrich for being such a wonderful host mom, and for everything. I would like to thank Dr. Melvin Wilk (R.I.P.) for his wisdom and friendship. I would like to thank Dr. Yan Lwin for his guidance and support while I was in Western Illinois University.

I would like to thank my senior colleagues Dr. Gambhir Ranjit, Dr. Eman Mohammed Ahmed, Dr. Rocio Gisel Olave, and Dr. Salim Balik for their patience with my questions and giving me their valuable time, and their friendship.

I would like to thank my fellow members of the group Jack Mills, Maha Omar, and Grady White for being a part in this endeavor. I would especially like to thank Jack Mills for his friendship, assistance whenever needed, and his expertise in LabVIEW. I would like to thank Janardan Upadhyay along with Jack and Mr. Do Im for his friendship and also being a member of our coffee club. There are many to thank in this rather long journey. I would like to thank Dr. Subashini Uddika De Silva, Dr. Senthil Raja, Dr. Bill Ford, Dr. Michael Mayer, Dr. Christopher Hopper, Dr. Ana Samolov, Dr. Milka Nikilic, Milos Basovic, Dr Suman Koirala, and Dr. Kurnia Foe for their friendship. I would like to express my thanks to Ms. Lisa Okun, Ms. Delicia Malin, and Ms. Annette Guzman-Smith and Mr. Walt Hooks for running things smooth for us.

I am thankful for the Myanmar community here in Norfolk for making me feel at home. I thank Dr. Khin Thitsar, Dr. Khin Maung Maung and Dr. Ei Ei Brown for their infectious enthusiasm for research and their friendship. I would like to thank

the families of Daw Shwe Ye Win, Daw Thet Maw Maw, and Dr. Tin Han Htwe for always welcoming me.

I am deeply thankful to Dr. Khin Oo and U Zaw Myint for being the family away from the family and for everything over all the years. I have truly been fortunate to know you. I am thankful for having brothers Wai Phyo Lin and Aung Naing Own, and sister Phyo Thinzar, and for being a part in your lives. You have enriched my life. I could not possibly express my deepest regards for May May Daw Khin Aye and Phay Phay U Tin Maung Ohn for your unrelenting metta.

TABLE OF CONTENTS

	Page
LIST OF TABLES	viii
LIST OF FIGURES	ix
 Chapter	
1. INTRODUCTION	1
2. THEORETICAL BACKGROUND	6
2.1 RYDBERG ATOMS	6
2.2 STARK STRUCTURE OF RYDBERG ATOMS	8
2.3 INTERACTION OF RYDBERG ATOMS	14
2.4 LASER COOLING AND TRAPPING OF ATOMS	20
3. EXPERIMENTAL SETUP FOR CREATION AND DETECTION OF RYD- BERG ATOMS	27
3.1 VACUUM SYSTEM	27
3.2 CREATION OF RYDBERG ATOMS	27
3.3 DETECTION OF RYDBERG ATOMS	35
4. RESULTS AND ANALYSIS	54
4.1 OBSERVATION OF STARK-TUNED FÖRSTER RESONANCES ...	54
4.2 CATALYSIS OF STARK-TUNED INTERACTIONS	59
4.3 MODELS FOR RESONANT ENERGY TRANSFER PROCESS	73
5. CONCLUSION AND OUTLOOK	80
 BIBLIOGRAPHY	80
 VITA	87

LIST OF TABLES

Table	Page
1. Quantum defect parameters for ^{85}Rb	7
2. Properties of Rydberg atoms. Adapted from [53].	8
3. The CODATA recommended values for selected physical constants in Hartree atomic units and SI units [57].	9
4. Rubidium 85 Physical Properties [74].	24
5. The values of electric fields for the Förster resonances.	56

LIST OF FIGURES

Figure	Page
1. Stark structures of ^{85}Rb for $n=34$	11
2. Schematic diagram of two interacting dipoles separated by a distance R	14
3. Schematic diagrams of the energy levels of atomic states and two-atom or pair states (not to scale). In the atomic state basis, the states are coupled by the dipole matrix elements μ_1 and μ_2 . Transforming the atomic state basis into the pair state basis reveals two states that are almost degenerate with a small energy difference Δ called Förster defect.	15
4. Stark structure of ^{85}Rb showing the dipole-coupled states of $34s_{1/2}$ and $34p_{3/2}$ with the dipole matrix element μ_1 and $34p_{3/2}$ and $35s_{1/2}$ with the dipole matrix element μ_2 . The energy level of $34p_{3/2}$ lies midway between $34s_{1/2}$ and $35s_{1/2}$ at the field of 5.83 V/cm.	18
5. Stark shift of the dipole-coupling allowed pair states $34s_{1/2} + 35s_{1/2}$ and $34p_{3/2} + 34p_{3/2}$, neglecting dipole-dipole interaction between them. Level crossing occurs at zero Förster defect.	19
6. The energy shifts for the resonant dipole interaction of $34p_{3/2} + 34p_{3/2} \rightarrow 34s_{1/2} + 35s_{1/2}$ vs. Förster defect. The resonant dipole interaction energy $\mu_1\mu_2/R^3$ is ~ 9.2 MHz for the distance between atoms of 5 μm	20
7. Doppler cooling scheme. (a) Two-level atom model, ω_0 is the resonant angular frequency of the transition and ω_{laser} is the angular frequency of the laser tuned lower than ω_0 . (b) In the laboratory frame the atom is moving toward one of the counter-propagating laser beams and away from the other. (c) In the atom's rest frame the frequency of the beam from the left appears higher than ω_0 (blue shifted), and the frequency of the beam from the right appears lower than ω_0 (red shifted).	21
8. The principle of magneto-optical trapping [69].	24
9. The energy levels of ^{85}Rb for magneto-optical trapping. Adapted from [74].	26
10. Schematic diagram of the top view of the vacuum system for the magneto-optical trap.	28
11. External cavity diode laser in Littman-Metcalf configuration (not to scale).	29

12.	Schematic layout of laser systems for the magneto-optical trap. AOM stands for acousto-optic modulator, and $\lambda/2$ and $\lambda/4$ represent half-wave plate and quarter-wave plate, respectively.	30
13.	Rydberg excitation scheme: excitation to $34P$ state directly from the ground state with 297.7 nm pulsed laser light, and to $34D$ state by the two-step excitation of $5S_{1/2} \rightarrow 5P_{3/2}$ with 780nm, and $5P_{3/2} \rightarrow 34D$ with 481.4 nm pulsed laser light respectively.	32
14.	Tuning curve of Continuum ND6000 laser with Rhodamine 6G dye.	33
15.	Dye laser energy vs. pump laser energy.	33
16.	The output laser energy from the frequency doubling crystal vs. the input laser energy.	34
17.	Schematic drawing of homebuilt dye laser in Littman configuration [76]. .	34
18.	Tunable homebuilt dye laser.	35
19.	The schematic diagram of the optical setup of the laser systems for excitation of Rydberg states. $\lambda/2$ stands for half-waveplate.	36
20.	Schematic diagram of the optical setup for fluorescence detection.	39
21.	A partial Rydberg spectrum of the nd series of ^{85}Rb obtained with the fluorescence detection method.	40
22.	Timing sequence for the trap loss spectroscopy for np series.	41
23.	A partial Rydberg spectrum of the np series of ^{85}Rb obtained with the fluorescence detection method.	41
24.	The output signal of the RC circuit for measuring its time constant. The circuit is used in ion detection by the field ionization method.	43
25.	Schematic diagram for the top view of the two configurations of electric field plates as part of the detection systems for Rydberg states by field ionization method (not to scale). (a) This field plates configuration was used in the first installation of ion detection system in the vacuum chamber. (b) The plates configuration for the second installation of ion detection system: steel plates were replaced with transparent wire meshes so that the separation between the plates can be made smaller for producing a uniform electric field between them.	44

26.	Time-resolved signals of Rydberg states detected by the field ionization method with plate separation of ~ 4.6 cm. Detection of lower Rydberg states was not possible with this field plate configuration.	45
27.	Time-resolved signals of lower Rydberg states detected by the field ionization method with the final configuration of the field plates that has a separation of ~ 1.35 cm between them.	46
28.	A partial Rydberg spectrum of the nd series of ^{85}Rb obtained with the field ionization method.	47
29.	Ion detection system before installation in the vacuum chamber. (a) The assembly for the channel electron multiplier. (b) The assembly of the plate used for field ionization of Rydberg atoms.	48
30.	Geometry of the ion detection system. The magneto-optical trap beams enter the central region of the vacuum chamber through the slots in the steel plates covered with transparent nickel mesh.	49
31.	Signals of the $45d$ state at various densities of the magneto-optical trap. The sharp signal at $198.2 \mu\text{s}$ is due to free ions. The trap density is varied with the intensity of the trap laser beams. The intensities from (a) to (f) are $\sim 9, 15, 20, 26, 30, 35,$ and 38 mW/cm^2 respectively.	51
32.	Signals of the $45d$ state at various energies of the excitation pulsed laser beam. The energies from (a) to (f) are $\sim 20, 30, 40, 60, 75,$ and $90 \mu\text{J/pulse}$ respectively.	52
33.	Experimental timing sequence (not to scale).	53
34.	Stark structures of the pair states. Förster resonances are observed at the fields where the level crossings occur.	55
35.	Time-resolved signals of Rydberg states for the process $34p_{3/2} + 34p_{3/2} \rightarrow 34s_{1/2} + 35s_{1/2}$. The signal in blue is for the resonant electric field, and the signal in red is for the non-resonant electric field.	56
36.	Förster resonance for the process $34p_{3/2, 1/2 } + 34p_{3/2, 1/2 } \rightarrow 34s_{1/2} + 35s_{1/2}$. The polarization of the excitation laser beam is set to be in the z direction.	57
37.	Förster resonances. The polarization of the excitation laser beam is set to be in the x direction.	58

38. The signals for $34d$ state for the interaction time of $7\mu s$. The signal in blue is for the electric field set to the resonant value for the process $34p_{3/2,|m_j|=1/2} + 34p_{3/2,|m_j|=1/2} \rightarrow 34s_{1/2} + 35s_{1/2}$. The signal in red is for a non-resonant electric field for the process. 60
39. The signals of Rydberg states $34d$ and $34p$ for the interaction time of $7\mu s$ in a non-resonant electric field. The signal in red is for the interaction without $34d$ state Rydberg atoms, and the signal in blue is for the interaction with $34d$ state Rydberg atoms included. 61
40. The signals of Rydberg states $34d, 34p$ and $34s$ for the interaction time of $7\mu s$ in the resonant electric field for $34p_{3/2,|m_j|=1/2} + 34p_{3/2,|m_j|=1/2} \rightarrow 34s_{1/2} + 35s_{1/2}$. The signal in red is for the interaction without $34d$ state Rydberg atoms, and the signal in blue is for the interaction with $34d$ state Rydberg atoms included. 62
41. Interaction time dependence of the $34s$ state population for the resonant energy transfer process $34p_{3/2,|m_j|=1/2} + 34p_{3/2,|m_j|=1/2} \rightarrow 34s_{1/2} + 35s_{1/2}$. The data in the symbol \times is for the process without the $34d$ state atoms included in the interaction, and that in symbol \blacklozenge is for the process with the $34d$ atoms in the interaction. 64
42. The correlation coefficient of the $34s$ state population with and without $34d$ included in the interaction vs. interaction time for the resonant energy transfer process $34p_{3/2,|m_j|=1/2} + 34p_{3/2,|m_j|=1/2} \rightarrow 34s_{1/2} + 35s_{1/2}$ 65
43. Ratio of the $34s$ state population vs. interaction time with and without $34d$ included in the interaction for the resonant energy transfer process $34p_{3/2,|m_j|=1/2} + 34p_{3/2,|m_j|=1/2} \rightarrow 34s_{1/2} + 35s_{1/2}$ 66
44. Interaction time dependence of the $34s$ state population for the resonant energy transfer process $34p_{3/2,|m_j|=3/2} + 34p_{3/2,|m_j|=1/2} \rightarrow 34s_{1/2} + 35s_{1/2}$. The data in the symbol \times is for the process without the $34d$ state atoms included in the interaction, and that in symbol \blacklozenge is for the process with the $34d$ atoms in the interaction. 67
45. The correlation coefficient of the $34s$ state population with and without $34d$ included in the interaction vs. interaction time for the resonant energy transfer process $34p_{3/2,|m_j|=3/2} + 34p_{3/2,|m_j|=1/2} \rightarrow 34s_{1/2} + 35s_{1/2}$ 68
46. Ratio of the $34s$ state population vs. interaction time with and without $34d$ included in the interaction for the resonant energy transfer process $34p_{3/2,|m_j|=3/2} + 34p_{3/2,|m_j|=1/2} \rightarrow 34s_{1/2} + 35s_{1/2}$ 69

47. Interaction time dependence of the 34s state population for the resonant energy transfer process $34p_{3/2,|m_j|=3/2} + 34p_{3/2,|m_j|=3/2} \rightarrow 34s_{1/2} + 35s_{1/2}$. The data in the symbol \times is for the process without the 34d state atoms included in the interaction, and that in symbol \blacklozenge is for the process with the 34d atoms in the interaction. 70
48. The correlation coefficient of the 34s state population with and without 34d included in the interaction vs. interaction time for the resonant energy transfer process $34p_{3/2,|m_j|=3/2} + 34p_{3/2,|m_j|=3/2} \rightarrow 34s_{1/2} + 35s_{1/2}$ 71
49. Ratio of the 34s state population vs. interaction time with and without 34d included in the interaction for the resonant energy transfer process $34p_{3/2,|m_j|=3/2} + 34p_{3/2,|m_j|=3/2} \rightarrow 34s_{1/2} + 35s_{1/2}$ 72
50. The experimental and simulation results for the time evolution of the fraction of 34s atoms for the energy transfer process $34p_{3/2,|m_j|=1/2} + 34p_{3/2,|m_j|=1/2} \rightarrow 34s_{1/2} + 35s_{1/2}$. The amplitude of the experimental data is scaled to fit. 76
51. The experimental and simulation results for the time evolution of the fraction of 34s atoms for the energy transfer process $34p_{3/2,|m_j|=3/2} + 34p_{3/2,|m_j|=1/2} \rightarrow 34s_{1/2} + 35s_{1/2}$. The amplitude of the experimental data is scaled to fit. 77
52. The experimental and simulation results for the time evolution of the fraction of 34s atoms for the energy transfer process $34p_{3/2,|m_j|=3/2} + 34p_{3/2,|m_j|=3/2} \rightarrow 34s_{1/2} + 35s_{1/2}$. The amplitude of the experimental data is scaled to fit. 78
53. Interaction time dependence of the population of 34s atoms for different Rydberg densities with the three-atom model. 79

CHAPTER 1

INTRODUCTION

Rydberg atoms are atoms in highly excited electronic states of high principal quantum number, n . Their first appearance is in the Balmer series of hydrogen in 1885. These highly excited atoms have exaggerated properties, some of them being large orbital radius and dipole moment that scale with n^2 , polarizability that scales with n^7 , van der Waals forces that scale with n^{11} , binding energy that scales with n^{-2} , and radiative lifetime that scales with n^3 . They are extremely sensitive to electric fields because of their huge polarizabilities. Their energy levels can be shifted to tune interactions between them with modest electric fields via the Stark effect. They can also readily be field ionized for detection of Rydberg states because their valence electrons are weakly bound [1]. With advances in laser technology which enable efficient production of Rydberg atoms, they have been employed in numerous experimental investigations. For example, the van der Waals interactions among a dense ensemble of Rydberg atoms were first observed by Raimond and Haroche using spectral line broadening due to the interaction [2]. The van der Waals interaction energy between a Rydberg atom and its images in the conducting walls of a cavity was also measured by Sandoghdar et al. by measuring the shift in Rydberg excitation spectra [3]. Rydberg atoms were utilized in the seminal experimental investigations of resonant energy transfer collisions by Safinya et al. using an electric field [4], and by Kachru et al. using a microwave field [5]. The total internal energy of a pair of colliding atoms is conserved in such collisions. By using resonant energy transfer collisions between Rydberg atoms Stoneman et al. measured the quantum defect of the p states of potassium [6]. These experiments were performed with atomic beam sources at room temperature where the thermal energy of the atoms is much larger than the interaction energy.

Advances in laser cooling and trapping of atoms have made possible investigations of interactions among Rydberg atoms at temperatures near absolute zero. The idea that atomic vapors can be cooled with laser light was independently proposed by Hansch and Schawlow, and Wineland and Dehmelt in 1975 [7, 8]. Trapping of neutral atoms in a magneto-optical trap (MOT) was first achieved in 1987 [9], and the

observation of a Bose-Einstein condensate (BEC) was achieved in 1995 [10]. The development of laser cooling and trapping techniques that have opened up the field of ultracold atomic physics where many interesting physical systems at ultracold temperatures are investigated, and the observation of BEC were recognized with Nobel prizes awarded to Steven Chu, Claude Cohen-Tannoudji, and Williams D. Phillips in 1997 and Eric Cornell, Wolfgang Ketterle, and Carl Wieman in 2001. The MOT operation has been demonstrated for about thirty different neutral elements to date [11]. In 1999 B. DeMarco and D. S. Jin reported the observation of the emergence of degeneracy in a fermionic atomic gas [12]. Recently BECs and quantum degenerate Fermi gases were demonstrated for dysprosium by Mingwu et al. [13, 14] and erbium by Aikawa et al. [15, 16]. These are lanthanide atoms that have large magnetic moments of 10 and 7 Bohr magnetons (μ_B) respectively, that provide strong magnetic dipole-dipole interactions between neutral atoms.

The resonant energy transfer collisions mediated by the long range dipole-dipole interactions are known as Förster resonances [17] for their similarity with the Förster resonant energy transfer (FRET) mechanism for energy transfer between two pigment molecules in photosynthetic organisms [18]. It is named after Theodor Förster who first described this mechanism as the non-radiative energy transfer between two molecules through a dipole-dipole interaction [19]. Resonant energy transfer occurs when the energy levels of a pair of colliding atoms lie midway between the energy levels of dipole allowed transitions so that the total energy of the initial colliding pair of atoms and that of the product pair are equal. Although there are accidental nearly resonant interaction channels, there will usually be an energy defect defined as the difference in energy between the initial colliding pair of atoms and the product pair in the absence of an external field. This energy defect can be brought to zero for tuning Förster resonances by shifting the energy levels of the atoms with a dc electric field via Stark effect [4, 20, 21, 22, 23]. Microwave-assisted resonances [5, 24, 25] and radio-frequency-assisted Förster resonances have also been observed [26]. The collisional cross sections increase sharply at resonances, and are observed to be $\sim 10^3$ times greater than the geometric cross sections which scale with n^4 [4].

Interactions between Rydberg atoms produced in the ultracold atomic vapors of $\sim 100\mu K$ differ from the binary interactions between the Rydberg atoms produced in atomic vapors at room temperature of $300K$. At ultracold temperatures Rydberg atoms move only a few percent of their interatomic spacing, typically $\sim 10\mu m$ in

a magneto-optical trap during the time of interest of a few microseconds for interactions between them [27, 20]. Therefore, they are essentially frozen in place and are accordingly referred to as “frozen Rydberg gas”. The interactions between many static atoms in a frozen gas are analogous to interactions in an amorphous solid. In frozen Rydberg gases there exists additional resonant dipole-dipole interaction channels which give rise to many-body effects besides the interaction channels where resonances are induced with an applied external field. Many-body effects in the frozen Rydberg gases are manifested in the spectral line broadening of resonances that cannot be accounted for with a binary collisions picture of interactions between Rydberg atoms in dilute gases at room temperature [20]. Mourachko et al. demonstrated the importance of many-body interactions by introducing additional Rydberg atoms to the Stark-tuned resonant energy transfer process between the Rydberg atoms of different states [28]. In doing so, another always resonant interaction channel was introduced, and it was observed that the spectral line width of the resonances were dependent on the density of the added Rydberg atoms. Similar effects on the spectral line widths due to many-body interactions were reported by Anderson et al. [29], and Carroll et al. [30]. The observation of the direct evidence of the three-body interaction was reported by Han et al. [31], and observation of resonant four-body interaction in cold cesium Rydberg atoms using Stark-tuned Förster resonance process was reported by Gurian et al. [32].

The strong dipole-dipole interaction among Rydberg atoms has been of great interest for implementation of quantum computation proposed by DiVincenzo [33]. Jaksch et al. proposed that the dipole-dipole interactions among Rydberg atoms can provide fast quantum gates for neutral atoms [34]. The energy level shifts associated with the dipole-dipole interactions between atoms in an ultracold atomic ensemble can prevent excitation of more than a single Rydberg excitation in the ensemble if the bandwidth of the laser used for the excitation is narrower than the interaction-induced energy shift. This phenomenon is known as Rydberg blockade or dipole blockade. In this blockade regime, a single Rydberg excitation is collectively shared among interacting atoms in the ensemble. The Rydberg blockade phenomenon has been intensively investigated for its application in quantum computation. For example, Lukin et al. proposed a scheme for quantum information processing in mesoscopic atomic ensembles using Rydberg blockade along with Förster process [35]. An extensive review on quantum information processing with Rydberg atoms by Saffman et

al. can be found at [36]. The suppression of Rydberg excitation due to van der Waals interaction was first observed by Tong et al. [37], and Singer et al. [38], followed by the observation of evidence of Rydberg blockade at Förster resonances by Vogt et al. [39]. The Rydberg blockade was also observed in a Bose-Einstein condensate by Heidemann et al. where several thousands of atoms were blocked from excitation in the vicinity of a single excitation [40]. The observation of Rydberg blockade for two single atoms confined separately in two optical dipole traps was independently reported by Gaëtan et al. [41] and Urban et al. [42] in 2009. Saffman et al. demonstrated a controlled-not quantum gate between two neutral atoms in the following year [43].

Another area of considerable interest closely related to studies of ultracold Rydberg atoms is ultracold neutral plasma that is produced by photo-ionizing ultracold atoms. The frequency of the photo-ionization laser beam is usually set around the ionization threshold of the atoms so as not to impart extra kinetic energy to the plasma created. The first ultracold neutral plasma with electron temperature of about 100 mK was demonstrated by Killian et al. by photo-ionizing ultracold xenon atoms in a magneto-optical trap [44]. This temperature is orders of magnitude lower than the temperature of ten thousand Kelvin or more of the plasmas traditionally produced by collisional ionization. One of the areas of investigation is the potential of reaching the so-called “strong coupling regime” with ultracold neutral plasmas where the electrical interaction between the charged particles exceeds the average kinetic energy [45, 46]. However, reaching this regime has remained elusive so far partially due to a heating mechanism known as disorder-induced heating [47, 48, 49]. Immediately after the photoionization, the Coulomb interaction among randomly distributed charged particles leads to increase in average kinetic energy of the plasma. It has also been observed that a dense sample of ultracold Rydberg atoms spontaneously evolves into an ultracold plasma [50]. The mechanisms responsible for initiating such evolution are found to be blackbody ionization and collisions between Rydberg atoms [51, 52].

In this dissertation, we report the observation of the catalysis effect of additional Rydberg atoms in the resonant energy transfer process and also the observation of Stark-tuned Förster resonances. We have investigated the energy transfer process of $34p + 34p \rightarrow 34s + 35s$ in a cold ^{85}Rb Rydberg gas. By adding $34d$ state Rydberg atoms into the energy transfer process, we have observed the increase in $34s$ state

population. Although the $34d$ state atoms do not directly participate in the $34p + 34p \rightarrow 34s + 35s$ energy transfer process, they add an interaction channel $34d + 34p \rightarrow 34p + 34d$ that is resonant for all electric fields. We have also investigated the interaction time dependence of the $34s$ state population, and compared the results with numerical simulations.

This dissertation is organized in five chapters. The second chapter contains the theoretical background for Rydberg atoms, Stark structures of the Rydberg atoms, and the dipole-dipole interaction between Rydberg atoms, and also laser cooling and trapping of ^{85}Rb atoms. In the third chapter, the experimental setup, characterization of the dye lasers used in the experiments, and the timing sequences of the experiments will be discussed. In the fourth chapter, the results and analysis of the experiments will be presented. In the last chapter, experimental results and analysis will be summarized and we conclude the dissertation with a brief outlook for future investigations.

CHAPTER 2

THEORETICAL BACKGROUND

2.1 RYDBERG ATOMS

Rydberg atoms are atoms in highly excited electronic states with high principle quantum number, n . The knowledge of them can be traced back to 1885 when Balmer's formula for the wavelengths of the visible spectral lines of atomic hydrogen was discovered, and is given by [53]

$$\lambda = \frac{bn^2}{n^2 - 4}, \quad (1)$$

where $b = 364.56$ nm. Balmer's formula in terms of wavenumber, ν , which is the inverse of the wavelength in vacuum is given by

$$\nu = \frac{4}{b} \left(\frac{1}{4} - \frac{1}{n^2} \right). \quad (2)$$

In 1888 Rydberg discovered that the wavenumbers for different series of observed lines of other atoms, notably alkali atoms, can be expressed as [53]

$$\nu_l = \nu_{\infty l} - \frac{R_y}{n^{*2}}, \quad (3)$$

where $n^* = (n - \delta_{nlj})$, the constant δ_{nlj} being quantum defect of the series l , $\nu_{\infty l}$ is the series limit, and R_y is known as the Rydberg constant and has the value of 109721.6 cm^{-1} . The series are sharp, principal and diffuse series which we now know as the series of the orbital angular momentum, l , states. Rydberg showed that the spectral lines of an atom are related and that Balmer's formula is a special case for transitions from $n = 2$ in hydrogen atom [53].

Alkali metal atoms are similar to hydrogen atom in having one valence electron. However, the nuclear charge of alkali metal atoms is screened by closed electron shells giving the core a finite size. For low orbital angular momentum states the valence electron penetrates and polarizes the core resulting in deviation from a Coulomb

TABLE 1: Quantum defect parameters for ^{85}Rb .

state	$n^2s_{1/2}$	$n^2p_{1/2}$	$n^2p_{3/2}$	$n^2d_{3/2}$	$n^2d_{5/2}$
δ_0	3.1311804	2.6548849	2.6416737	1.34809171	1.34646572
δ_2	0.1784	0.2900	0.2950	-0.60286	-0.59600

potential. The quantum defects, δ_{nlj} which are determined empirically from the spectroscopic measurements account for these deviations. The Rydberg-Ritz formula can be used for calculating quantum defects from empirically measured parameters, $\delta_0, \delta_2, \delta_4, \dots$, which are dependent on the quantum numbers l and j as followed.

$$\delta_{nlj} = \delta_0 + \frac{\delta_2}{(n - \delta_0)^2} + \frac{\delta_4}{(n - \delta_0)^4} + \dots \quad (4)$$

The parameters, δ_0 and δ_2 , for ^{85}Rb have been measured by Li et al. [54], and Han et al. [55]. The values of these parameters are listed in Table 1.

The Bohr model of the atom [56] in 1913 successfully explains the Rydberg formula. It assumes an electron moving classically in a circular orbit around an ionic core, the orbital angular momentum is quantized in integral units of \hbar , Planck's constant divided by 2π , and radiation occurs only for transitions between well defined energies [53]. The energy, W , of a state is the total of its kinetic and potential energies, and by taking into account of quantization of orbital angular momentum we get,

$$W = -\frac{k^2 Z^2 e^4 m_e}{2n^{*2} \hbar^2}, \quad (5)$$

where $k = 1/4\pi\epsilon_0$, ϵ_0 being the permittivity of free space, Z the atomic number, e the charge of electron, m_e mass of electron, and n^* effective principal quantum number. The Rydberg constant is given by

$$R_y = \frac{k^2 Z^2 e^4 m_e}{2\hbar^2}. \quad (6)$$

TABLE 2: Properties of Rydberg atoms. Adapted from [53].

Property	n^* dependence
Binding energy	n^{*-2}
Energy between adjacent states	n^{*-3}
Ionizing field	n^{*-4}
Orbital radius	n^{*2}
Geometrical cross-section	n^{*4}
Dipole moment	n^{*2}
Polarizability	n^{*7}
Radiative lifetime	n^{*3}

Rydberg atoms have many interesting properties, one of them being their enormous size; the orbital radius r scales as n^{*2} and as a result they have large geometrical cross-sections. Their dipole moment and polarizability scales as n^{*2} and n^{*7} respectively making them very responsive to external electric fields. The electron binding energy scales as n^{*-2} and the energy difference between adjacent n states scales as n^{*-3} . The ionizing electric field scales as n^{*-4} , and therefore Rydberg atoms in the states of higher principal quantum number can readily be detected by selective field ionization (SFI) method with relatively low electric fields [53]. These properties are listed in Table 2.

It is more convenient for calculations in atomic physics to use a different system of units known as Hartree atomic units than international system of units (SI units). In the Hartree atomic units system charge of electron e , mass of electron m_e , and reduced Planck constant \hbar are all set to equal to one and length is measured in Bohr radius a_0 . A few selected values of physical constants both in Hartree atomic units and SI units are given in Table 3. These numerical values are taken from the Committee on Data for Science and Technology (CODATA) recommended values of the fundamental physical constants [57].

2.2 STARK STRUCTURE OF RYDBERG ATOMS

The energy levels of an atom are shifted when it is placed in a static electric field, \mathbf{E} . This phenomenon is known as the Stark effect. Taking the direction of the electric field to be along the z-axis, the Hamiltonian of the atom in the field, H , is

TABLE 3: The CODATA recommended values for selected physical constants in Hartree atomic units and SI units [57].

Quantity	Atomic Units	SI Units
electron charge e	1	$1.602\ 176\ 487(40) \times 10^{-19}$ C
electron mass m_e	1	$9.109\ 382\ 15(45) \times 10^{-31}$ kg
reduced Planck constant \hbar	1	$1.054\ 571\ 628(53) \times 10^{-34}$ Js
Bohr radius a_0	1	$0.529\ 177\ 208\ 59(36) \times 10^{-10}$ m
electric dipole moment $a_0 e$	1	$8.478\ 352\ 81(21)^{-30}$ Cm
electric field	1	$5.142\ 206\ 32(13) \times 10^{11}$ V/m
fine structure constant α	$7.297\ 352\ 5376(50) \times 10^{-3}$	$7.297\ 352\ 5376(50) \times 10^{-3}$
speed of light c	137.035 999 679(94)	$299\ 792\ 458$ ms ⁻¹
energy	$e^2/a_0 = 1$ Hartree	$4.359\ 743\ 94(22) \times 10^{-18}$ J
time	1	$2.418\ 884\ 326\ 505(16) \times 10^{-17}$ s

the total of the Hamiltonian of the unperturbed atom, H_{atom} , and the Hamiltonian for interaction of the electric dipole moment of the atom and the field. In atomic units,

$$H = H_{atom} + Ez. \quad (7)$$

When the interaction energy is small compared to the energy level spacings of the unperturbed atom, the level shifts due to Stark effect can be found by perturbation methods. The matrix elements of the perturbation are

$$\langle nlm|Ez|n'l'm'\rangle = E\langle nlm|r \cos \theta|n'l'm'\rangle, \quad (8)$$

where $|n'l'm'\rangle$ and $|nlm\rangle$ are the eigenstates of the unperturbed atom. The selection rules for non-vanishing matrix elements are $m' = m$ and $l' = l \pm 1$. Hence, the first-order energy shift given by $\langle nlm|Ez|nlm\rangle$ vanishes. The second-order energy shift of $|n'l'm'\rangle$ is given by

$$\Delta E_{Stark} = \sum_{nlm \neq n'l'm'} \frac{|\langle nlm|Ez|n'l'm'\rangle|^2}{E_{n'l'm'} - E_{nlm}}, \quad (9)$$

where $E_{n'l'm'}$ and E_{nlm} are energy eigenvalues of the states $|n'l'm'\rangle$ and $|nlm\rangle$ respectively.

When the Stark energy shift is comparable to the energy difference to the next dipole coupled state, the diagonalization of the Hamiltonian of the atom in the external electric field is necessary to calculate the energy shift. Such diagonalizations for different electric fields give the Stark structure of the atom. Stark structures of the Rydberg states alkali-metal atoms were first numerically computed by Zimmerman et al. [58]. For computing the Stark structure for ^{85}Rb I use a program written by Pritchard. Details of the computation can be found in his thesis [59]. An overview of evaluating wavefunctions and dipole matrix elements along with a couple of Stark structures of ^{85}Rb for the current experimental investigations will be presented in the following section.

2.2.1 RYDBERG ATOM WAVEFUNCTIONS AND DIPOLE MATRIX ELEMENTS

Accurate wavefunctions are needed for the calculation of dipole matrix elements. For Rydberg states, these dipole matrix elements can be accurately evaluated from the wavefunctions of the atom in the absence of an external electric field for they weight strongly in the region where the potential seen by the valence electron can be approximated as a Coulomb potential that varies with $1/r$, where r is the coordinate of the valence electron [58]. The wavefunctions in the spherical coordinates, $\psi(r, \theta, \phi)$, can be obtained from solving the Schrödinger equation [60] given in atomic units as

$$\left[-\frac{1}{2\mu_e}\nabla^2 + V(r)\right]\psi(r, \theta, \phi) = W\psi(r, \theta, \phi), \quad (10)$$

where μ_e is the reduced mass of the electron, $V(r)$ is the potential and W is the energy. We use the symbol W for energy instead of E which is used to represent electric field. Since the potential depends only on r , the wavefunction can be separated into radial and angular parts: $\psi(r, \theta, \phi) = R(r)Y_l^m(\theta, \phi)$, where $Y_l^m(\theta, \phi)$ is a spherical harmonic which depends on the orbital angular momentum l and its projection m onto the quantization axis. The radial Schrödinger equation is given by

$$\left[-\frac{1}{2\mu_e}\left(\frac{d^2}{dr^2} + \frac{2}{r}\frac{d}{dr}\right) + \frac{l(l+1)}{2\mu_e r^2} + V(r)\right] = WR(r). \quad (11)$$

For alkali-metal atoms, the polarization of their cores for lower angular momentum states are no longer negligible, and accordingly $V(r)$ cannot be treated as purely

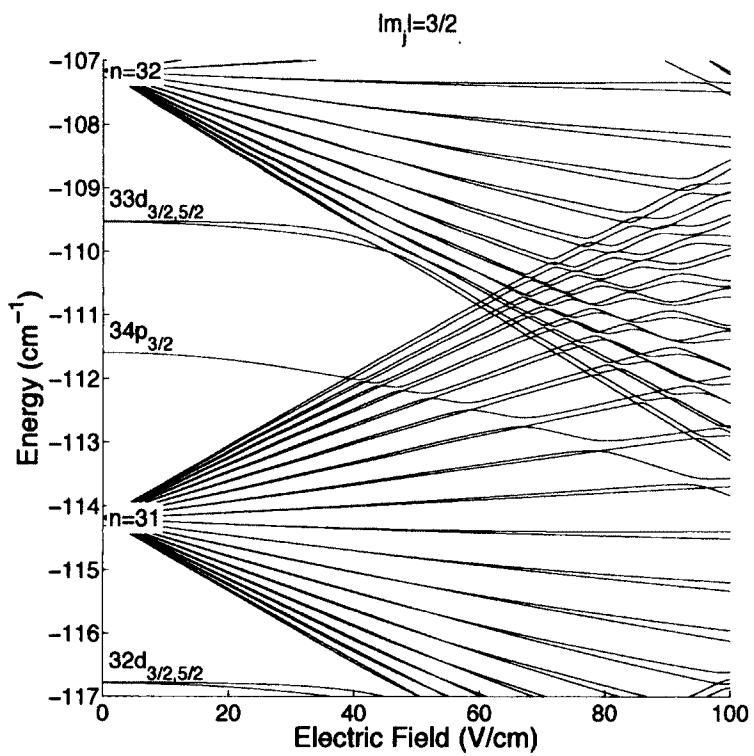
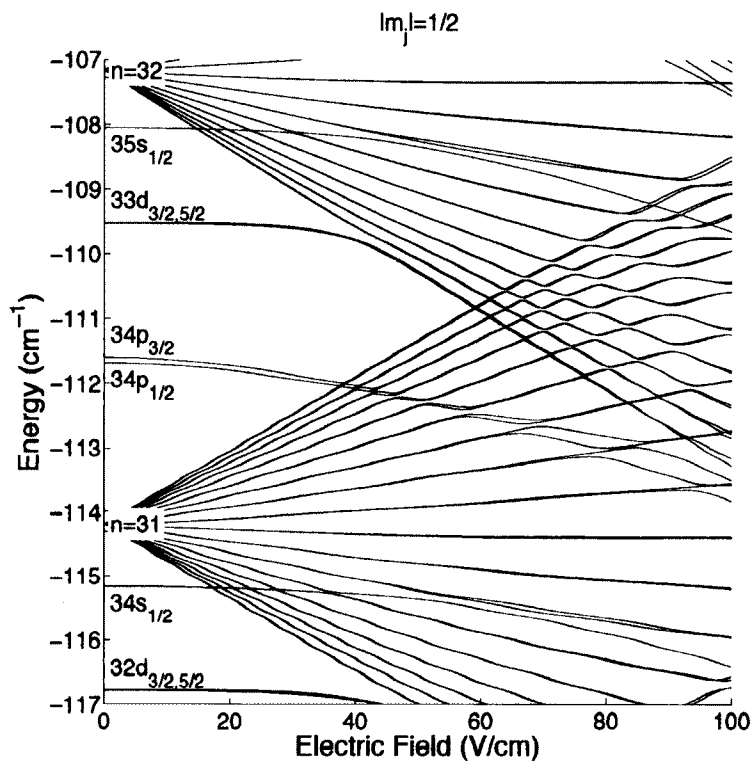


FIG. 1: Stark structures of ^{85}Rb for $n=34$.

Coulomb potential anymore. It is therefore most advantageous to solve the radial equation numerically for it allows the inclusion of perturbations to the Coulomb potential such as core-polarization and spin-orbit interaction terms [58]. Marinescu et al. provided a model potential that is dependent on the orbital angular momentum of the valence electron for taking into account the core-polarization [61]. This potential is given by

$$V_l(r) = -\frac{Z_l(r)}{r} - \frac{\alpha_c}{2r^4}[1 - e^{-(r/r_c)^6}], \quad (12)$$

where α_c is the static dipole polarizability of the core, and r_c is the cut-off radius. $Z_l(r)$ is the radial charge given by

$$Z_l(r) = 1 + (Z - 1)e^{-a_1 r} - r(a_3 + a_4 r)e^{-a_2 r}, \quad (13)$$

where Z is the nuclear charge of the atom. The authors obtained the optimized values of the parameters $r_c, a_1, a_2, a_3,$ and a_4 by fitting the above equations with fixed α_c to the alkali-metal-atom Rydberg energies. The spin-orbit interaction potential that gives rise to the fine structure splittings is given by [62]

$$V_{SO}(r) = \frac{\alpha^2}{2r^3} \mathbf{L} \cdot \mathbf{S}, \quad (14)$$

where $\alpha = \frac{1}{137}$ is the fine structure constant and

$$\mathbf{L} \cdot \mathbf{S} = \frac{1}{2}[j(j+1) - l(l+1) - s(s+1)], \quad (15)$$

where $j, l,$ and s are the quantum numbers for the total angular momentum, orbital angular momentum, and spin angular momentum respectively. The potential $V(r)$ is therefore

$$V(r) = V_l(r) + V_{SO}(r). \quad (16)$$

The radial wavefunction can then be found by first transforming equation (11) into the form $\frac{d^2}{dx^2} X = g(x)X$ with $X = R(r)r^{3/4}$ and $x = \sqrt{r}$ [63], and then solving it numerically using Numerov algorithm [64]. Integration is carried out inwards from the outer radius $r = 2n(n+15)$ to minimize the cumulative numerical errors [58] and is truncated at the inner radius $r = \sqrt[3]{\alpha_c}$ for the model potential is divergent near the origin.

The spin-orbit interaction in heavy alkali-metal atoms is large enough to influence the Stark structure and must be taken into account [58]. The total angular momentum is thus $j = l + s$ and the dipole matrix elements in this fine structure basis are given by

$$\begin{aligned} \langle nljm_j|Ez|n'l'j'm'_j\rangle &= \delta_{m_j,m'_j}\delta_{l,l'\pm 1}\langle nl|r|n'l'\rangle E \\ &\times \sum_{m_l=m_j\pm\frac{1}{2}} \langle l, \frac{1}{2}, m_l, m_j - m_l|jm_j\rangle \langle l', \frac{1}{2}, m_l, m_j - m_l, |jm_j\rangle \langle lm_l|\cos\theta|l'm_l\rangle. \end{aligned} \quad (17)$$

The radial dipole matrix elements $\langle nl|r|n'l'\rangle$ are evaluated from the radial wavefunctions derived from the model potential given in (12). The first two coefficients in the summation are Clebsch-Gordan coefficients and $\langle lm_l|\cos\theta|l'm_l\rangle$ can be evaluated from the algebra of spherical harmonics [65] since $\cos\theta = \sqrt{\frac{4\pi}{3}}Y_0^1$ where Y_0^1 is a spherical harmonic, and

$$\begin{aligned} \langle l'm'|Y_{LM}|lm\rangle &= (-1)^{m'}\sqrt{\frac{(2l'+1)(2L+1)(2l+1)}{4\pi}} \\ &\times \begin{pmatrix} l' & L & l \\ -m' & M & m \end{pmatrix} \begin{pmatrix} l' & L & l \\ 0 & 0 & 0 \end{pmatrix}, \end{aligned} \quad (18)$$

where the last two terms in the parentheses are the numerical coefficients given in $3j$ symbols, and they are non-vanishing only when

$$\begin{aligned} -m' + M + m &= 0, \\ l' + L + l &\text{ is even,} \\ \text{and } |l - l'| &\leq l + l'. \end{aligned} \quad (19)$$

The last term $\langle lm_l|\cos\theta|l'm_l\rangle$ in (17) is then given by

$$\langle lm_l|\cos\theta|l-1, m_l\rangle = \sqrt{\frac{l^2 - m_l^2}{(2l+1)(2l-1)}} \quad (20)$$

and

$$\langle lm_l|\cos\theta|l+1, m_l\rangle = \sqrt{\frac{(l+1)^2 - m_l^2}{(2l+3)(2l+1)}}. \quad (21)$$

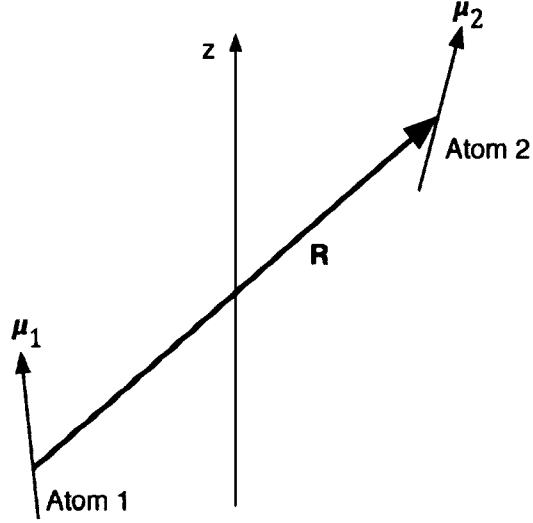


FIG. 2: Schematic diagram of two interacting dipoles separated by a distance R .

The Stark structures of ^{85}Rb for $|m_j| = 1/2$ and $|m_j| = 3/2$ are given in Fig. 1.

2.3 INTERACTION OF RYDBERG ATOMS

The primary interaction that induces atomic transitions is the electric dipole interaction. The transition probability due to the electric dipole interaction is a factor of $\sim 1/(Z\alpha)^2$ greater than that of the magnetic dipole interaction, where Z is the atomic number and α is the fine structure constant [66]. Rydberg atoms interact strongly via the electric dipole interaction since the dipole matrix element scales with n^2 . The interaction between two classical dipoles separated by a distance R is schematically illustrated in Fig. 2. The dipole-dipole interaction energy is given by

$$V_{dd}(R) = \frac{\boldsymbol{\mu}_1 \cdot \boldsymbol{\mu}_2}{R^3} - \frac{3(\boldsymbol{\mu}_1 \cdot \mathbf{R})(\boldsymbol{\mu}_2 \cdot \mathbf{R})}{R^5}, \quad (22)$$

where $\boldsymbol{\mu}_1$ and $\boldsymbol{\mu}_2$ are the dipole moments of the two interacting atoms, and \mathbf{R} is the displacement between the two dipole moments. The second term in the equation (20) accounts for the angular dependence of the interaction energy, and can be omitted for the discussion on the quantum mechanical description of the interaction that gives rise to Förster resonances. In the quantum mechanical description, the classical electric dipole moments are replaced with the matrix elements of the electric dipole

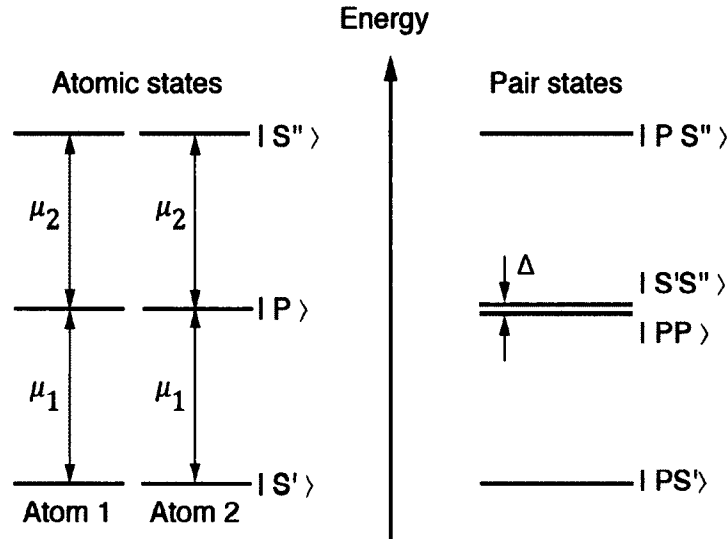


FIG. 3: Schematic diagrams of the energy levels of atomic states and two-atom or pair states (not to scale). In the atomic state basis, the states are coupled by the dipole matrix elements μ_1 and μ_2 . Transforming the atomic state basis into the pair state basis reveals two states that are almost degenerate with a small energy difference Δ called Förster defect.

operator, $\mu = \langle \phi | er | \phi' \rangle$. Consider two atoms in the states $|\phi'_1\rangle$ and $|\phi'_2\rangle$ respectively. The dipole-dipole interaction between them can be expressed as

$$V_{dd}(R) = \frac{1}{R^3} \sum_{|\phi_1\rangle, |\phi_2\rangle} \langle \phi_1 | \mu_1 | \phi'_1 \rangle \langle \phi_2 | \mu_2 | \phi'_2 \rangle. \quad (23)$$

The energy shifts associated with the dipole-dipole interaction can more readily be explained if the atomic state basis is transformed into the two-atom state or pair state basis. The dipole-dipole interaction in this basis is given by

$$V_{dd}(R) = \sum_{|\phi_1, \phi_2\rangle} \langle \phi_1, \phi_2 | \frac{\mu_1 \mu_2}{R^3} | \phi'_1, \phi'_2 \rangle. \quad (24)$$

The dipole selection rules are that the orbital angular momentum l of an individual atom must change by $l \pm 1$, and that the total projection of the angular momentum along the quantization axis $M = m_1 + m_2$ is conserved, where m_1 and m_2 are the individual projection angular momentum of the atoms involved in the interaction [67]. In principle, the sum in equation (22) must be over all intermediate states

that obey the dipole selection rules. In practice, this sum can be greatly simplified because in most cases only states with energy close to the initial state have significant dipole matrix elements to contribute to the sum [67]. For some atomic states, when transformed into two-atom or pair state basis, it happens that two of the pair states are almost degenerate with a small energy difference. This energy difference is known as Förster defect and is defined as the difference in energy between the final and initial pair states. For our experimental investigations, initial pair states are formed from the same atomic states giving

$$\Delta = E(n_a l_a j_a) + E(n_b l_b j_b) - 2E(n l j), \quad (25)$$

where the first two terms in the right hand side of (23) is the energy of the final atomic states and the last term is the energy of the initial atomic states. The dipole-dipole interaction can induce the transition between them. Schematic diagrams of the energy levels of the atomic state basis and the two-atom or pair state basis are given in Fig. 3. Treating the system in the pair state basis as a two-level system for the nearly degenerate pair states, the Hamiltonian of the system is given by

$$H = \begin{pmatrix} 0 & V_{dd}(R) \\ V_{dd}(R) & \Delta \end{pmatrix}. \quad (26)$$

The corresponding eigenvalues are

$$\lambda_{\pm} = \frac{\Delta \pm \sqrt{\Delta^2 + 4V_{dd}^2(R)}}{2}. \quad (27)$$

The energy levels of Rydberg atoms can readily be shifted with moderate electric fields via the Stark effect. Thus they present a unique ability to tune the Förster energy defect Δ . For some combinations of Rydberg states, their energy levels can even be tuned to make the energy defect vanish. In addition, the dipole-dipole interaction is dependent upon the interatomic distance, and thus can also be tuned for example by varying the density of the atomic sample. It is therefore necessary to consider the limiting cases.

When $V_{dd}(R) \ll \Delta$, a binomial expansion of (27) yields,

$$\lambda_{\pm} = \frac{\Delta}{2} \pm \left(\frac{\Delta}{2} + \frac{V_{dd}^2(R)}{\Delta} + \dots \right). \quad (28)$$

yielding the change in energy in this limit as

$$\begin{aligned}
 \Delta W_{vdW} &= -\frac{V_{dd}^2(R)}{\Delta} \\
 &= -\frac{(\mu_1\mu_2)^2/\Delta}{R^6} \\
 &= -\frac{C_6}{R^6}.
 \end{aligned} \tag{29}$$

This is the well known van der Waals interaction energy. In this regime the dipole-dipole interaction energy can be treated as a perturbation, and the second-order effect of the interaction gives rise to this interaction energy [68]. The van der Waals coefficient $C_6 = (\mu_1\mu_2)^2/\Delta$ scales as n^{11} since dipole matrix elements, μ_1 and μ_2 , scale as n^2 and the energy between adjacent states, Δ , scales as n^{-3} .

When $\Delta \ll V_{dd}(R)$ and Δ is negligible the interaction energy is given by

$$\begin{aligned}
 \Delta W &= \pm V_{dd}(R) \\
 &= \pm \frac{\mu_1\mu_2}{R^3} \\
 &= \pm \frac{C_3}{R^3}.
 \end{aligned} \tag{30}$$

The system in this regime exhibits resonant dipole-dipole interaction that scales with $1/R^3$, and it is the strongest possible interaction besides the Coulomb interaction for non-overlapping Rydberg atoms [36]. The resonant dipole-dipole interaction coefficient C_3 scales as n^4 .

2.3.1 FÖRSTER RESONANCES

The resonant dipole-dipole interaction character, scaling as $1/R^3$, appears as the Förster defect Δ as defined in (25) becomes comparable with the dipole-dipole interaction energy $V_{dd}(R)$. It is possible for some dipole-coupled Rydberg states to tune the Förster defect to vanish with moderate electric fields via the Stark effect. It can be seen from the Stark structure of ^{85}Rb given in Fig. 4 that at zero electric field the energy level of the state $34p_{3/2}$ nearly lies midway between the dipole-coupled states of $34s_{1/2}$ and $35s_{1/2}$ with the dipole matrix elements μ_1 and μ_2 respectively. At the electric field of 5.83 V/cm the energy level of the state $34p_{3/2}$ lies exactly

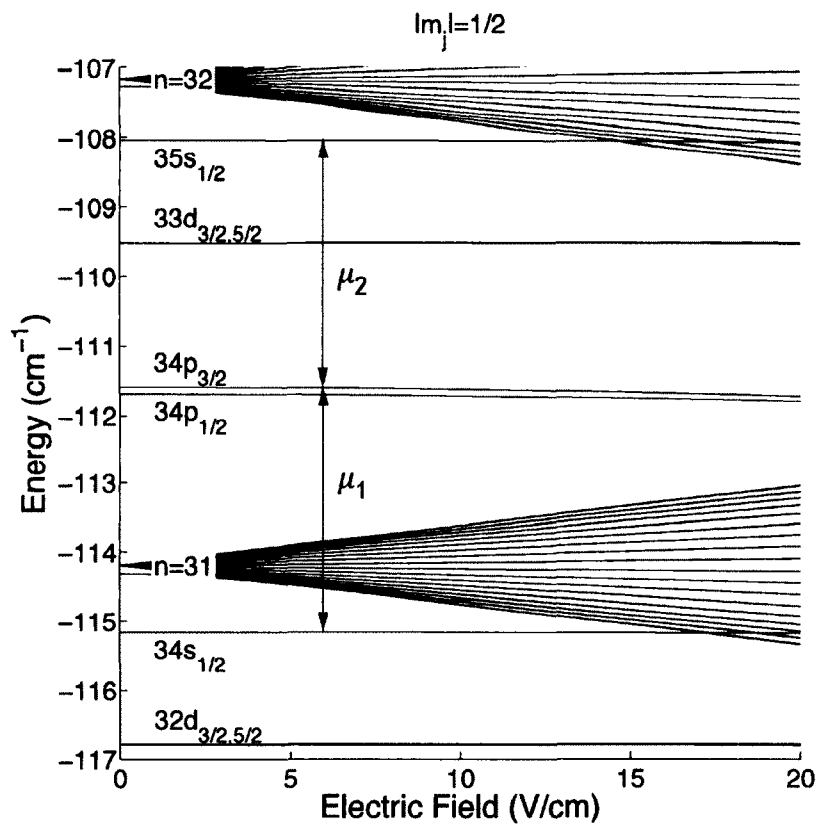


FIG. 4: Stark structure of ^{85}Rb showing the dipole-coupled states of $34s_{1/2}$ and $34p_{3/2}$ with the dipole matrix element μ_1 and $34p_{3/2}$ and $35s_{1/2}$ with the dipole matrix element μ_2 . The energy level of $34p_{3/2}$ lies midway between $34s_{1/2}$ and $35s_{1/2}$ at the field of 5.83 V/cm.

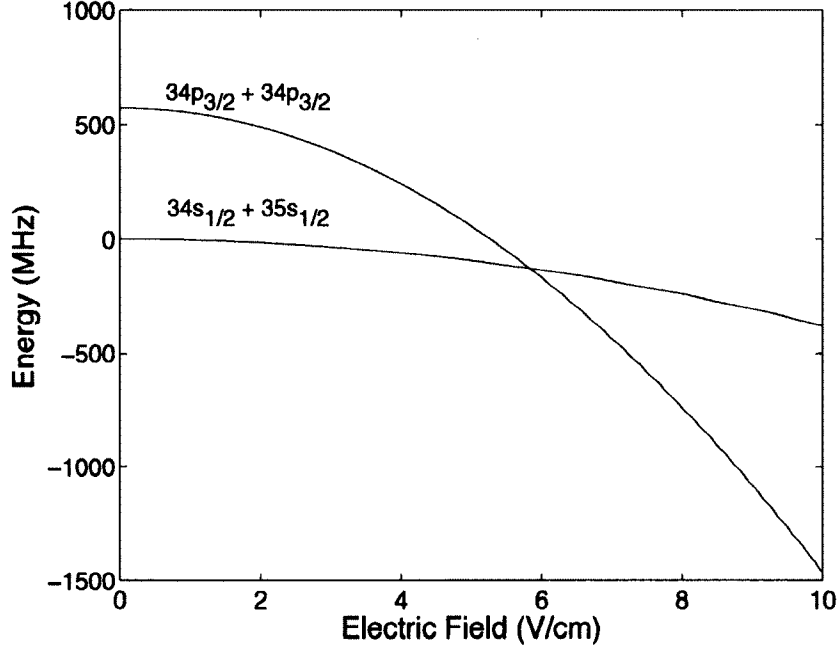
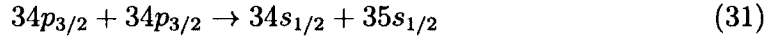


FIG. 5: Stark shift of the dipole-coupling allowed pair states $34s_{1/2} + 35s_{1/2}$ and $34p_{3/2} + 34p_{3/2}$, neglecting dipole-dipole interaction between them. Level crossing occurs at zero Förster defect.

midway between the two other states so that the Förster defect of the interaction



is zero, and the dipole interaction becomes resonant. Such resonances are known as Förster resonances. The Stark shifts of the dipole-coupling allowed pair states reveals the level crossings of the pair states. An example of such crossing is given in Fig. 5 for one of the resonances of the reaction given in (31). However, the dipole interaction between the two pair states was not taken into account. Diagonalization of the Hamiltonian of the dipole-coupled pair states such as the one given in (26) will result in finding energy levels for the eigenstates. The result of such diagonalization for the $34p_{3/2} + 34p_{3/2} \rightarrow 34s_{1/2} + 35s_{1/2}$ is given in Fig. 6 for Förster defects ranging from -100 MHz to 100 MHz. The interaction is taken to be resonant dipole interaction, $\mu_1\mu_2/R^3$, as given in (30). The reason for this is as follow: The radial dipole matrix elements in atomic units are calculated to be $\langle 34p_{3/2}|r|34s_{1/2}\rangle = 1100$

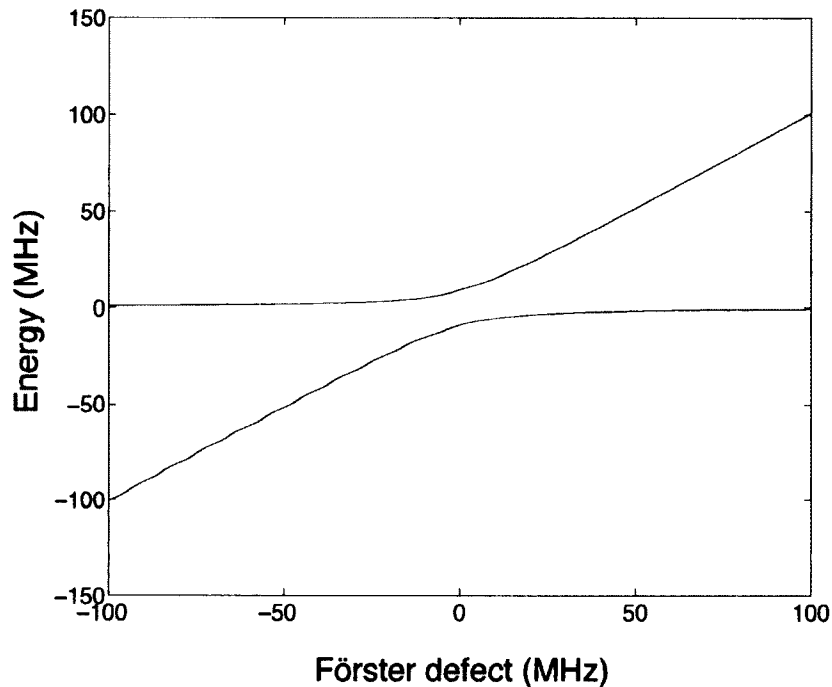


FIG. 6: The energy shifts for the resonant dipole interaction of $34p_{3/2} + 34p_{3/2} \rightarrow 34s_{1/2} + 35s_{1/2}$ vs. Förster defect. The resonant dipole interaction energy $\mu_1\mu_2/R^3$ is ~ 9.2 MHz for the distance between atoms of $5 \mu\text{m}$.

and $\langle 34p_{3/2} | r | 35s_{1/2} \rangle = 1074$, and the distance between the atoms is taken to be $5 \mu\text{m}$ which is the achievable interatomic spacing in a magneto-optical trap. The resulting dipole interaction energy is ~ 9.2 MHz which is comparable with the Förster defects used in the calculation.

2.4 LASER COOLING AND TRAPPING OF ATOMS

Cooling of atomic vapors by radiation pressure of laser light was independently proposed by Hansch and Schawlow, and Wineland and Dehmelt in 1975 [7, 8]. They proposed that if the frequency of the laser irradiating an atomic vapor is set to the lower half of the Doppler-broadened absorption line of the vapor, it can be cooled since atoms moving toward the laser will see frequencies Doppler-shifted closer toward the atomic transition, and thus will have large scattering cross sections while those moving away from the laser will see even lower frequencies from the resonant frequency of the transition. A damping force arises in the process of many scattering

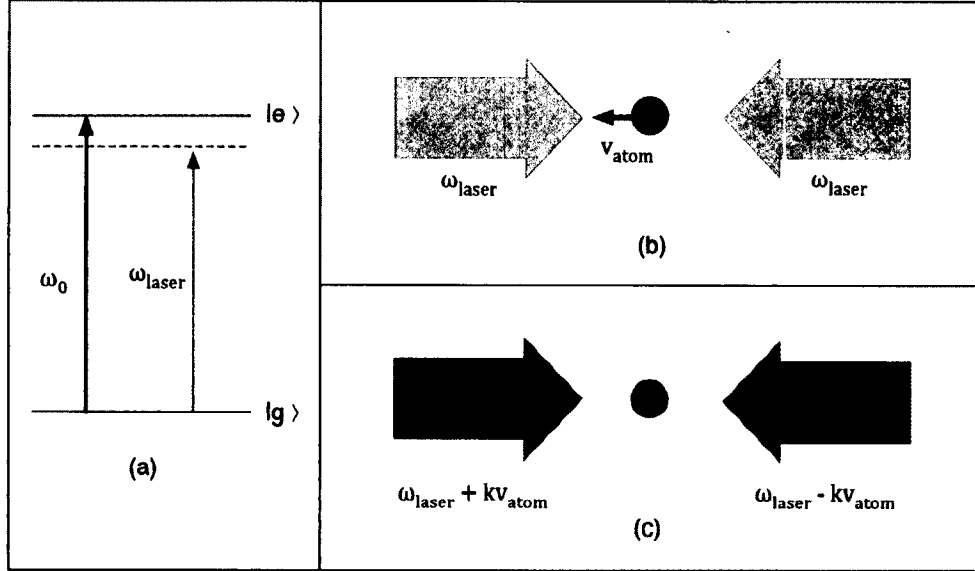


FIG. 7: Doppler cooling scheme. (a) Two-level atom model, ω_0 is the resonant angular frequency of the transition and ω_{laser} is the angular frequency of the laser tuned lower than ω_0 . (b) In the laboratory frame the atom is moving toward one of the counter-propagating laser beams and away from the other. (c) In the atom's rest frame the frequency of the beam from the left appears higher than ω_0 (blue shifted), and the frequency of the beam from the right appears lower than ω_0 (red shifted).

events, absorption of photon followed by spontaneous emission in random direction, because on the average there is a net change in momentum: the average momentum associated with recoil from spontaneous emission is zero whereas that associated with absorption is not. This force is given by [69]

$$\vec{F}_{OM} \approx \frac{8\hbar k^2 \delta I / I_s \vec{v}}{\Gamma(1 + I/I_s + (2\delta/\Gamma)^2)^2}, \quad (32)$$

where \hbar is reduced Planck constant, $k = \frac{2\pi}{\lambda}$ is the magnitude of the wave vector of the radiation, λ being its wavelength, \vec{v} is the velocity of the atom, $\delta = \omega_0 - \omega_{laser}$, is the detuning of laser frequency, ω_{laser} , from the resonant frequency ω_0 , I is the intensity of the radiation, $I_s = \pi\hbar c/3\lambda^3\tau$, is saturation intensity of the transition where h is Planck constant, c is speed of light, and τ is the radiative lifetime of the excited state, and Γ is the decay rate which is equal to the inverse of τ . The acceleration due to this viscous force is about 10^4g , where g is the gravitational acceleration. This cooling scheme known as the Doppler cooling is illustrated in Fig. 7. There,

however, is a limit to lowest temperature achievable with Doppler cooling due to heating associated with random nature of recoils from spontaneous emission: atoms can diffuse out of the overlap region of the beams and hence no longer be cooled. This Doppler cooling limit is given by [70]

$$T_D = \frac{\hbar\Gamma}{2k_B}, \quad (33)$$

where k_B is the Boltzmann's constant. For rubidium atoms, this temperature is about $146\mu\text{K}$. Chu et al. in 1985 first demonstrated viscous confinement and cooling of neutral sodium atoms in three dimensions via the radiation pressure of counter propagating laser beams [71], an experimental arrangement now commonly referred to as optical molasses.

It was soon realized that the temperature of the atoms in the optical molasses was well below the Doppler cooling limit [72]. The mechanism responsible for cooling below the Doppler limit was explained by Dalibard and Cohen-Tannoudji in 1989, and is known as polarization gradient cooling [73]. The overlapping beams form spatially varying polarizations in an optical molasses. Unlike a simple two-level atom model, the ground state of alkali atoms used in laser cooling has multiple sub-levels. Preferential population of atoms into a certain sub-level of ground state, known as optical pumping, occurs when multi-level atoms interact with nearly resonant light depending on the polarization of the light. The interaction also shifts the energy levels [69]. The combined effect of these mechanisms is that as atoms move in the polarization gradients they scatter light such that the frequency of spontaneous emission is higher than that of absorption. This energy dissipation into the radiation field results in cooling below the Doppler limit. Optical molasses, however, is not a trap because its damping force for cooling is dependent only upon the velocity of the atoms rather than their positions as well for spatial confinement.

2.4.1 MAGNETO-OPTICAL TRAP

The damping force which arises from the radiation pressure of scattering events will become position dependent if the scattering rate can be made position dependent. This is achieved by exploiting the internal structure of alkali atoms: the separation between energy levels can be made position dependent via the Zeeman

effect. Trapping by this arrangement is known as magneto-optical trapping. The first magneto-optical trap that confined neutral alkali atoms was demonstrated in 1987 by Raab et al. [9]. The basic principle of the trap is illustrated in Fig. 8. Consider a hypothetical atom with the angular momentum $J = 0(m_j = 0)$ in the ground state and $J = 1(m_j = -1, 0, 1)$ in the excited state. The m_j states for $J = 1$ are degenerate in the absence of an external magnetic field. This degeneracy is lifted in the presence of an external magnetic field. The amount of shift in energy is given by $\Delta E = g_j m_j \mu_B B$, where the constants g_j and μ_B are the Lande g factor and the Bohr magneton respectively, and B is the magnetic field. If the magnetic field varies linearly with position so will the shift in energy as shown in Fig. 8. The counter-propagating beams to induce the transition are circularly polarized, and have opposite polarizations σ_+ and σ_- respectively. The selection rules for circularly polarized light are $\Delta m_j = \pm 1$: σ_+ beam induces the transition from the ground state to $m_j = +1$ state, and σ_- beam to $m_j = -1$ state respectively. The frequency of the beams, ω_l , is detuned from the resonant frequency of the transition in the absence of the magnetic field. In a magnetic field gradient that causes the linear shift in energy of the m_j states as illustrated in Fig. 8, atoms at the position z' will scatter more from the σ_- beam than σ_+ beam since its frequency, ω_l , is now closer to the resonant frequency of the transition from the ground state to the $m_j = -1$ state. Therefore, the radiation pressure from the σ_- beam is greater than that from the σ_+ beam and atoms are pushed back to the center where the magnetic field is zero. A similar process occurs on the opposite of z' where the radiation pressure from σ_+ beam is greater than that from the σ_- beam. Consequently, atoms are constantly pushed into the central region of the trap. This trapping scheme can be extended to three dimensional trapping with six laser beams.

For the current experimental investigations, ^{85}Rb atoms, one of the stable isotopes of rubidium, are confined in a magneto-optical trap. Its atomic number is 37 and atomic mass is 84.911u. The electron configuration of ^{85}Rb is $(1s)^2(2s)^2(2p)^6(3s)^2(3p)^6(4s)^2(3d)^{10}(4p)^6(5s)^1$. A few important physical properties of ^{85}Rb are given in Table 4. Only the outermost electron contributes to the total angular momentum of the atom. The total angular momentum due to the orbital angular momentum, \mathbf{L} , and spin angular angular momentum, \mathbf{S} , of the outermost electron is given by

$$\mathbf{J} = \mathbf{L} + \mathbf{S}. \quad (34)$$

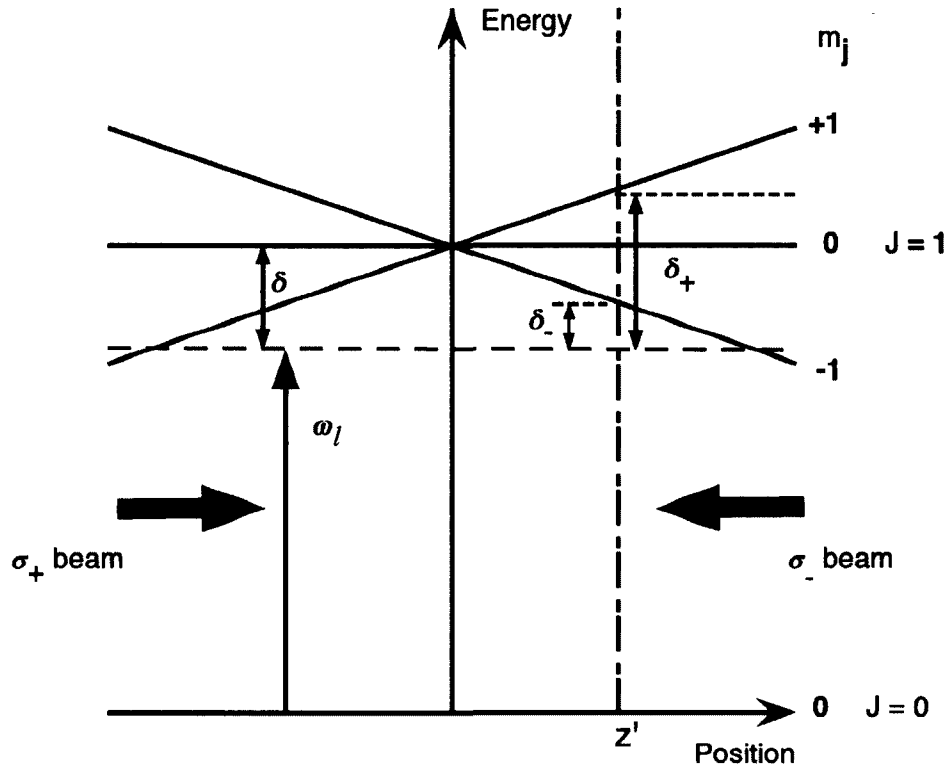


FIG. 8: The principle of magneto-optical trapping [69].

TABLE 4: Rubidium 85 Physical Properties [74].

Quantity	Symbol	Numerical value
Atomic number	Z	37
Total nucleons	$Z + N$	85
Relative natural abundance	η	72.17(2)%
Atomic mass	m	$1.409\,993\,199(70) \times 10^{-25}$ kg 84.911 789 732(14) u
Nuclear spin	I	5/2
Ionization limit	E_I	33 690.798 90(20) cm^{-1} 4.177 126 33(10) eV
Density at 25°C	ρ_m	1.53 g/cm^3
Vapor pressure at 25°C	P_v	$3.92(20) \times 10^{-7}$ torr

The values of the quantum number \mathbf{J} lie in the range $|L - S| \leq J \leq |L + S|$. Atoms also have the nuclear spin angular momentum \mathbf{I} . Coupling of \mathbf{J} and \mathbf{I} results in the total atomic angular momentum

$$\mathbf{F} = \mathbf{J} + \mathbf{I}. \quad (35)$$

The values of \mathbf{F} lie in the range $|J - I| \leq F \leq |J + I|$. The magnitude of electronic and nuclear spin angular momentum are $S = \frac{1}{2}$ and $I = \frac{5}{2}$ respectively. The cycling transition for trapping is between $F = 3$ of the ground state $5^2S_{1/2}$ and $F' = 4$ of the excited state $5^2P_{3/2}$ as illustrated in Fig. 9. The Russell-Saunders notation of $n^{2S+1}L_J$ is used, where n is the principal quantum number, in describing the electronic states of ^{85}Rb atoms. The frequency of the laser is red-detuned from the $F = 3 \rightarrow F' = 4$ trapping transition, and thus effectively blue-detuned from $F = 3 \rightarrow F' = 3$ transition which is allowed since the selection rule for \mathbf{F} is $\Delta F = 0, \pm 1$, and the separation between the $F' = 3$ and $F' = 4$ is only ~ 120 MHz. Therefore, there is some probability of the atoms making $F = 3 \rightarrow F' = 3$ transition, and some of these atoms will spontaneously decay to $F = 2$ of the ground state. These atoms will now leave the confinement region since $F = 2$ and $F = 3$ of the ground state are separated by ~ 3 GHz, and the frequency of the trapping laser is set for $F = 3 \rightarrow F' = 4$ transition. To recycle these atoms another laser whose frequency is set for $F = 2 \rightarrow F' = 3$ transition must be introduced. Some of the atoms excited to $F' = 3$ by this repumping laser will spontaneously decay to $F = 3$ of the ground state so that they will be excited to $F' = 4$ state again by the trapping laser.

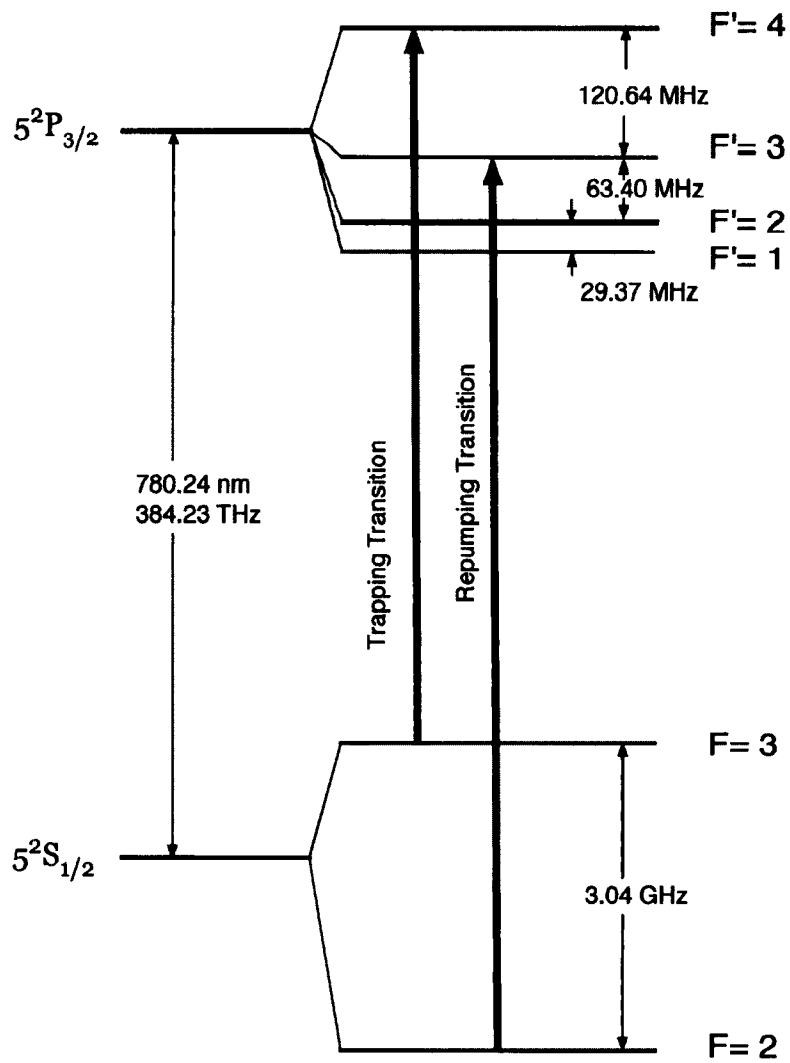


FIG. 9: The energy levels of ^{85}Rb for magneto-optical trapping. Adapted from [74].

CHAPTER 3

EXPERIMENTAL SETUP FOR CREATION AND DETECTION OF RYDBERG ATOMS

In this chapter the experimental setup for creation and detection of Rydberg atoms will be discussed. It includes discussion of vacuum system for the magneto-optical trap, setup of laser systems for cooling and trapping of ^{85}Rb atoms, exciting ground state atoms to desired Rydberg states, and detection systems and methods for Rydberg states.

3.1 VACUUM SYSTEM

For magneto-optical trapping an ultra high vacuum (UHV) is required to keep the collisional loss of the trap minimum so that the trap will have long enough lifetime for most experiments [75]. The vacuum system for the magneto-optical trap consists of a cylindrical stainless steel chamber, an ion pump (Ultek D-I) with a pumping rate of 11 liter/second, a 5kV power supply from Perkin-Elmer for the ion pump, and a rubidium dispenser (SEAS Getters USA Inc.) mounted in the chamber through an electrical feedthrough. The diameter and the length of the chamber are 5 inches and 2.5 inches respectively. The chamber has ten 2.75 inches conflat ports, six of which are used for transmitting laser beams for the magneto-optical trap, and the rest are used for excitation and detection of Rydberg states. The schematic diagram of the top view of the vacuum system is given in Fig. 10. The pressure of the chamber is maintained at 10^{-9} Torr. The current for the rubidium dispenser is typically set to 3.2A during the experiment.

3.2 CREATION OF RYDBERG ATOMS

The process of creating Rydberg atoms includes cooling and trapping of ^{85}Rb atoms in a magneto-optical trap (MOT) using diode lasers and a quadrupole magnetic field, and then exciting atoms confined in the MOT to desired Rydberg states with commercial and homebuilt dyes lasers which are pumped with Nd:YAG lasers. The

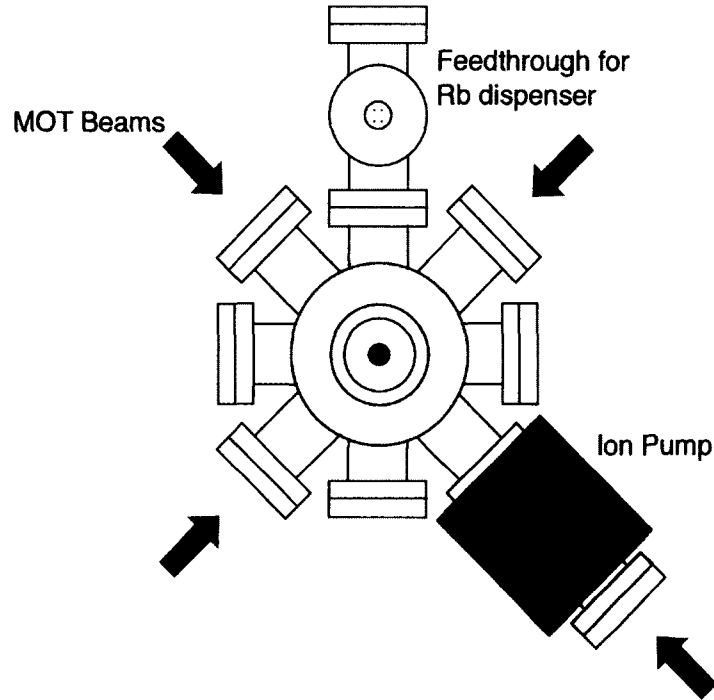


FIG. 10: Schematic diagram of the top view of the vacuum system for the magneto-optical trap.

quadrupole magnetic field for the MOT is derived from a pair of anti-Helmholtz coils mounted outside the chamber. The magnetic field gradient is $\sim 10 \text{ Gcm}^{-1}$.

3.2.1 LASER SYSTEMS FOR MAGNETO-OPTICAL TRAP

For trapping atoms, three diode lasers are used: a pair of diode lasers in master-slave configuration for the trapping transition and another laser for the repumping transition. Except for the slave laser, the lasers are external cavity diode lasers (ECDL) in Littman-Metcalf configuration [76]. An ECDL in this configuration consists of a laser diode, a collimating lens, a diffraction grating and a mirror. The collimated laser beam from the diode laser is shone on a diffraction grating. Optical feedback is achieved by reflecting the first-order beam back to the diode laser with a mirror which can be adjusted for tuning wavelength. For finer adjustment of the angle, a piezo electric transducer (PZT) is attached to the mirror mount. The zeroth-order beam reflected from the grating is the output of ECDL in this configuration as schematically illustrated in Fig. 11. For this experimental setup, a diode laser

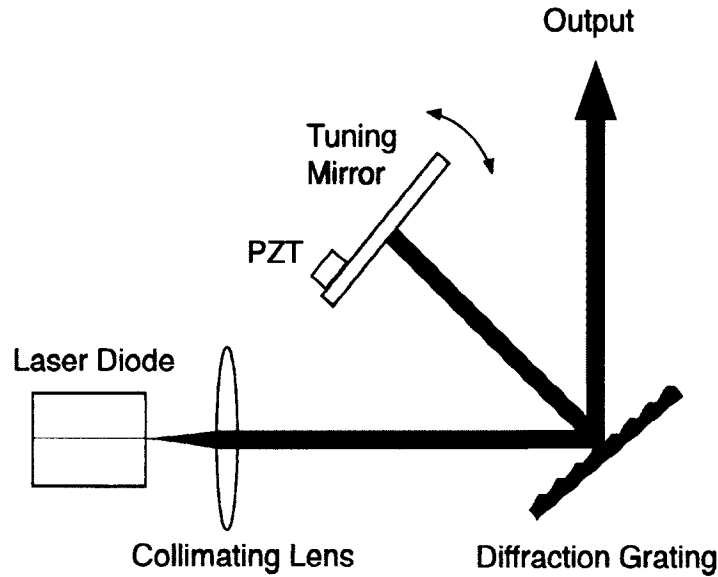


FIG. 11: External cavity diode laser in Littman-Metcalf configuration (not to scale).

(Sanyo DL 7140-201S) is held in a collimating tube (Thorlabs LT230P-B) which in turn is held in an aluminum housing. This assembly is mounted on an aluminum slab with a thermoelectric cooler (Marlow DT12-6-01L) placed in between them. Its temperature is monitored with a thermistor which provides feedback to a temperature controller connected to the thermoelectric cooler in order to maintain a constant temperature for the diode assembly. The diode injection current is controlled by a current controller. The spectral linewidth of an ECDL in this configuration is less than 1MHz [77]. A schematic layout of laser systems for magneto-optical trap is given in Fig. 12. In order to achieve a higher power for the trapping laser beam a master-slave configuration is employed: a portion of light from an ECDL master laser is injected into a free-running diode laser (Sharp GH0781JA2C) causing its spectrum to collapse into a single mode at the master laser frequency [78]. The power of the slave laser beam going into a fiber launcher is ~ 32 mW. The power of the beam after exiting the optical fiber is ~ 18 mW.

Acousto-optic modulators (AOM) are used for switching the laser beams for the experiment and also to control the detuning of the trapping laser beam. A portion of the beam from the master laser is reflected from a beam splitter and sent to a double-pass acousto-optic modulator system with an 80 MHz AOM. The frequency of

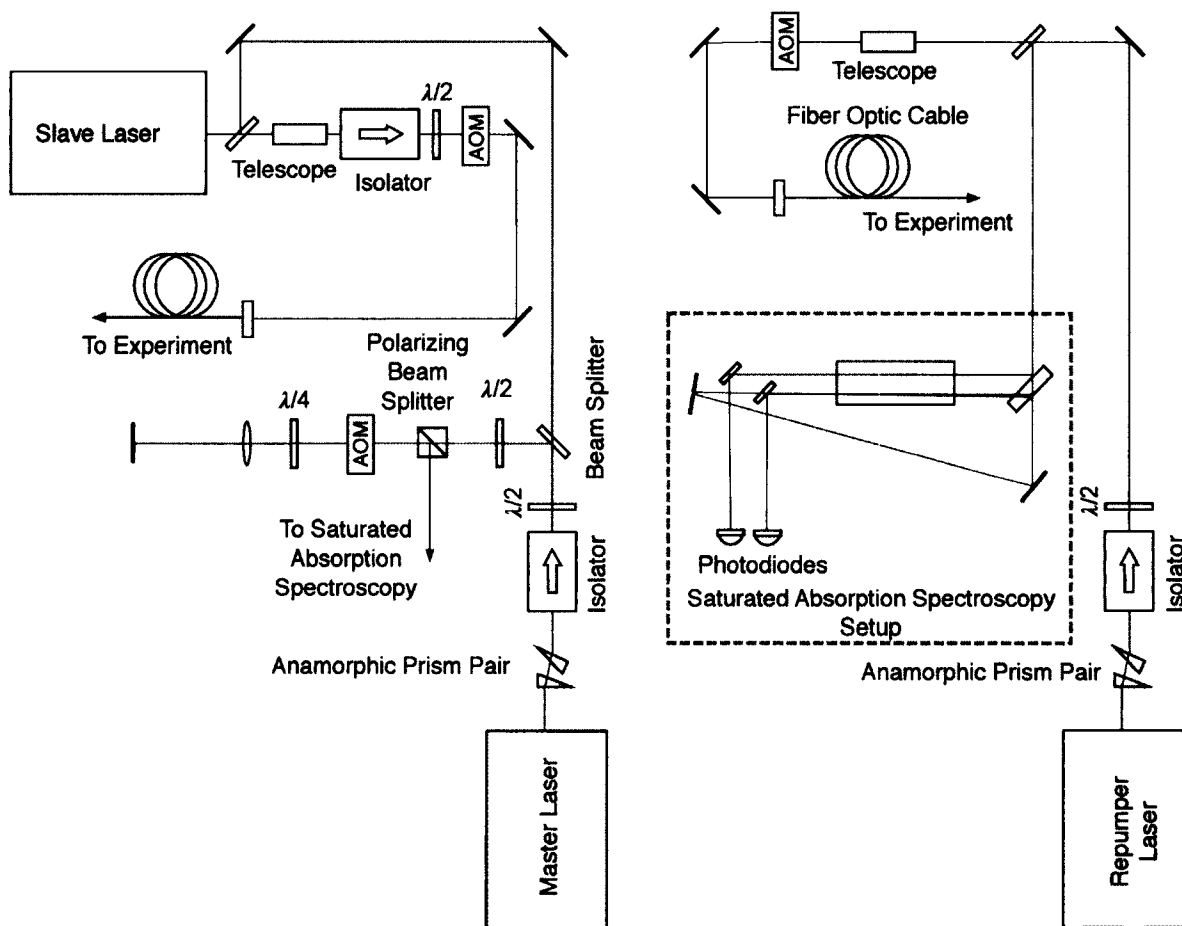


FIG. 12: Schematic layout of laser systems for the magneto-optical trap. AOM stands for acousto-optic modulator, and $\lambda/2$ and $\lambda/4$ represent half-wave plate and quarter-wave plate, respectively.

the laser beam is down-shifted 160 MHz by the double-pass system and the outgoing beam is sent to a saturated absorption spectroscopy (SAS) setup [79]. For frequency stabilization an active feedback loop is employed [80]. The injection current for the laser diode is modulated at ~ 10 kHz. The SAS signal is sent to a lock-in amplifier, and the dispersive signal from it is then sent to a lock-box, a servo loop, which continuously adjusts the PZT in the laser. The frequency of the master laser is locked to $F' = 2$ -3 crossover peak of the SAS for $F = 2 \rightarrow F' = 2, 3, 4$ transitions. This crossover peak is ~ -92 MHz away from the desired trapping transition of $F = 2 \rightarrow F' = 3$. Since the SAS for this setup is derived from the output beam of the previously mentioned double-pass acousto-optic modulator system, the locked frequency of the master laser is 160 MHz higher than the frequency had the SAS been derived directly from the master laser without the double-pass system. The slave laser beam passes through an acousto-optic modulator shifting its frequency by -80 MHz. This optical setup results in detuning of -12 MHz from the trapping transition. The SAS for the repumper laser is derived without the double-pass system. The laser frequency is locked to $F = 2 \rightarrow F' = 2$ transition and it is shifted $+63.4$ MHz by an AOM to be on resonance with the repumping transition ($F = 2 \rightarrow F' = 3$).

3.2.2 LASER SYSTEMS FOR EXCITATION TO RYDBERG STATES

Tunable dye lasers are employed to excite ground state atoms in the magneto-optical trap to desired Rydberg states. There are two sets of dye laser systems: one for excitation to nP Rydberg states directly from the $5S_{1/2}$ ground state, and the other for excitation to nS and nD states by the two-step excitation ($5S_{1/2} \rightarrow 5P_{3/2} \rightarrow nS, nD$). A typical excitation scheme is illustrated in Fig.13. Each dye laser system is pumped with an appropriate harmonic from a Nd:YAG laser.

In the first system, a commercial dye laser (Continuum ND6000) with flowing Rhodamine 6G dye is pumped by the second harmonic (532 nm) of a Q-switched Nd:YAG laser (Quantel Brilliant Eazy). The repetition rate and pulse width of this laser are 10 Hz and 5 ns respectively. It has maximum energy of ~ 170 mJ/pulse. The tunable wavelength range of the dye laser is between 575 nm and 600 nm, and the laser has the maximum energy of 10 mJ/pulse at 588 nm. The tuning curve of this laser is given in Fig. 14, and the energy of the dye laser tuned at ~ 600 nm vs. the energy of the pump laser is given in Fig. 15. The laser beam from the dye laser is sent through a frequency doubling crystal to achieve the wavelength of 297.7 nm for

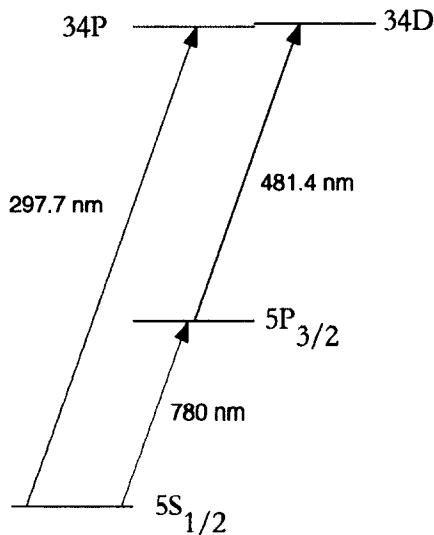


FIG. 13: Rydberg excitation scheme: excitation to $34P$ state directly from the ground state with 297.7 nm pulsed laser light, and to $34D$ state by the two-step excitation of $5S_{1/2} \rightarrow 5P_{3/2}$ with 780nm, and $5P_{3/2} \rightarrow 34D$ with 481.4 nm pulsed laser light respectively.

the excitation of desired $34P$ state. The output energy of 300 nm beam vs. the input energy of 600nm beam is given in Fig. 16. The conversion efficiency of the crystal is approximately three percent, and the typical energy of the laser while running the experiments is ~ 0.5 mJ/pulse. The 300 nm beam is separated from the 595.4 nm beam with a Pellin Broca prism. A portion of the 595 nm beam reflected from a beam splitter is sent to a wavelength meter (Bristol 821) for monitoring wavelength during the experiment.

The second system consists of a commercial dye laser (Continuum ND6000) with flowing Coumarin 480 dye, and a homebuilt dye laser in Littman configuration with flowing LDS 798 dye. The former is pumped by the third harmonic (355 nm) and the latter by the second harmonic (532 nm) of a Q-switched Nd:YAG laser (Quantel Brilliant B). The third harmonic has the energy of ~ 53 mJ/pulse. The second harmonic is separated from the fundamental using a dichroic mirror. The Continuum dye laser has energy of ~ 0.2 mJ/pulse at 481.5 nm with fresh dye. The bandwidth of the laser is less than 0.1 cm^{-1} . In the homebuilt dye laser a cylindrical lens focuses the pump beam to a narrow horizontal line just inside the cuvette for the dye. Care must be taken not to focus the beam on the cuvette too tightly for that can damage

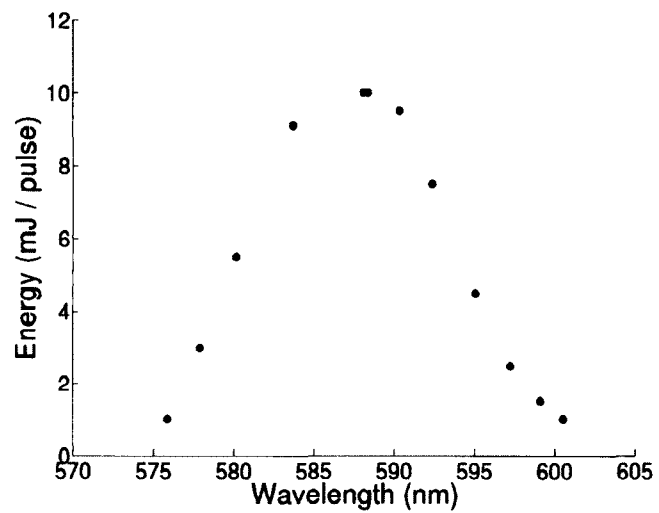


FIG. 14: Tuning curve of Continuum ND6000 laser with Rhodamine 6G dye.

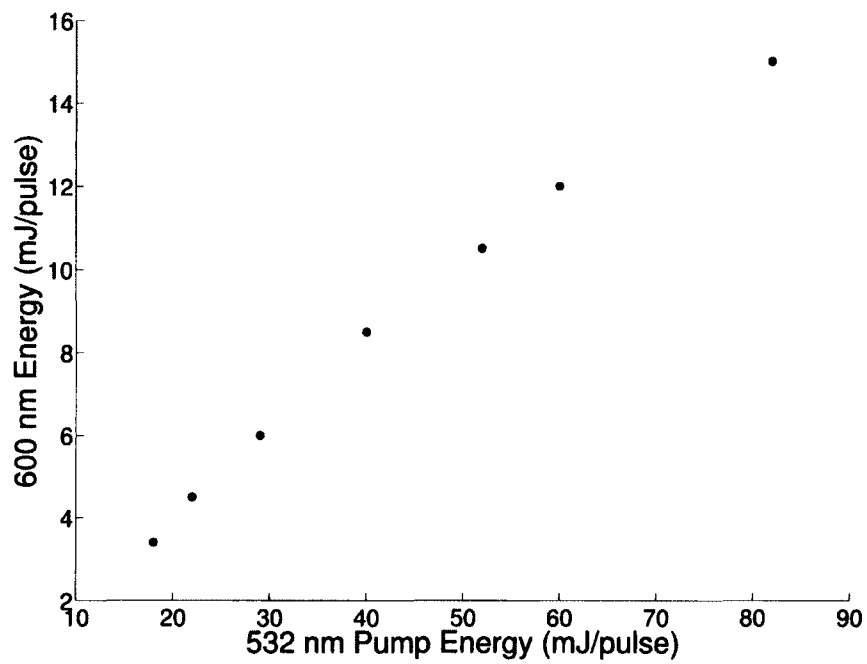


FIG. 15: Dye laser energy vs. pump laser energy.

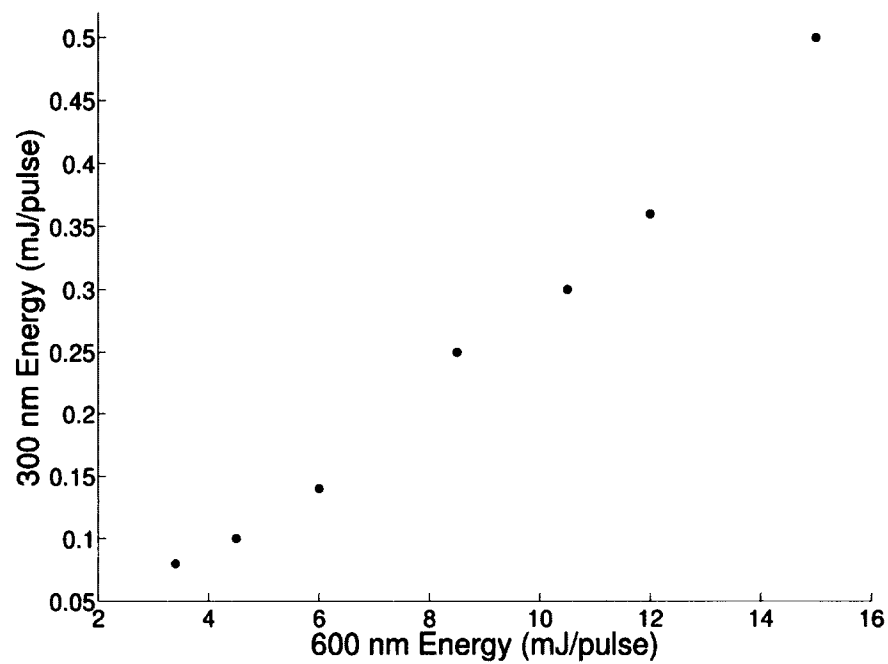


FIG. 16: The output laser energy from the frequency doubling crystal vs. the input laser energy.

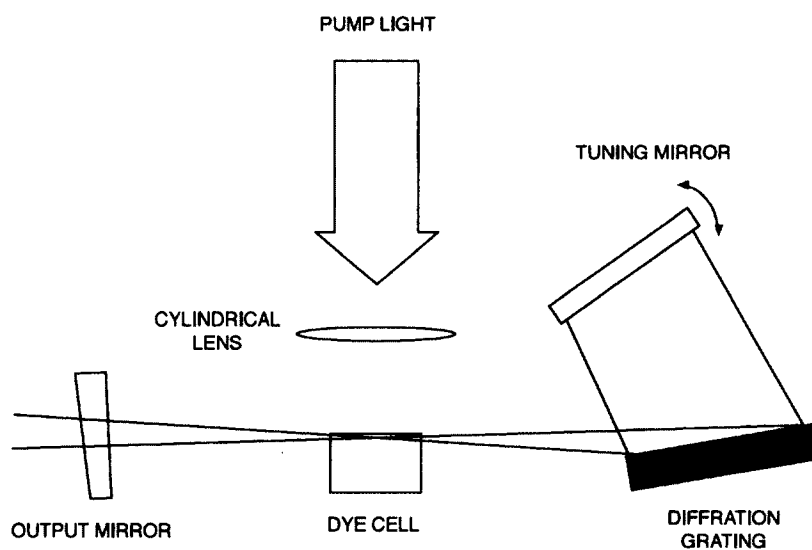


FIG. 17: Schematic drawing of homebuilt dye laser in Littman configuration [76].



FIG. 18: Tunable homebuilt dye laser.

the cuvette. The laser cavity is formed by the 4% reflecting wedged output mirror, a 1200 lines/mm diffraction grating, and a tuning mirror as schematically illustrated in Fig. 17. The assembled dye laser is shown in Fig. 18. The output beam is collimated with a lens of focal length 200mm (Thorlabs LB1945-B). The concentration of LDS 798 dye for this laser is 3.3×10^{-4} molar. The wavelength of the laser is tuned to 780 nm and its energy is $\sim 80 \mu\text{J}/\text{pulse}$ with the energy of the pump beam $\sim 200 \mu\text{J}/\text{pulse}$.

The schematic of the optical setup for the dye laser systems is given in Fig. 19. The 300 nm pulsed laser beam is focused onto the MOT with a quartz lens of focal length 200 mm. The lens is mounted on a translation stage for fine alignment required for overlapping the laser beam with the MOT. A half-waveplate is placed in the optical path to control its polarization. The 780 nm and 480 nm pulsed laser beams are combined using a dichroic beamsplitter. The transmission efficiency of the beamsplitter for 780 nm pulsed laser beam is $\sim 85\%$. Each beam has a half-waveplate in its optical path for setting the desired polarizations of the laser beams. The combined beam is then focused onto the MOT with an uncoated lens of focal length of 250 mm. This lens is also mounted on a translation stage.

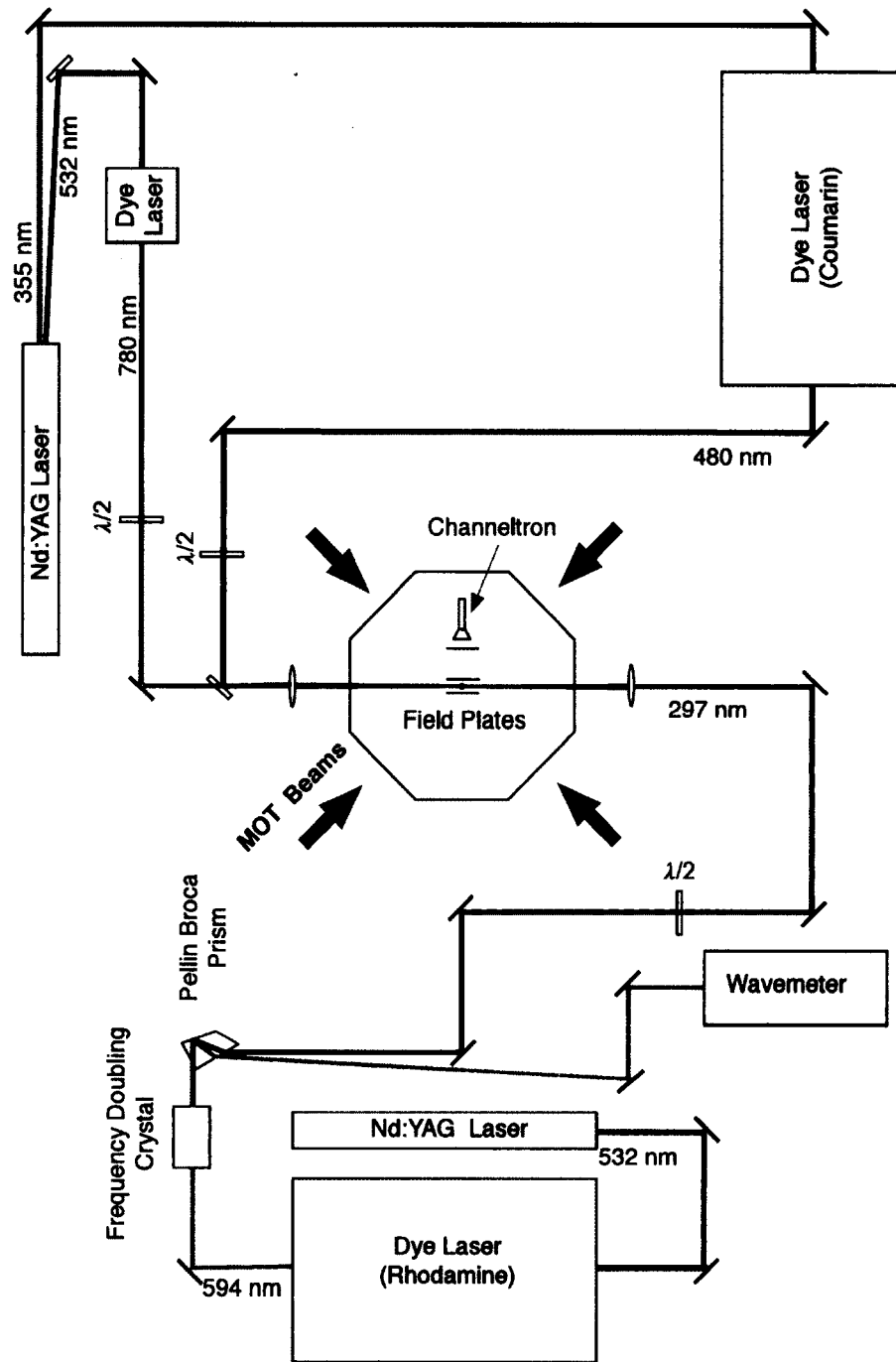


FIG. 19: The schematic diagram of the optical setup of the laser systems for excitation of Rydberg states. $\lambda/2$ stands for half-waveplate.

3.3 DETECTION OF RYDBERG ATOMS

For the detection of Rydberg atoms in different experiments two methods of detection were used: fluorescence detection method and ion detection method. Details of these detection methods will be discussed in the following subsections. Initially, the vacuum chamber for the magneto-optical trap was not equipped with any ion detection system. Therefore, fluorescence detection of the trap with a photomultiplier tube was first employed as the method of detection of Rydberg states for the early experiments. For Förster resonance experiments an ion detection system was installed in the vacuum chamber for the detection of Rydberg states using the field ionization detection method. The installation of the ion detection system was performed twice, the second time with an improved configuration for the detection of Rydberg states. The details of the configurations of the ion detection system will be discussed in the subsection for ion detection.

3.3.1 FLUORESCENCE DETECTION

Rydberg spectroscopy was performed before an ion detection system was installed in the vacuum chamber. Fluorescence detection of trap loss was employed as a detection method for the spectroscopy. Fluorescence from the MOT is collected with a lens ($f = 50.8\text{mm}$) placed just outside one of the windows of the chamber. In order to block the unwanted background light from the chamber, a pinhole is placed where the image of the MOT is formed by this collection lens. Another lens ($f = 35\text{mm}$) is placed after the pinhole so that the collected fluorescence from the MOT becomes collimated. Collimation of the fluorescence signal is necessary for getting good efficiency of a bandpass filter (FL780-10 Thorlabs) that is placed in the signal collection path to further filter out the unwanted background signal: An angle of incidence other than zero will shift the central transmitted wavelength of a bandpass filter. Lastly, this filtered fluorescence is loosely focused onto a photomultiplier tube (R928 Hamamatsu) in order to mitigate the prospect of damaging it. The photomultiplier tube is connected to a current to voltage converter. From the knowledge of the scattering rate of atoms in the trap, the solid angle extended by the first lens, the transmission efficiency of the optics, and the quantum efficiency of the photomultiplier tube, the total number of the trapped atoms can be calculated [81]. The laser beam for exciting atoms in the trap to desired Rydberg states is focused onto

the MOT with a quartz lens ($f = 200$ mm). The schematic diagram of the optical setup for the fluorescence detection method is given in Fig. 20.

For performing Rydberg spectroscopy a detection technique known as trap loss spectroscopy was employed. As some of the atoms in the trap are excited to Rydberg states, they no longer participate in the cycling transition for cooling and trapping. Furthermore, a few atoms will ionize through resonantly enhanced multiphoton ionization. As a result, the number of atoms in the trap is reduced, and so is the fluorescence from the scattering of the trapped atoms, accordingly. Rydberg spectroscopy is thus achieved by monitoring the reduction in fluorescence signal from the magneto-optical trap as the frequency of the laser for the excitation of Rydberg states scans. For the two-step excitation to nD states, the trapping laser beams of 780 nm in wavelength themselves serve as the excitation laser beams for the first step ($5S_{1/2} \rightarrow 5P_{3/2}$). The pulsed laser beam from a dye laser (Continuum ND 6000) with Coumarin 480 dye is used as the second step excitation laser beam for creating nD Rydberg states. As this second step laser is scanned in frequency, reduction in fluorescence signal from the magneto-optical trap is observed whenever atoms are excited to Rydberg states. The data acquisition process is as follows: the output signal from the photomultiplier tube is amplified with a preamplifier (SR 445A Stanford Research Systems), and the amplified signal is fed to a gated photon counter (SR 400 Stanford Research Systems). The wavelength of the dye laser is monitored with a pulsed laser wavelength meter (821 Series, Bristol Instruments) with absolute accuracy of ± 0.001 nm at 700 nm. The result of the trap loss spectroscopy is presented in Fig. 21 and is in excellent agreement with NIST atomic spectra database and also with the previous work [82].

Trap loss spectroscopy was also performed for nP states. The excitation pulsed laser beam is derived from a pulsed dye laser beam with wavelength of ~ 600 nm by frequency doubling it with a nonlinear crystal as described in the previous section. As this dye laser scans its frequency, the crystal must be constantly phase-matched to maintain the conversion efficiency. The timing sequence for the experiment is given in Fig. 22. The trigger ($t=0$) comes from the flash lamp synchronization output of the pump Nd:YAG laser. A hundred microseconds after the trigger, the MOT laser beams are turned off for three hundred microseconds so that all atoms in the trap will be in the ground state. The excitation pulsed laser comes $180\mu s$ after the trigger. A typical result of the trap loss spectroscopy for the nP states is presented in Fig.

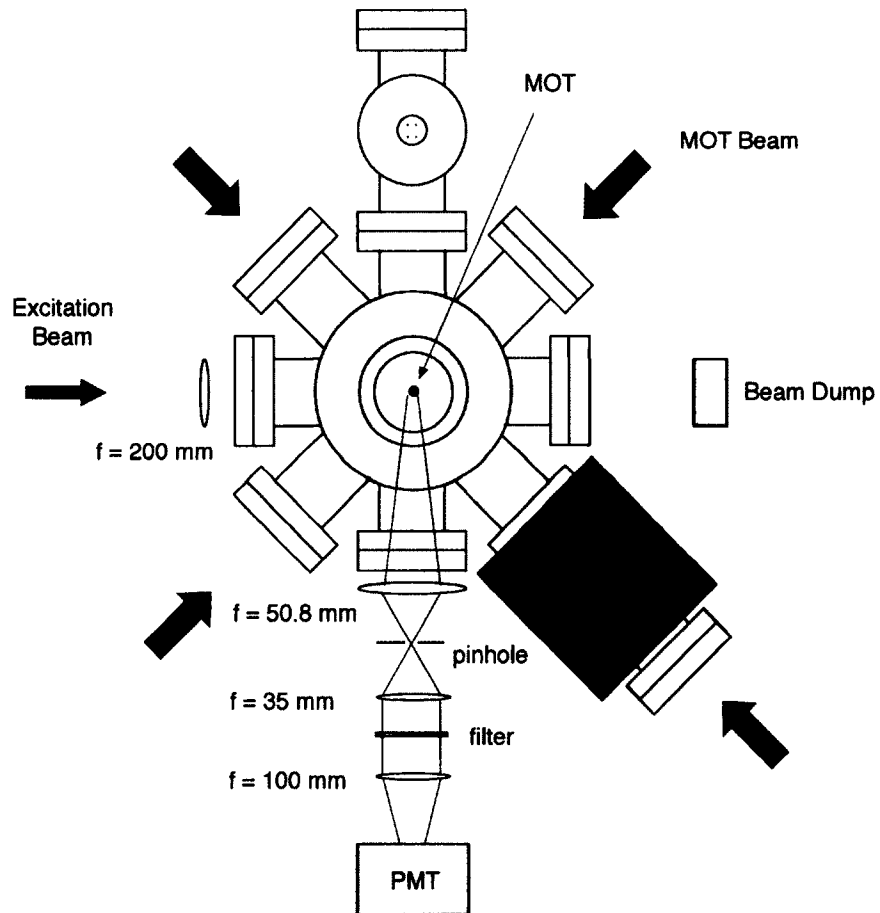


FIG. 20: Schematic diagram of the optical setup for fluorescence detection.

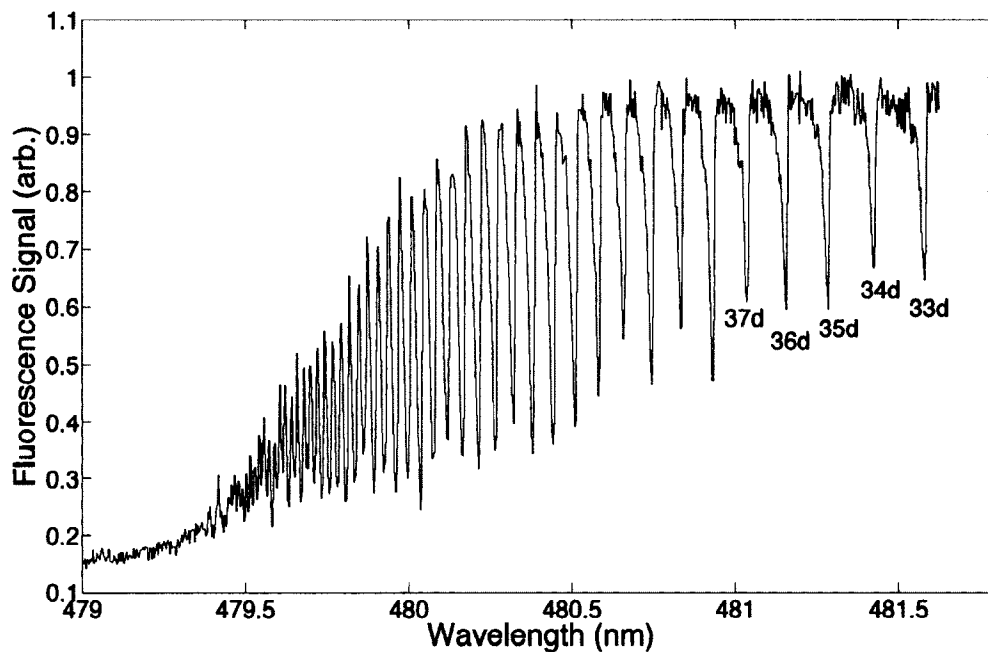


FIG. 21: A partial Rydberg spectrum of the nd series of ^{85}Rb obtained with the fluorescence detection method.

23, and is in excellent agreement with NIST atomic spectra database.

3.3.2 FIELD IONIZATION

The valence electron is weakly bound in Rydberg atoms. As a result, the application of even a modest electric field can ionize the Rydberg atoms. The detection of Rydberg states with field ionization method is highly efficient and state selective [1]. The ionization of Rydberg atoms with an external electric field can be explained using a model known as the saddle point model. The potential for the valence electron of the Rydberg atoms in an external field, E , in the z direction is given by (in atomic units)

$$V = -\frac{1}{|z|} + Ez. \quad (36)$$

It has a saddle point on the z -axis at $z = -1/\sqrt{E}$ with the value of $V = -2\sqrt{E}$, giving $E = V^2/4$. Ionization occurs when V is greater than or equal to the binding energy of the valence electron, $W = -1/2n^{*2}$. The threshold electric field for

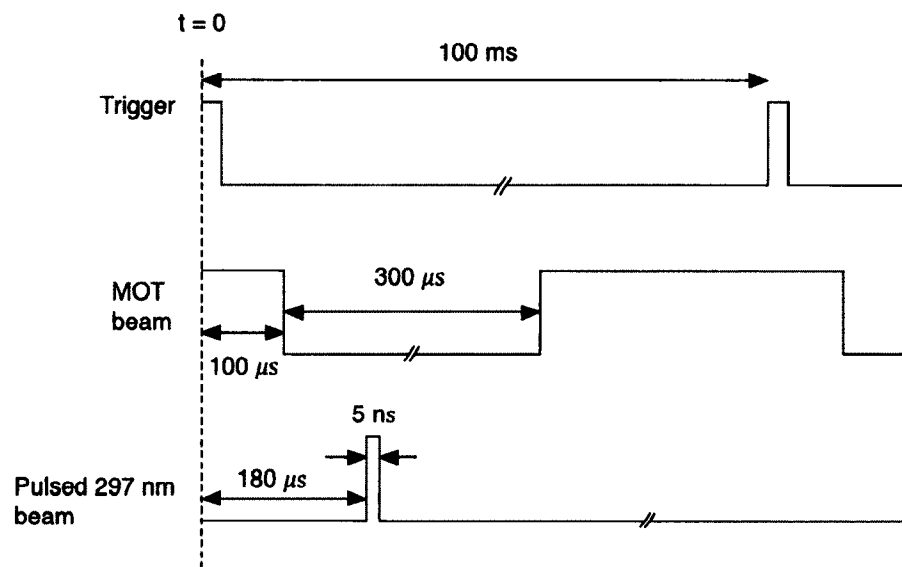


FIG. 22: Timing sequence for the trap loss spectroscopy for np series.

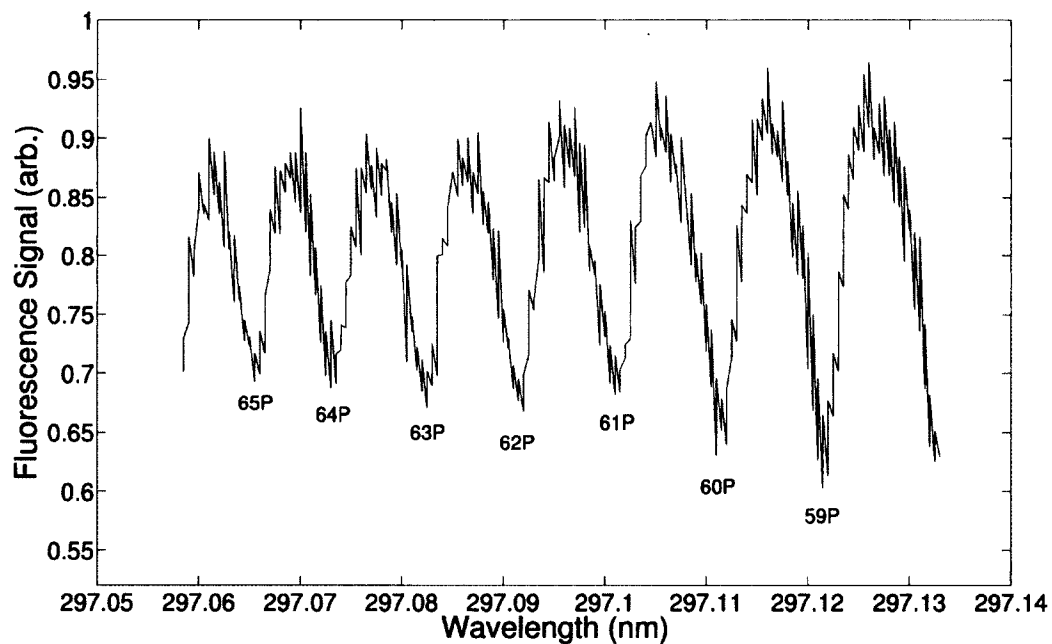


FIG. 23: A partial Rydberg spectrum of the np series of ^{85}Rb obtained with the fluorescence detection method.

ionization in terms of the binding energy is given by

$$E = \frac{W^2}{4}. \quad (37)$$

In terms of effective quantum number, n^* , it is given by

$$E = \frac{1}{16n^{*4}}. \quad (38)$$

The above expressions are only valid for $m = 0$ states. For $m \neq 0$ states, the centrifugal potential keeps the electron away from the z-axis raising the threshold field [83]. The fractional increase in the threshold field compared to the field for $m = 0$ is given by

$$\frac{\Delta E}{E} = \frac{|m|}{2n^*}. \quad (39)$$

Moreover, the saddle point model does not take into account the shift in energy of the states by the Stark effect. If the linear Stark effect is taken into account for the extreme red state with high n^* (the state whose energy is shifted down), the energy, W , is given by [53]

$$W = -\frac{1}{2n^{*2}} - \frac{3n^{*2}E}{2}, \quad (40)$$

and the threshold field is given by

$$E = \frac{1}{9n^{*4}}. \quad (41)$$

Differentiation of Rydberg states is achieved by feeding a square pulse with the pulse width of 400 μs from a high voltage pulse generator (DEI PVM 4210) into a RC-circuit. The circuit is tested at a low voltage to determine its time constant to be $\sim 8 \mu s$. The output of the RC-circuit is sent to one of the field plates installed in the vacuum chamber. The other field plate is held at ground potential during the field ionization phase of the experiment. As the electric field between the plates increases sufficiently, Rydberg states with higher n^* are ionized first followed by the ionization of states with lower n^* , thus providing time-resolved ion signals for different Rydberg states.

3.3.3 ION DETECTION

After the Rydberg atoms are field ionized, ions are collected by a channel electron

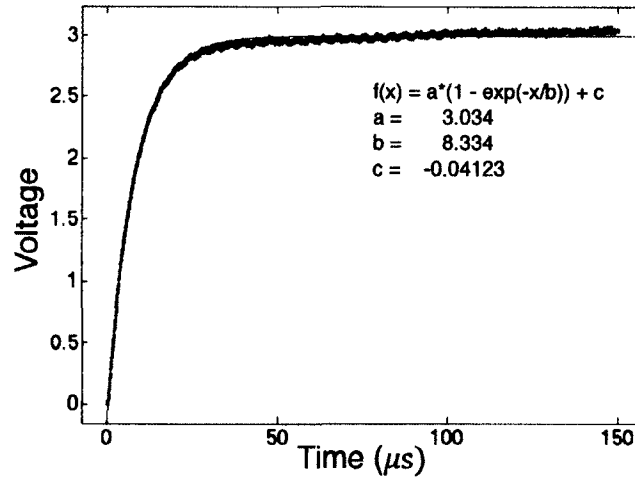


FIG. 24: The output signal of the RC circuit for measuring its time constant. The circuit is used in ion detection by the field ionization method.

multiplier (Dr. Sjuts Optotechnik KBL 10RS). A channel electron multiplier (CEM) has a high resistive surface that acts as a continuous dynode when a potential is applied between the input and output end of the CEM. A dynode emits secondary electrons when impinged upon by ions. These electrons are accelerated by the applied potential, and they impinge the dynode again producing further secondary electrons. The repeated process of impinging the dynode with particles produces an avalanche of electrons. The resulting electron cloud from the output of the CEM is accelerated through free space to the collecting anode with a bias voltage of $\sim 50\text{V}$. This is achieved by connecting an external resistor of $10\text{ M}\Omega$ in series with the CEM with the surface resistance of $\sim 200\text{ M}\Omega$. The collecting cone of the CEM is held at -1100V . The CEM has a gain of 10^8 and a pulse width of 8 ns .

As mentioned earlier, installation of the ion detection system was performed twice, each time for a different configuration of the electric field plates. The schematic diagrams of these configurations are given in Fig. 25. In the first configuration two steel plates of diameter of 3.3 cm are used as the field plates, and they are placed as close as possible to the magneto-optical trap without clipping the trap laser beams. The distance between them is about 4.6 cm . With this configuration of field plates, we were able to detect high Rydberg states as shown in Fig. 26. The sharp signal observed at $13.2\text{ }\mu\text{s}$ is due to free ions. Spectroscopy for Rydberg states

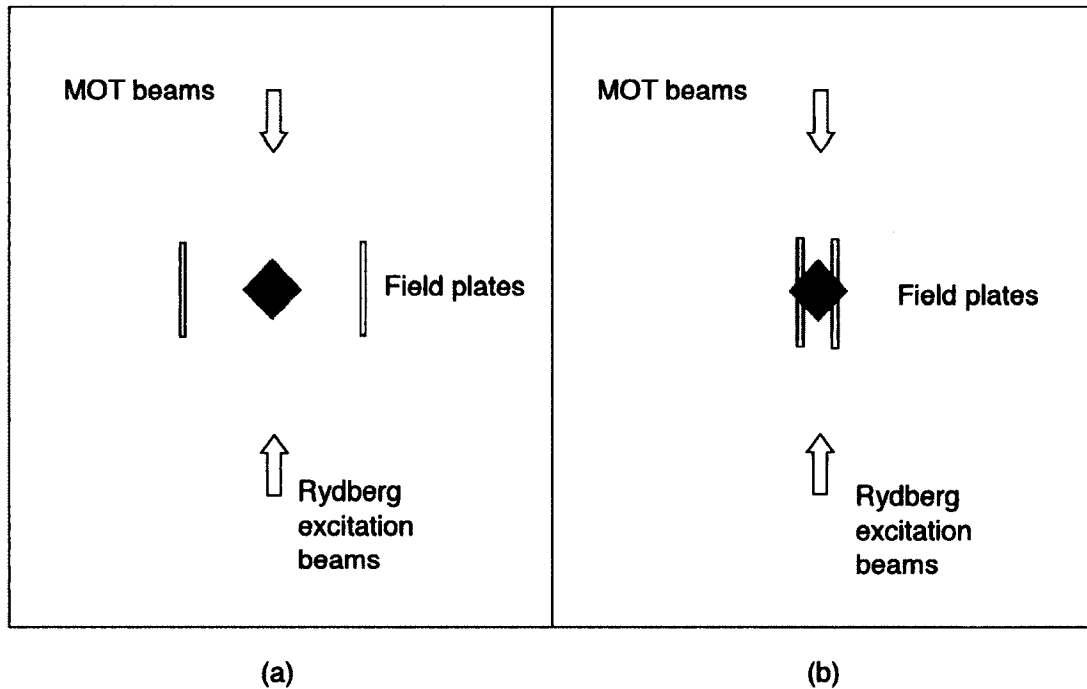


FIG. 25: Schematic diagram for the top view of the two configurations of electric field plates as part of the detection systems for Rydberg states by field ionization method (not to scale). (a) This field plates configuration was used in the first installation of ion detection system in the vacuum chamber. (b) The plates configuration for the second installation of ion detection system: steel plates were replaced with transparent wire meshes so that the separation between the plates can be made smaller for producing a uniform electric field between them.

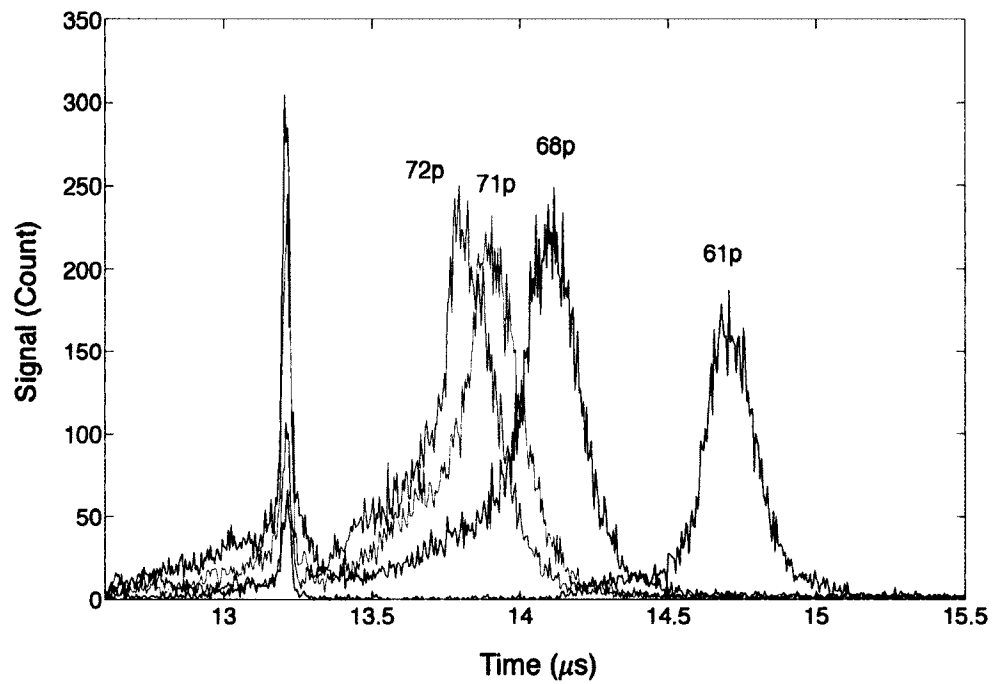


FIG. 26: Time-resolved signals of Rydberg states detected by the field ionization method with plate separation of ~ 4.6 cm. Detection of lower Rydberg states was not possible with this field plate configuration.

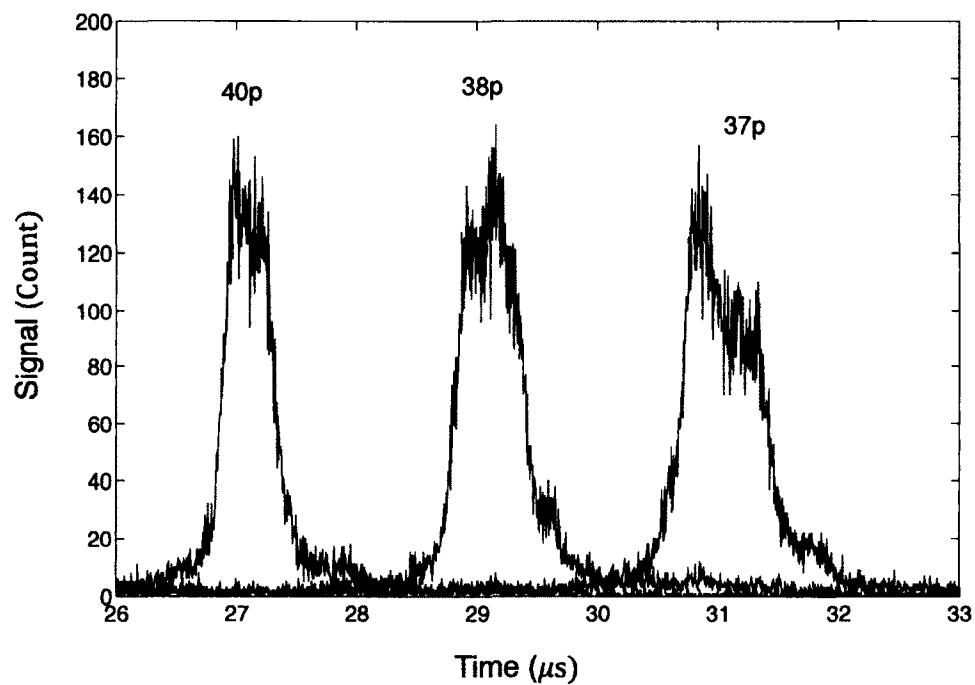


FIG. 27: Time-resolved signals of lower Rydberg states detected by the field ionization method with the final configuration of the field plates that has a separation of ~ 1.35 cm between them.

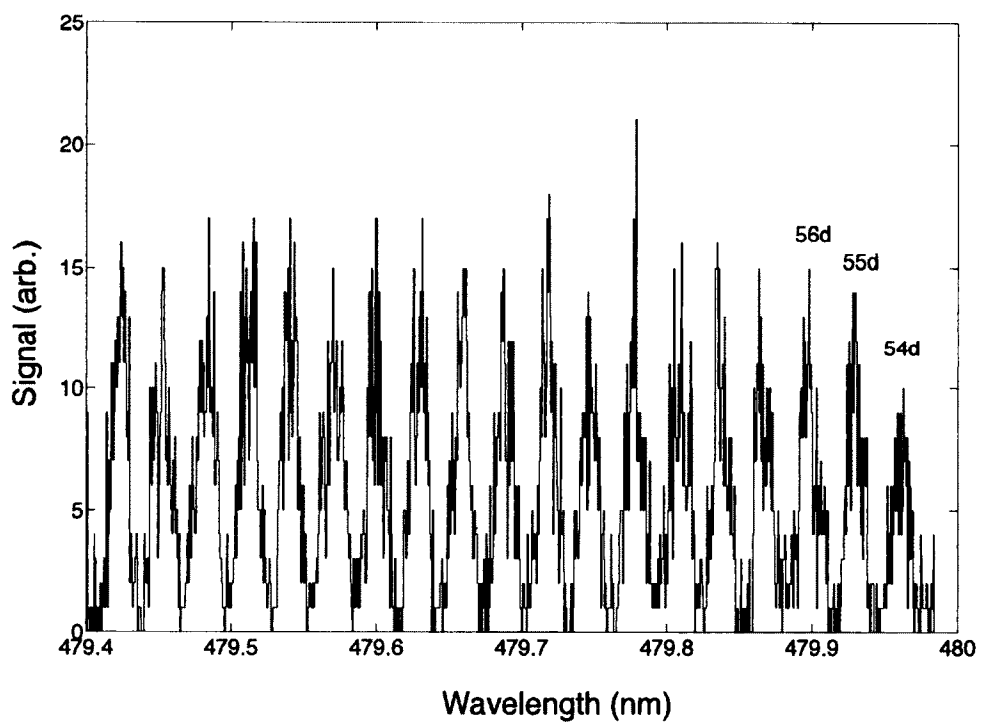


FIG. 28: A partial Rydberg spectrum of the nd series of ^{85}Rb obtained with the field ionization method.

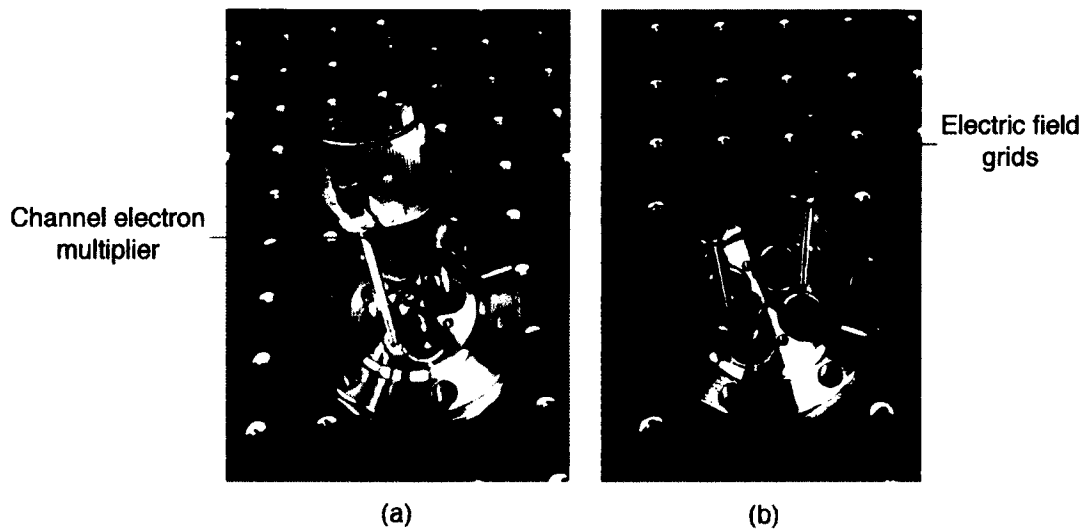


FIG. 29: Ion detection system before installation in the vacuum chamber. (a) The assembly for the channel electron multiplier. (b) The assembly of the plate used for field ionization of Rydberg atoms.

was also performed with this ion detection system and the result is given in Fig. 28. Detection of lower Rydberg states such as $44d$ with this field plates configuration was not possible since the required electric field to ionize a given state scales with $1/n^4$ and the separation of the plates in this configuration was too large for the high voltage pulse generator (DEI PVM 4210) to supply enough voltage for the required field. Although we were able to detect time-resolved higher Rydberg states, efforts to observe Stark-tuned Förster resonances were hindered by the fact that the electric field between the plates was non-uniform making the calibration of the field required to tune the Rydberg atoms into resonances rather difficult. We therefore decided to modify the field plates configuration to circumvent these difficulties as shown in (b) of Fig. 25.

The images of the assemblies of the ion detection system with the improved configuration of field plates, and the geometry of the system before installation in the vacuum chamber are presented in Fig. 29 and Fig. 30. Wire mesh field plates are used so that the two field plates can be positioned closely to have a uniform electric field around the region of the magneto-optical trap. This is achieved by inserting a fine nickel mesh (Industrial Netting BM 0020-01-N) between two slotted stainless steel plates each of which has the diameter of 1.3 in. The nickel mesh has

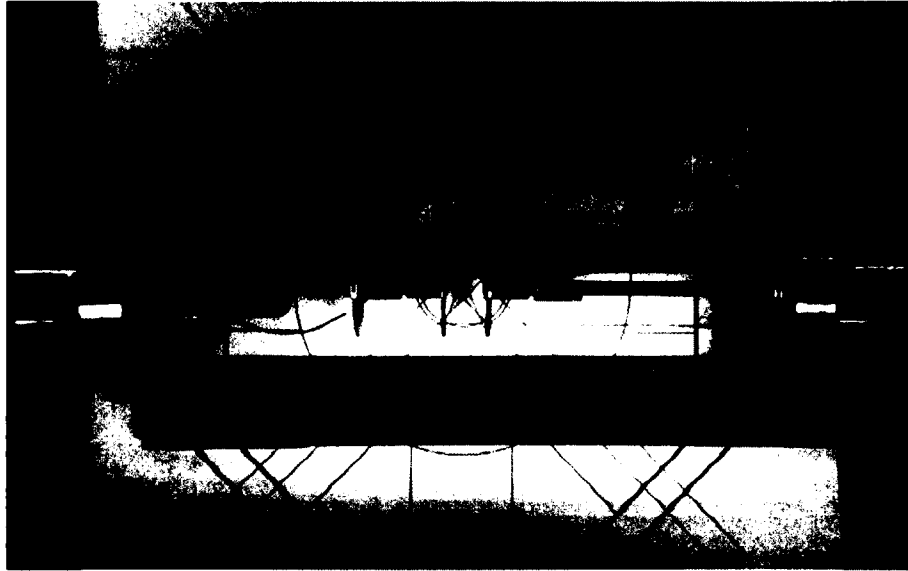


FIG. 30: Geometry of the ion detection system. The magneto-optical trap beams enter the central region of the vacuum chamber through the slots in the steel plates covered with transparent nickel mesh.

20 wires per inch, and the thickness of 0.00363 in, and the maximum transmission of 86 percent. The separation between the two field plates is 1.35 cm. The plates are electrically isolated from the chamber with ceramic standoffs and washers. The electrical connections are made through high voltage feedthroughs. In the channel electron multiplier assembly, there is another field plate in front of the cone of the CEM to shield the magneto-optical trap from any electric field from it since it is kept at a high voltage. This stainless steel field plate has a 10 mm diameter opening in the center covered with a stainless steel mesh for the passage for ions to the collecting cone of the CEM. Both plates in the CEM assembly are kept at the same potential. With this configuration of field plates, lower Rydberg states can now be detected as shown in Fig. 27.

We observed that the signals of the Rydberg states varied either with the density of the trap or the intensity of the excitation pulsed laser beam. At higher densities of the trap or higher intensities of the excitation laser beam multiple states were observed even though the wavelength of the excitation laser was set to excite a particular state. We have investigated this effect first by varying the density of the trap, and then by varying the intensity of the excitation laser beam. The density

of the trap was varied with the intensity of the trap laser beams. The wavelength of the laser was set to 480.38 nm for excitation to $45d$ state. The energy of the laser is $60 \mu\text{J}/\text{pulse}$. The intensity of the trapping laser beam was varied from $9 \text{ mW}/\text{cm}^2$ to $38 \text{ mW}/\text{cm}^2$. The results are given in Fig. 31. In the next experiment, the intensity of the excitation laser beam was varied from $20 \mu\text{J}/\text{pulse}$ to $90 \mu\text{J}/\text{pulse}$ while the density of the trap was kept constant with the intensity of the trapping laser beams of $38 \text{ mW}/\text{cm}^2$. The results are given in Fig. 32. The ion signal at $198.2 \mu\text{s}$ was observed in all cases. Tanner et al. have reported similar observations, and provided an explanation. The pair state $nd + nd$ is nearly degenerate with the pair state $(n+2)p + (n-2)f$ which in turn is coupled with other pair states composed of atomic states of higher and lower energy. In a high density Rydberg gas, the atomic population quickly diffuses over a band of levels [84].

3.3.4 EXPERIMENTAL TIMING SEQUENCE

The flash lamp synchronization output from one of the Nd:YAG lasers (Quantel Brilliant Eazy) triggers the timing sequence of the experiment. It triggers a digital delay pulse generator (Quantum Composer 9614) that controls the timing sequence. It also triggers the flash lamp of the other Nd:YAG laser, the Q-switch of which is internally triggered. This triggering scheme for the Nd:YAG lasers has a delay of 2.3 to $3 \mu\text{s}$ so that if their Q-switches are set to trigger internally at the same time one of the optical pulses will arrive at a later time. This delay was accounted for when setting triggering time for the Q-switches so that the pulses were not more than $1 \mu\text{s}$ apart in time. After the delay of $180 \mu\text{s}$ from the flash lamp trigger, the MOT beams for the cooling transition are turned off for $100 \mu\text{s}$. The repumper beam is turned off for $500 \mu\text{s}$ immediately after the trigger. The Q-switch of the Nd:YAG laser used for the generation of 297.7 nm pulse for $5S \rightarrow 34P$ is set at $189 \mu\text{s}$ after the flash lamp trigger. The Q-switch of the other ND:YAG laser used for the generation of 780 nm and 480 nm pulses for $5S \rightarrow 5P \rightarrow 34D$ two-step transition is set at $187 \mu\text{s}$. The Rydberg atoms created are tuned into resonances via the Stark effect. This Stark-tuning pulse of variable pulse width is turned on $190 \mu\text{s}$ after the trigger. After this, the field ionization pulse of pulse width $400 \mu\text{s}$ is turned on for the detection of Rydberg atoms. The maximum amplitude from the pulse generator is 5V . To achieve the necessary voltage for the Stark tuning, the pulse from the pulse generator is amplified with a fast operational amplifier (OPA 453-TA). The

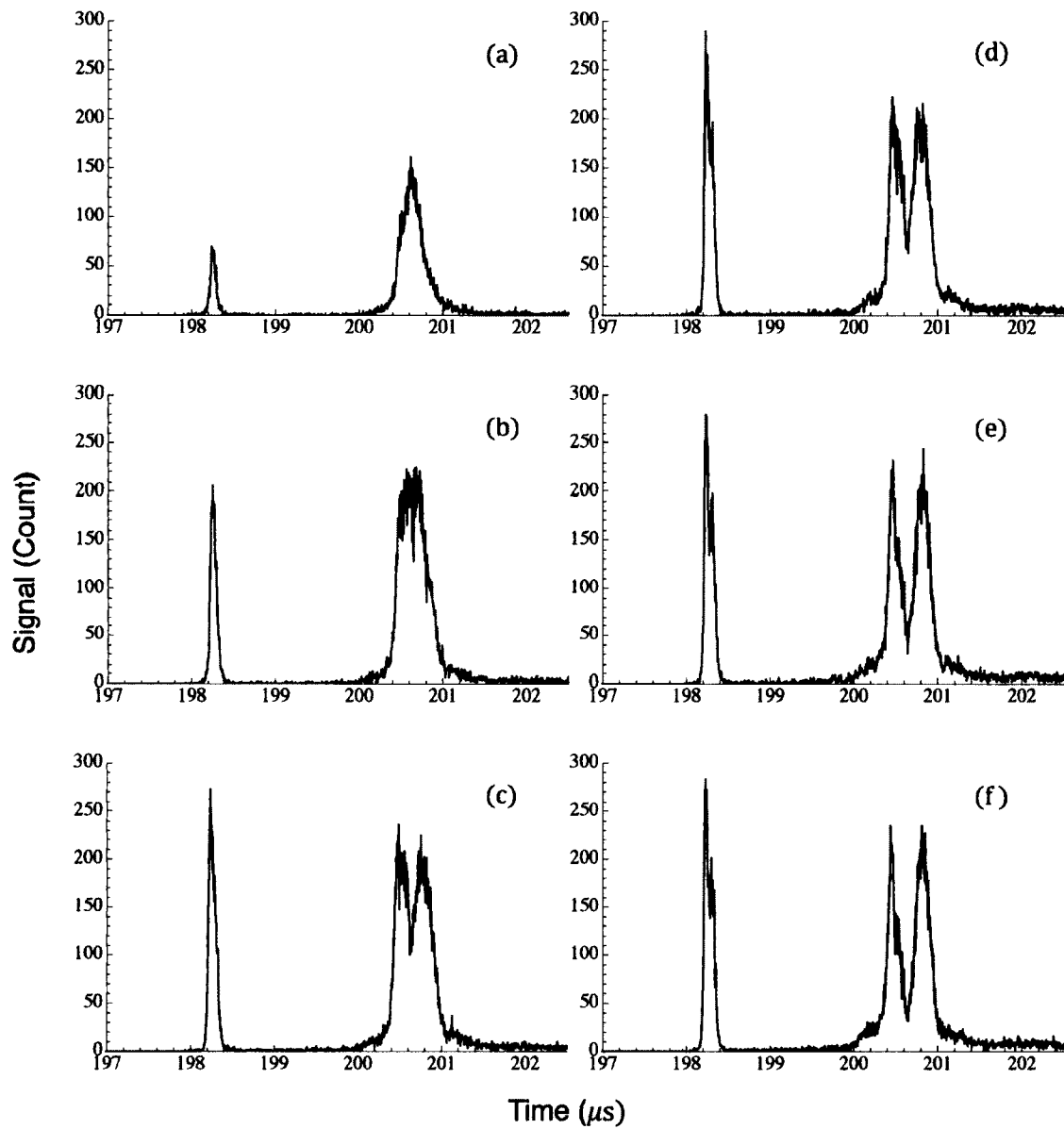


FIG. 31: Signals of the $45d$ state at various densities of the magneto-optical trap. The sharp signal at $198.2 \mu\text{s}$ is due to free ions. The trap density is varied with the intensity of the trap laser beams. The intensities from (a) to (f) are $\sim 9, 15, 20, 26, 30, 35,$ and 38 mW/cm^2 respectively.

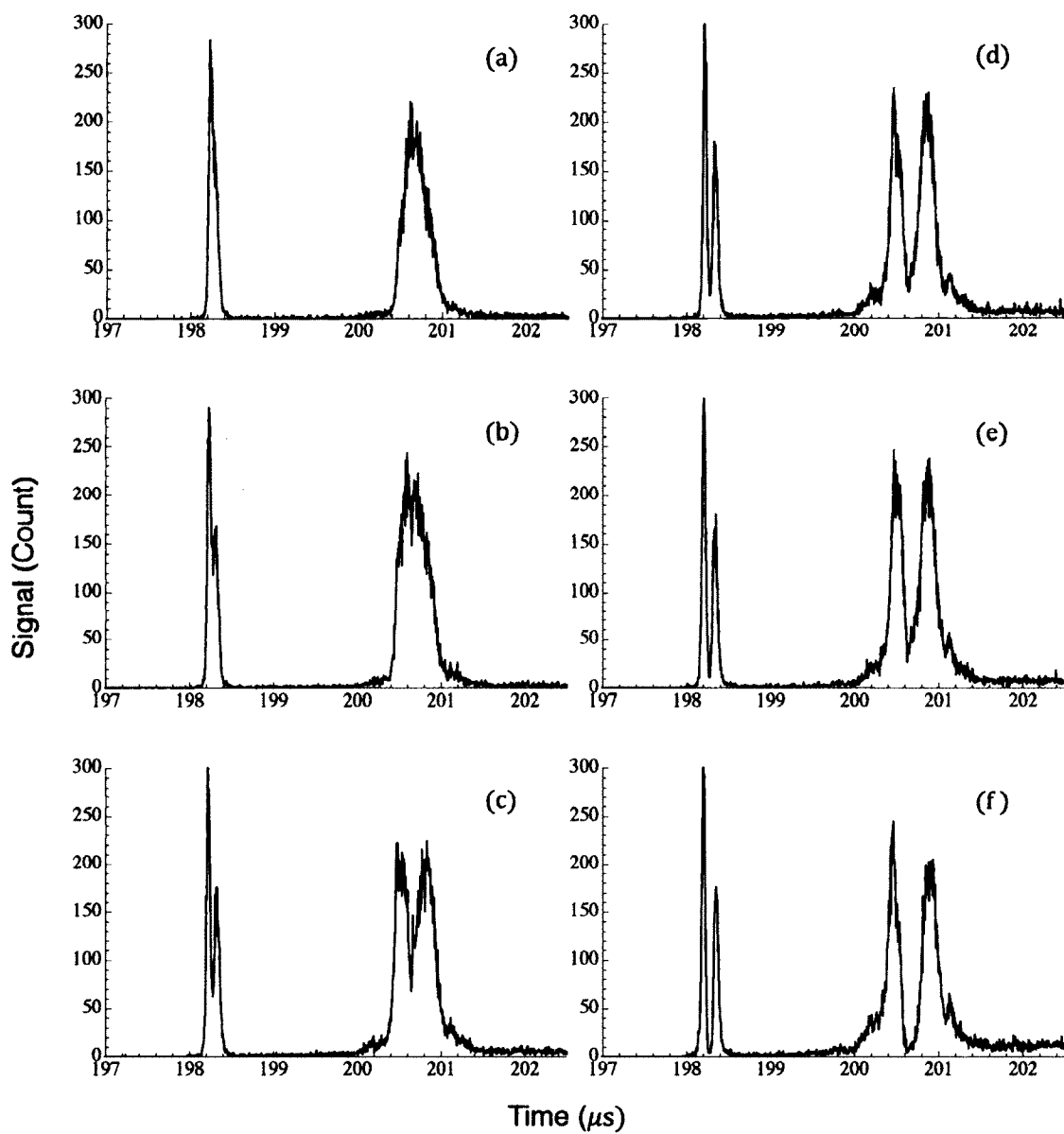


FIG. 32: Signals of the $45d$ state at various energies of the excitation pulsed laser beam. The energies from (a) to (f) are $\sim 20, 30, 40, 60, 75,$ and $90 \mu\text{J}/\text{pulse}$ respectively.

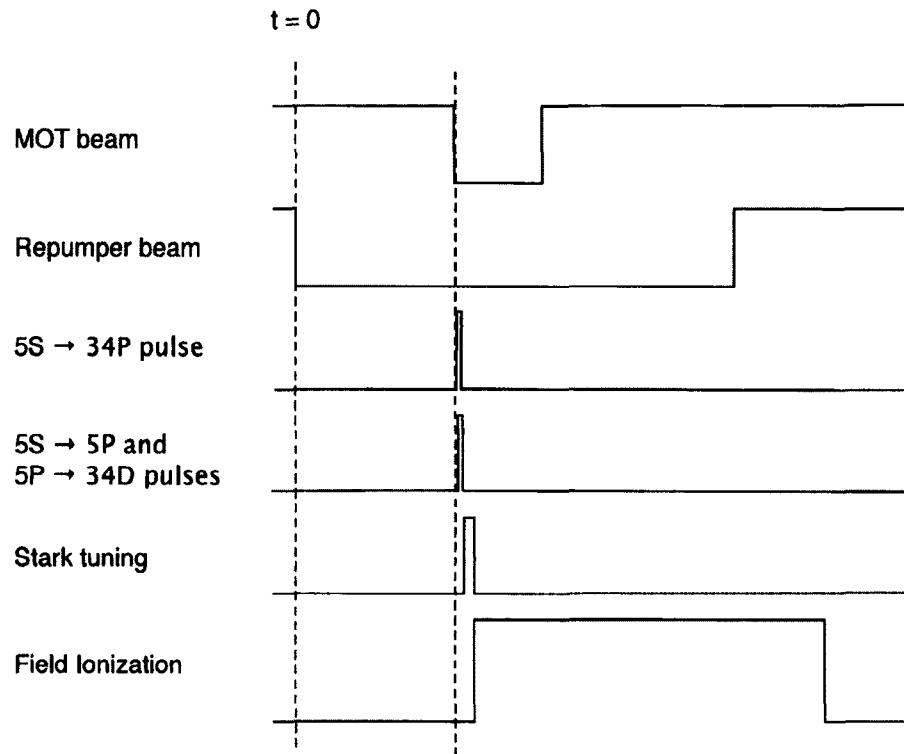


FIG. 33: Experimental timing sequence (not to scale).

experimental timing sequence diagram is given in Fig. 33.

CHAPTER 4

RESULTS AND ANALYSIS

In this chapter the results and analysis of a set of experiments to investigate Stark-tuned Förster resonances in ^{85}Rb will be presented and discussed. First, the observation of Stark-tuned Förster resonances for different m_j values of the reaction $34p_{3/2} + 34p_{3/2} \rightarrow 34s_{1/2} + 35s_{1/2}$ will be discussed. Then the results of the experiments for the different interaction times for the reaction will be discussed. In these experiments Rydberg atoms of states $34d$ were introduced to the reaction, and we have observed an increase in the production of $34s_{1/2}$ Rydberg atoms. The interaction of $34d$ atoms among themselves cannot produce $34s_{1/2}$ atoms since it is forbidden by the dipole selection rule of $\Delta l = \pm 1$. The reaction of $34d + 34p \rightarrow np + 34s$ for some n is also very unlikely since the electric fields are specifically tuned for resonances of $34p_{3/2} + 34p_{3/2} \rightarrow 34s_{1/2} + 35s_{1/2}$ reaction. However, the reaction $34p + 34d \rightarrow 34d + 34p$ is resonant at all electric fields, and it can act as the catalysis in the production of $34s_{1/2}$ atoms. The comparison of the $34s_{1/2}$ atoms population with and without $34d$ in the reaction will be presented. A model for the population of $34s_{1/2}$ atoms for different interaction times for the reaction will be described and the result will be compared with the experimental data.

4.1 OBSERVATION OF STARK-TUNED FÖRSTER RESONANCES

We have observed Stark-tuned Förster resonances for different projection quantum number m_j values of $34p_{3/2} + 34p_{3/2} \rightarrow 34s_{1/2} + 35s_{1/2}$. The selection rules for the reaction are $\Delta l = \pm 1$ and that the total $M_j = m_{j1} + m_{j2}$ is conserved [67]. For example, the reaction $34p_{3/2,3/2} + 34p_{3/2,-3/2} \rightarrow 34s_{1/2,1/2} + 35s_{1/2,-1/2}$ is allowed. Here we use the symbol nl_{j,m_j} to represent principal, orbital, total angular momentum, and the projection of the total angular quantum numbers. The calculated electric fields for the observed Förster resonances are listed in Table 5. The pair states $34p_{3/2} + 34p_{3/2}$ and $34s_{1/2} + 35s_{1/2}$ are 572.5 MHz apart in energy at zero electric field. The Stark structure of the pair states reveals the crossings of the energy levels at the fields for Förster resonances as shown in Fig. 34. The energy level crossings

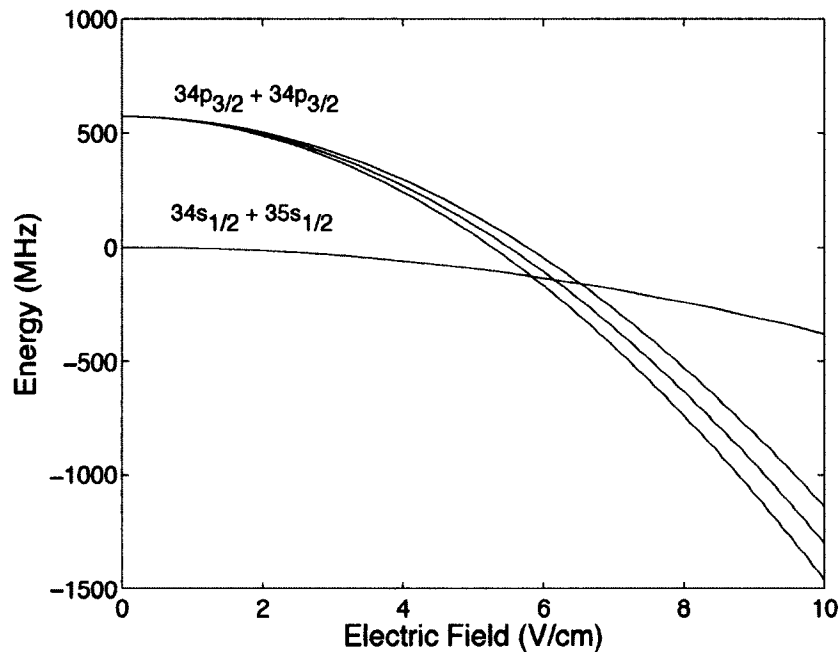


FIG. 34: Stark structures of the pair states. Förster resonances are observed at the fields where the level crossings occur.

do not occur for the pair states with $34p_{1/2}$, and accordingly there are no Förster resonances for the pair states with $34p_{1/2}$.

The general timing sequence for the experiment is described in the last section of Chapter 3. For the observation of Stark-tuned Förster resonances the procedure for the data collection is as follow. The trap beams are turned off $180 \mu\text{s}$ after the trigger. The pulsed laser beam for excitation of atoms in the trap from $5s_{1/2}$ to $34p_{3/2}$ is turned on $189 \mu\text{s}$ after the trigger. The electric field between the plates for tuning the resonances is turned on 100 ns after the excitation for the interaction time of $8 \mu\text{s}$ for this experiment. The Rydberg atoms are then detected with the pulsed field ionization method. The time constant of the pulsed field is $\sim 8.3 \mu\text{s}$. The time-resolved ion signals are then collected with a channel electron multiplier (Dr. Sjuts Optotechnik KBL 10RS). The signals are then amplified with a preamplifier (SR445A Stanford Research Systems) and collected with a multichannel scaler/averager (SR430 Stanford Research Systems). The time-resolved signals of Rydberg states for the reaction $34p_{3/2} + 34p_{3/2} \rightarrow 34s_{1/2} + 35s_{1/2}$ for both resonant and non-resonant electric fields

TABLE 5: The values of electric fields for the Förster resonances.

Process	Electric field for resonance (V/cm)
$34p_{3/2, 1/2 } + 34p_{3/2, 1/2 } \rightarrow 34s_{1/2} + 35s_{1/2}$	5.83
$34p_{3/2, 3/2 } + 34p_{3/2, 1/2 } \rightarrow 34s_{1/2} + 35s_{1/2}$	6.16
$34p_{3/2, 3/2 } + 34p_{3/2, 3/2 } \rightarrow 34s_{1/2} + 35s_{1/2}$	6.53

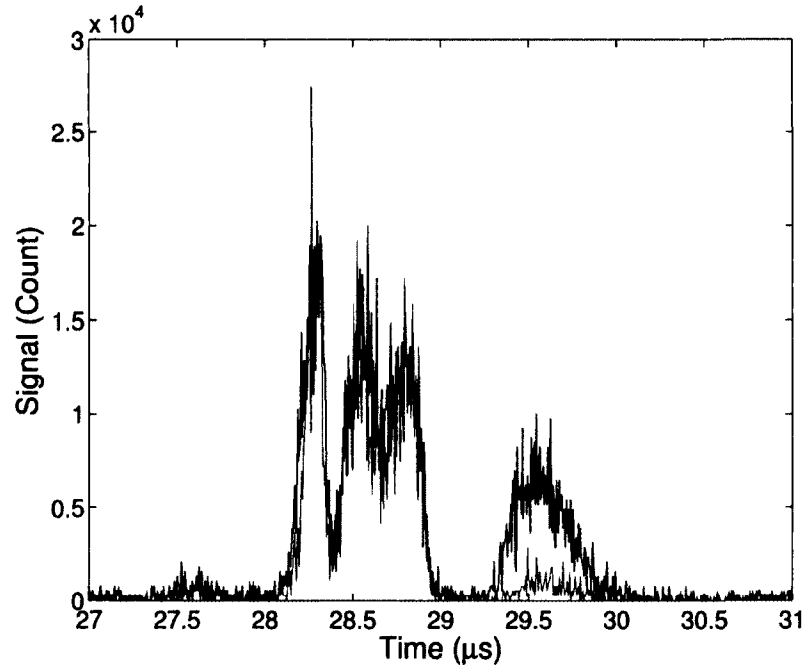


FIG. 35: Time-resolved signals of Rydberg states for the process $34p_{3/2} + 34p_{3/2} \rightarrow 34s_{1/2} + 35s_{1/2}$. The signal in blue is for the resonant electric field, and the signal in red is for the non-resonant electric field.

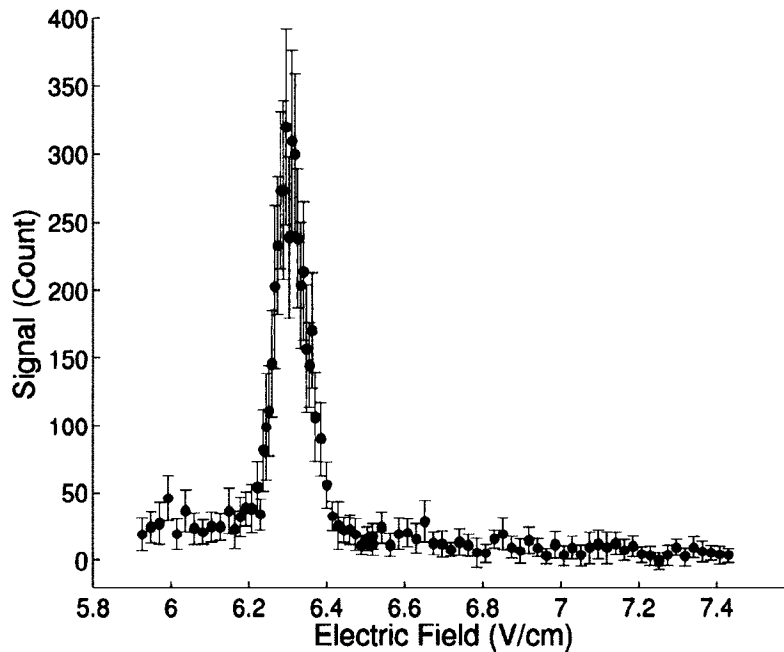


FIG. 36: Förster resonance for the process $34p_{3/2,|1/2\rangle} + 34p_{3/2,|1/2\rangle} \rightarrow 34s_{1/2} + 35s_{1/2}$. The polarization of the excitation laser beam is set to be in the z direction.

are presented in Fig. 35. Although the reaction requires a $35s$ atom for every $34s$ atom, we observed that there are many more $34s$ atoms than $35s$ atoms detected at the resonant field. The tuning electric field is varied from 5.9 V/cm to 7.4 V/cm in each data collection, and we performed a total of eight such data collection, each time randomly varying the values of the tuning electric field to minimize systematic errors. The resulting signals are then added together. Typical added signals for the Rydberg states are given in Fig. 35. The signal in blue is for the resonant interaction and the signal in red is for the non-resonant interaction. The polarization of the excitation pulsed laser beam is controlled with a half-waveplate. Taking the direction of the tuning electric field to be in z direction, the propagation of the excitation laser beam is in the y direction.

In the first experiment the polarization of the excitation laser beam was set to be in the z direction, and Förster resonance for $34p_{3/2,|1/2\rangle} + 34p_{3/2,|1/2\rangle} \rightarrow 34s_{1/2} + 35s_{1/2}$ was observed at the electric field of 6.3 V/cm which is higher than the calculated value of 5.83 V/cm. In the second experiment the polarization was set to be in the

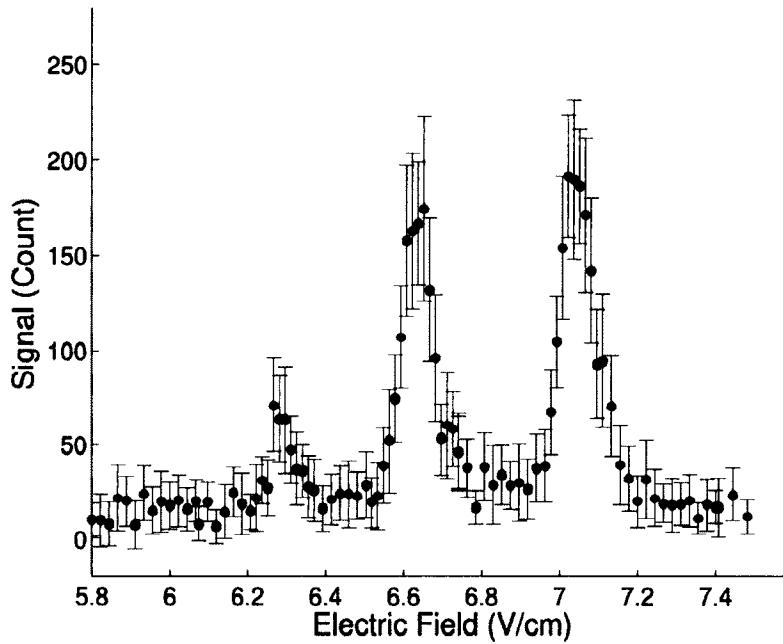


FIG. 37: Förster resonances. The polarization of the excitation laser beam is set to be in the x direction.

x direction, and all three resonances were observed at the electric fields of 6.3 V/cm, 6.6 V/cm, and 7.1 V/cm respectively. They are all about 0.5 V/cm higher than the calculated values. It could be because of the uncertainty in the measurement of the distance between the field plates. The results of the experiments are presented in Fig. 36 and Fig. 37. The signal here is the total counts of the $34s$ state atoms for a given electric field. These results are in good agreement with similar experiments on resonant dipole-dipole energy transfer in cold Rydberg gas, for example by Anderson et al. [20] and Carroll et al. [30]. They reported observation of the linewidths of the resonances on the order of 10 MHz which is much higher than the expected linewidths on the order of kHz at the temperature of $300 \mu\text{K}$ in the binary interaction picture. They attributed this broadening of linewidth to many-body interactions in cold Rydberg gas. Such cold Rydberg gases are known as frozen Rydberg gases for the Rydberg atoms move only a few percent of their interatomic spacing during the experimental time scale of a few microseconds. Mourachko et al. investigated many-body interactions in a frozen Rydberg gas by introducing an additional Rydberg state that does not participate directly in the energy transfer process, but is strongly

coupled to one of the final states [28]. They observed broadening of the resonances due to the additional Rydberg atoms of 34s state.

4.2 CATALYSIS OF STARK-TUNED INTERACTIONS

In this set of experiments we investigate both the catalysis of Stark-tuned interactions by introducing additional Rydberg atoms of 34d state to the energy transfer process that we have been studying, and the interaction time dependence of the energy transfer process. The process under investigation has three interaction channels:

$$34p + 34p \rightarrow 34s + 35s, \quad (42)$$

$$34p + 34s \rightarrow 34s + 34p, \text{ and} \quad (43)$$

$$34p + 35s \rightarrow 35s + 34p. \quad (44)$$

By introducing Rydberg atoms of 34d state another always resonant channel is added to the energy transfer process although these atoms do not directly participate in the process of equation (42).

$$34p + 34d \rightarrow 34d + 34p. \quad (45)$$

We have investigated the interaction time dependence of the 34s state population for all three Förster resonances. For each resonance, we have also investigated the catalysis effect of adding 34d state atoms in the interaction. The timing sequence for the experiment is the same as before except varying the interaction time before field ionizing the Rydberg atoms for detection, and the inclusion of pulsed laser beams for exciting atoms to 34d state for investigating the catalysis effect. These laser beams are turned on $\sim 0.5\mu\text{s}$ after the pulsed laser beam for excitation of 34p state is turned on. The polarization of the laser beam for excitation of 34p state is set to be in the x direction as before since all three resonances can be observed in this polarization, and the polarizations for the rest of the pulsed lasers are set to be in the z direction. The interaction time was varied randomly from 100 ns to 55 μs for each data collection, and we performed 33 data collections for each Förster resonance. The data with the 34d state included in the interaction and the data without the 34d included in the interaction were taken right after one another so that both would have similar experimental conditions such as density of the MOT and the energy of the pulsed

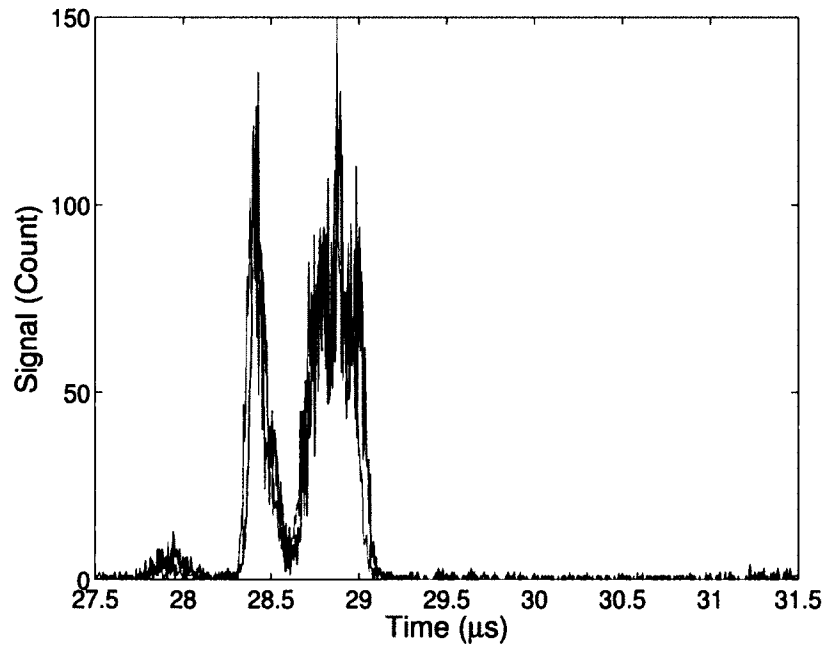


FIG. 38: The signals for $34d$ state for the interaction time of $7\mu\text{s}$. The signal in blue is for the electric field set to the resonant value for the process $34p_{3/2,|m_j|=1/2} + 34p_{3/2,|m_j|=1/2} \rightarrow 34s_{1/2} + 35s_{1/2}$. The signal in red is for a non-resonant electric field for the process.

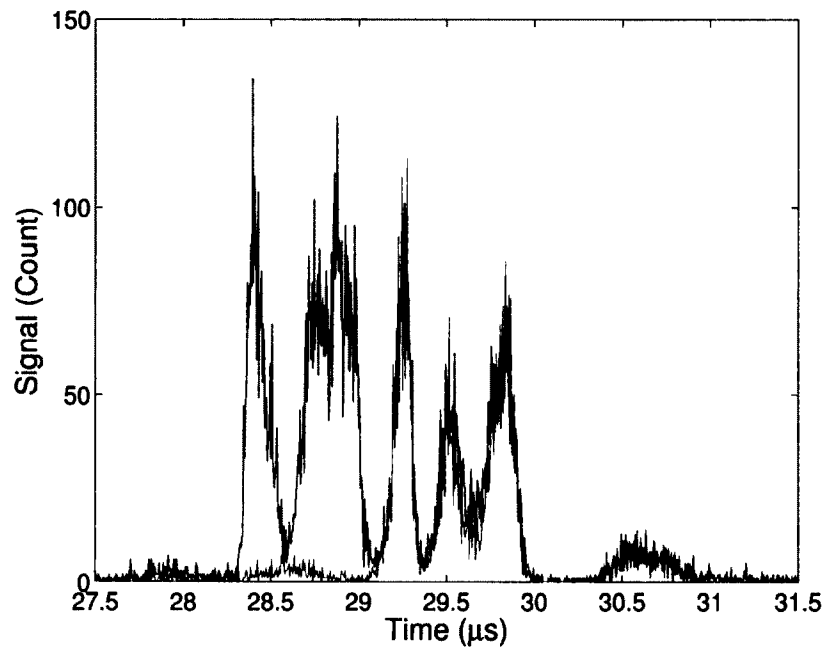


FIG. 39: The signals of Rydberg states $34d$ and $34p$ for the interaction time of $7\mu\text{s}$ in a non-resonant electric field. The signal in red is for the interaction without $34d$ state Rydberg atoms, and the signal in blue is for the interaction with $34d$ state Rydberg atoms included.

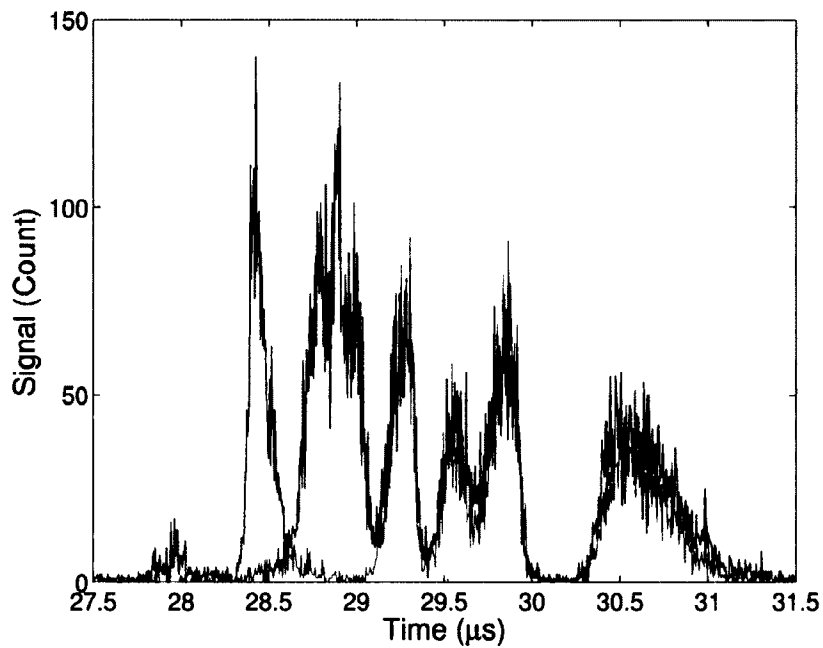


FIG. 40: The signals of Rydberg states $34d$, $34p$ and $34s$ for the interaction time of $7\mu\text{s}$ in the resonant electric field for $34p_{3/2,|m_j|=1/2} + 34p_{3/2,|m_j|=1/2} \rightarrow 34s_{1/2} + 35s_{1/2}$. The signal in red is for the interaction without $34d$ state Rydberg atoms, and the signal in blue is for the interaction with $34d$ state Rydberg atoms included.

laser beams. The energy of the pulsed laser beam for $34p$ excitation varied from ~ 0.3 mJ/pulse to 0.7 mJ/pulse for each data collection. The energy of the 780 nm and 480 nm pulse laser beams for the excitation of the $34d$ state were ~ 25 μ J/pulse and ~ 15 μ J respectively. The data were taken over several days and the experimental conditions were not exactly the same from day to day. Therefore, we resorted to taking as much data as possible and averaging them.

In Fig. 38, the $34d$ state signals for the interaction time of 7μ s is given. The signal in blue is for the electric field set to the resonant value for the process $34p_{3/2,|1/2\rangle} + 34p_{3/2,|1/2\rangle} \rightarrow 34s_{1/2} + 35s_{1/2}$. The signal in red is for a non-resonant electric field for the process. It can be seen that there is no signal of $34s$ due to $34d$ for both electric fields. In Fig. 39, the typical signals of $34p$ and $34d$ states for interaction time of 7μ s in a non-resonant electric field is given. The signal in red is for the interaction without the $34d$ state included, and the signal in blue is with $34d$ state included. Since the interaction is not resonant in this case, $34s$ state signal is not very large. The presence of $34d$ state in the interaction also does not appear to affect the nature of this non-resonant interaction. Typical signals of Rydberg states with the electric field tuned to the resonance is given in Fig. 40. The signal in red is for the interaction without $34d$ state atoms included, and the signal in blue is with $34d$ s state atoms included. Since, it is now a resonant interaction, a larger signal for $34s$ state is observed. It is also observed that the inclusion of $34d$ state in the interaction increases the population of $34s$ state atoms. The alignment for overlapping the excitation laser beams is critical for the observation of such effect.

The result of the experiment for the first resonance is given in Fig. 41. The data in symbol \times is for the interaction without the $34d$ state and the data in \blacklozenge is for the interaction with the $34d$ state. The $34s$ population is the highest at the interaction time of 15 μ s and trails off at longer interaction times due to other processes such as spontaneous emission and collisional ionization. The Rydberg atoms can no longer be treated as frozen at longer experimental time scales, and also the radiative lifetime of $34s$ state is only about 30 μ s. In this figure, the $34s$ state populations for interactions with and without the $34d$ state included are presented when averaged over the 34 data sets that were taken for each interaction time. When the first resonance is viewed this way, there does not appear to be much difference in the $34s$ state populations for interactions with and without $34d$ atoms present. This is because the experimental

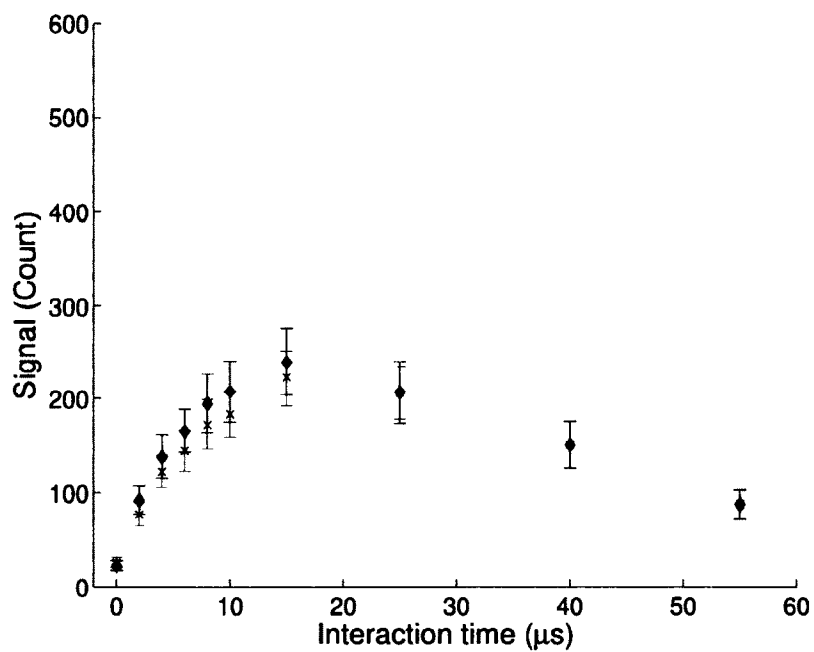


FIG. 41: Interaction time dependence of the $34s$ state population for the resonant energy transfer process $34p_{3/2,|m_j|=1/2} + 34p_{3/2,|m_j|=1/2} \rightarrow 34s_{1/2} + 35s_{1/2}$. The data in the symbol \times is for the process without the $34d$ state atoms included in the interaction, and that in symbol \blacklozenge is for the process with the $34d$ atoms in the interaction.

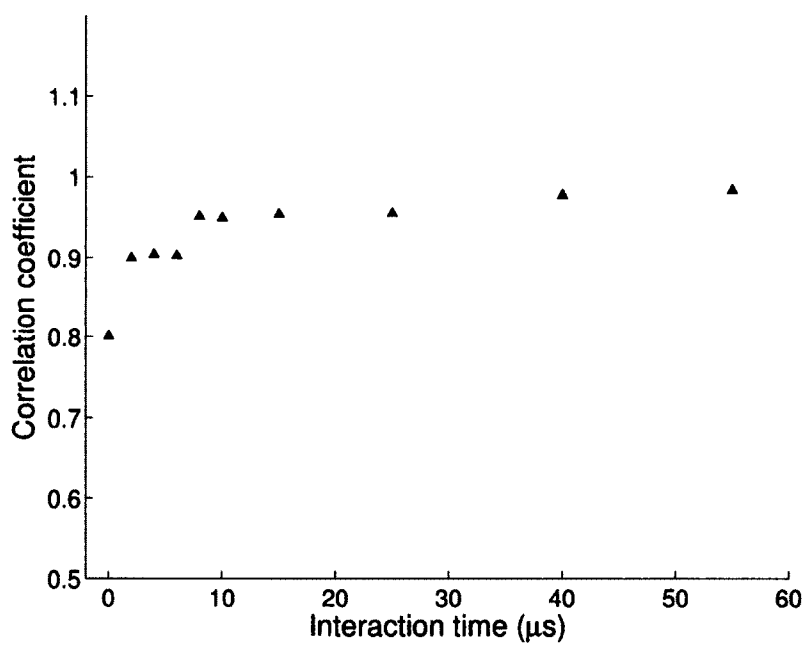


FIG. 42: The correlation coefficient of the $34s$ state population with and without $34d$ included in the interaction vs. interaction time for the resonant energy transfer process $34p_{3/2,|m_j|=1/2} + 34p_{3/2,|m_j|=1/2} \rightarrow 34s_{1/2} + 35s_{1/2}$.

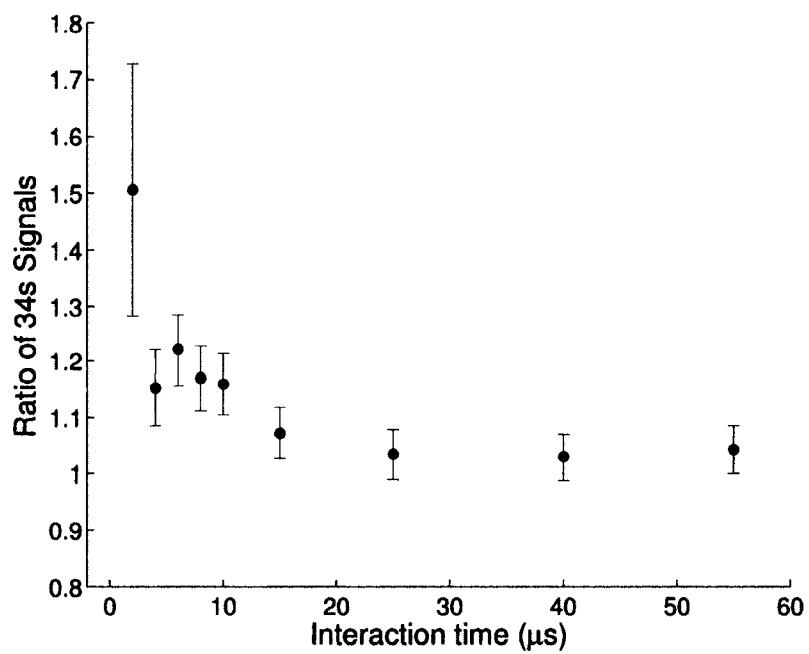


FIG. 43: Ratio of the 34s state population vs. interaction time with and without 34d included in the interaction for the resonant energy transfer process $34p_{3/2,|m_j|=1/2} + 34p_{3/2,|m_j|=1/2} \rightarrow 34s_{1/2} + 35s_{1/2}$.

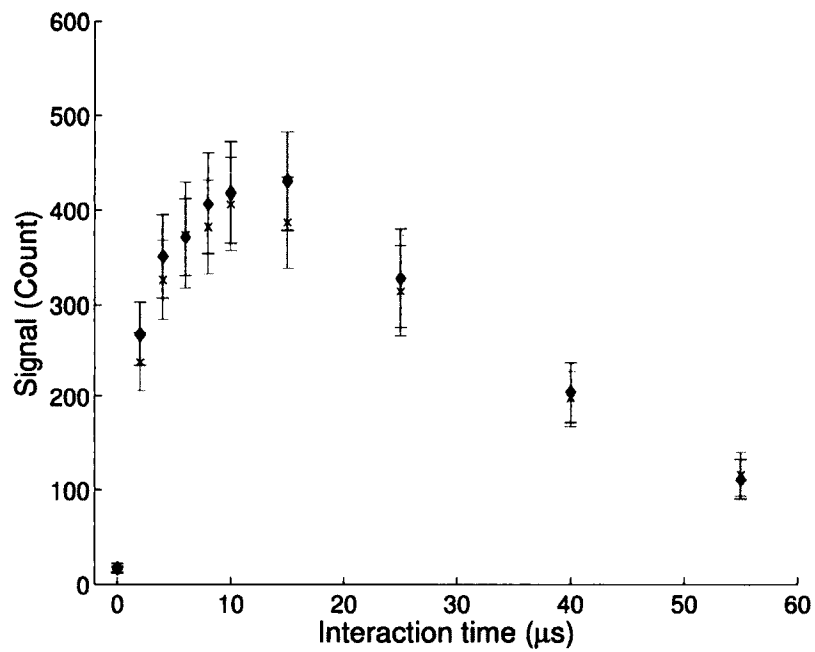


FIG. 44: Interaction time dependence of the $34s$ state population for the resonant energy transfer process $34p_{3/2,|m_j|=3/2} + 34p_{3/2,|m_j|=1/2} \rightarrow 34s_{1/2} + 35s_{1/2}$. The data in the symbol \times is for the process without the $34d$ state atoms included in the interaction, and that in symbol \blacklozenge is for the process with the $34d$ atoms in the interaction.

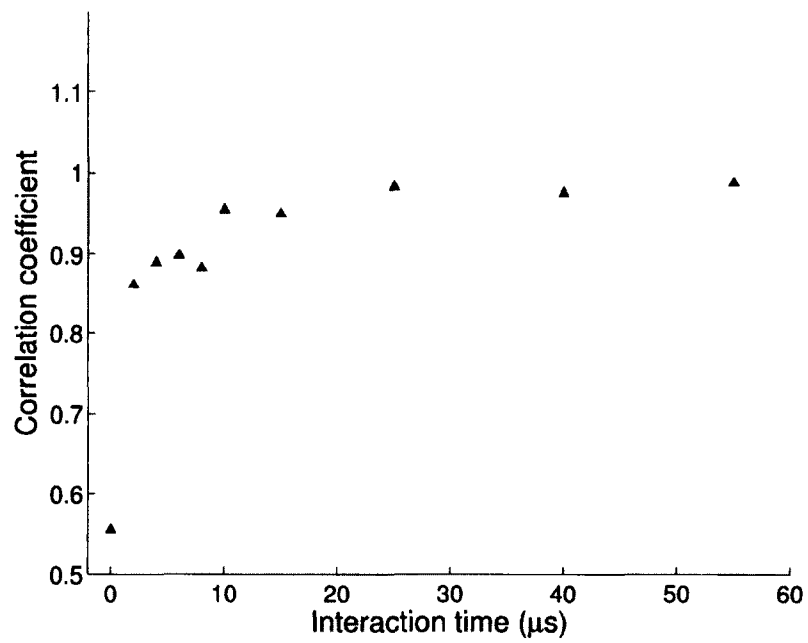


FIG. 45: The correlation coefficient of the $34s$ state population with and without $34d$ included in the interaction vs. interaction time for the resonant energy transfer process $34p_{3/2,|m_j|=3/2} + 34p_{3/2,|m_j|=1/2} \rightarrow 34s_{1/2} + 35s_{1/2}$.

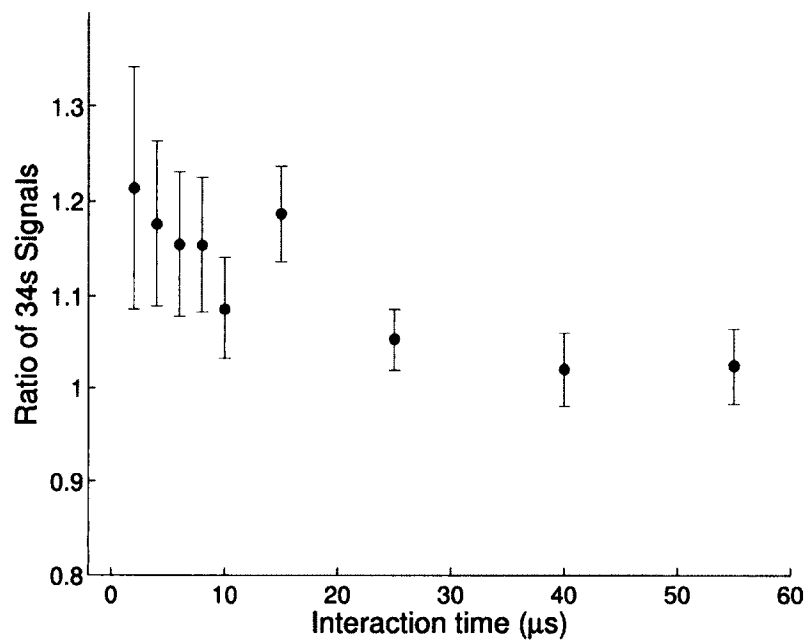


FIG. 46: Ratio of the 34s state population vs. interaction time with and without 34d included in the interaction for the resonant energy transfer process $34p_{3/2,|m_j|=3/2} + 34p_{3/2,|m_j|=1/2} \rightarrow 34s_{1/2} + 35s_{1/2}$.

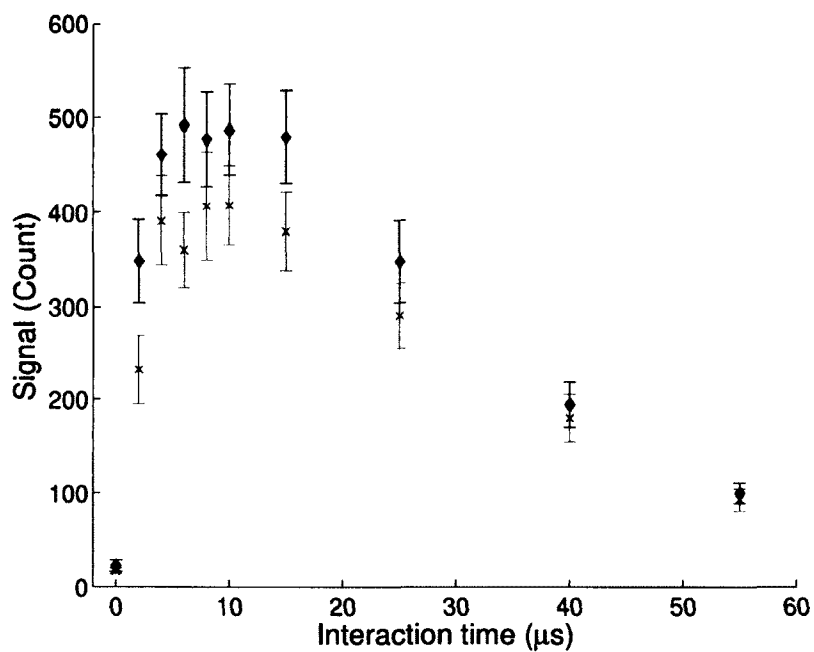


FIG. 47: Interaction time dependence of the $34s$ state population for the resonant energy transfer process $34p_{3/2,|m_j|=3/2} + 34p_{3/2,|m_j|=3/2} \rightarrow 34s_{1/2} + 35s_{1/2}$. The data in the symbol \times is for the process without the $34d$ state atoms included in the interaction, and that in symbol \blacklozenge is for the process with the $34d$ atoms in the interaction.

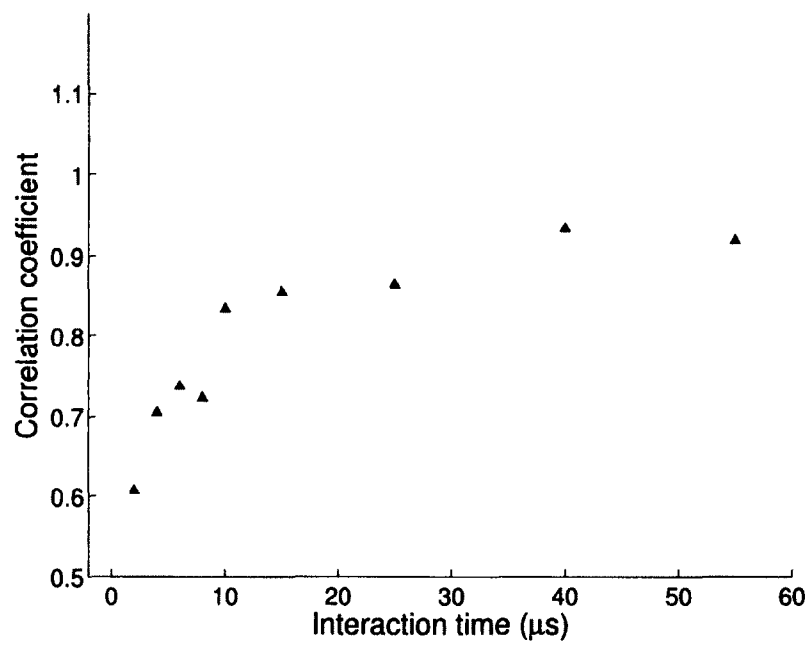


FIG. 48: The correlation coefficient of the 34s state population with and without 34d included in the interaction vs. interaction time for the resonant energy transfer process $34p_{3/2,|m_j|=3/2} + 34p_{3/2,|m_j|=3/2} \rightarrow 34s_{1/2} + 35s_{1/2}$.

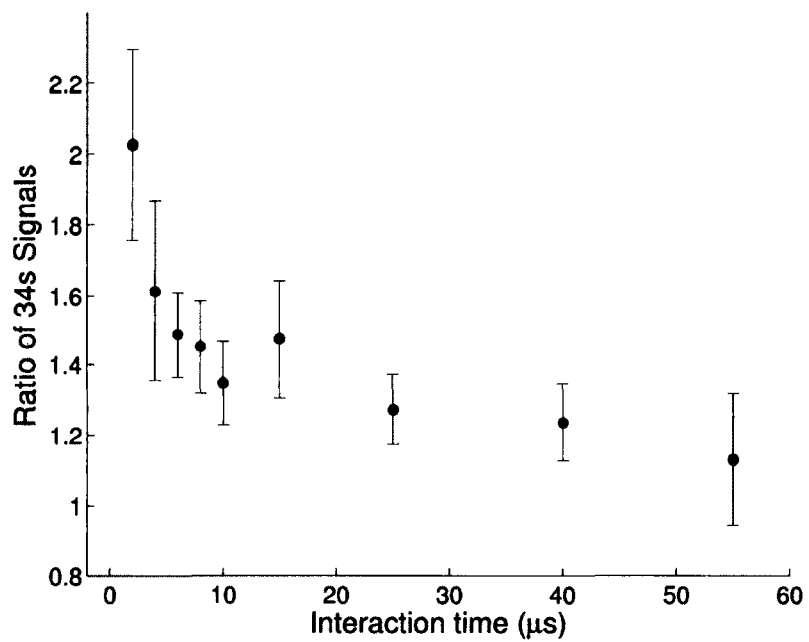


FIG. 49: Ratio of the 34s state population vs. interaction time with and without 34d included in the interaction for the resonant energy transfer process $34p_{3/2,|m_j|=3/2} + 34p_{3/2,|m_j|=3/2} \rightarrow 34s_{1/2} + 35s_{1/2}$.

conditions for each run were not always identical. A more meaningful way to view the data is to compare sets of data (with and without the $34d$ atoms) that were taken back to back where the experimental conditions are the most similar. We do this by taking the ratio of $34s$ atoms with and without the $34d$ atoms for each of the 34 data runs. To verify that there is a direct correlation between these data points, the correlation coefficients were computed for each interaction time. The correlation results are given in Fig. 42, Fig. 45, and Fig. 48. The correlation coefficients are all greater than 0.6 indicating that the data points collected right next to each other are positively correlated.

Once we find the ratio of all pairs of data points, we can then find the average of these ratios and the standard error. The result of such an analysis is given in Fig. 43. The inclusion of $34d$ state atoms in the interaction clearly increases the $34s$ state population by about 20% at shorter interaction times. The results of the experiments for the second and third resonances are given in Fig. 44, Fig. 46, Fig. 47, and Fig. 49. The ratio is much higher for the third resonance. In these analyses, the ratios for the interaction time of 100 ns are omitted because the signals are too small to make meaningful comparison.

4.3 MODELS FOR RESONANT ENERGY TRANSFER PROCESS

In order to simulate the resonant energy transfer process, we have developed simple models that closely follow the models by Westermann et al. [85]. The atoms in these model are fixed in place as is appropriate for the frozen Rydberg gas approximation, and also spontaneous emission, and loss due to ionization are neglected in these models. For the frozen Rydberg gas approximation to be valid, the time scale of only a few μs for the interaction is considered in these models. Amthor et al. have investigated models that take into account of the motion of the atoms [86]. Consider the resonant energy transfer process of a pair of atoms initially in the p state, and the final states of s and s' . The interaction channels are

$$p + p \rightarrow s + s', \quad (46)$$

$$p + s \rightarrow s + p, \text{ and} \quad (47)$$

$$p + s' \rightarrow s' + p. \quad (48)$$

The last two interactions are always resonant energy exchange processes. The basic

states can be expressed in the form $|\psi_1\psi_2\dots\psi_N\rangle$ denoting the state of the atom at position i , where $i = 1, 2, \dots, N$. Each atom can either be in the state p, s or s' . The rule for the basis state is that for every atom in the s state there must be another atom in the s' state since the energy transfer process $p + p \rightarrow s + s'$ produces a pair of s and s' atoms. The basis states for the two-atom model are

$$\begin{aligned} &|pp\rangle, \\ &|ss'\rangle, \text{ and} \\ &|s's\rangle. \end{aligned} \tag{49}$$

These states are coupled by the dipole-dipole interaction, $V_{dd}(R)$. For example,

$$\langle pp|V_{dd}(R)|ss'\rangle = \frac{\mu_1\mu_2}{R^3}, \tag{50}$$

where $\mu_1 = \langle p|r|s\rangle$ and $\mu_2 = \langle p|r|s'\rangle$ are the dipole matrix elements, and R is the distance between the two atoms. Our calculated values of the dipole matrix elements for $\langle 34p|r|34s\rangle = 1100$ and $\langle 34p|r|35s\rangle = 1074$ in atomic units respectively. In the equation (50) we have neglected the angular part of the interaction for our simple model. For the three-atom model, there are a total of seven basis states which are

$$\begin{aligned} &|ppp\rangle, \\ &|pss'\rangle, \\ &|ps's\rangle, \\ &|sps'\rangle, \\ &|s'ps\rangle, \\ &|ss'p\rangle, \text{ and} \\ &|s'sp\rangle. \end{aligned} \tag{51}$$

To find the time evolution of the fraction of s' atoms we numerically solve the time dependent Schrödinger equation.

$$i\hbar\frac{dc_j(t)}{dt} = \sum_k c_k(t)H'_{jk}, \tag{52}$$

where $c_j(t)$ and $c_k(t)$ are the time dependent probability amplitudes for the basis

states $|\phi_j\rangle$ and $|\phi_k\rangle$ respectively, and $H'_{jk} = \langle\phi_j|V_{dd}(R)|\phi_k\rangle$. The time evolution of the fraction of s and s' is obtained by summing the square of the probability amplitudes of the states that contain s and s' pair.

We follow the method of Westermann et al. for selecting the initial positions of the atoms [85]. A thousand atoms are randomly placed in a cube whose length is chosen for setting the desired density. The positions of the three atoms that are closest to the center are picked for the simulation with a three-atom model. It should be noted that this selection method does not give the the closet possible pairs of atoms that contribute with the highest weights in the energy transfer process since the resonant dipole-dipole interaction scales with $1/R^3$. Nevertheless, we have obtained good results with this method since it still selects the atoms closet to the center, and thus somewhat minimizing the distance between the interacting pair of atoms.

The result of the simulations along with the experimental result for the resonant energy transfer process $34p_{3/2,|1/2\rangle} + 34p_{3/2,|1/2\rangle} \rightarrow 34s_{1/2} + 35s_{1/2}$ is given in Fig. 50. We have performed 2000 realizations for each simulation. We have used the three-atom model in our simulation to fit the experimental results because we have found it to be better than the two-atom model in fitting the data. The density of the Rydberg atoms is varied in the simulation, and the amplitude of the experimental data is scaled for fitting. We have found that the results of the simulations are in good agreement with the experimental data. The density parameter used in the simulation for fitting the experimental data for the first resonance is 8.2×10^6 atoms/cm³. The results for the other resonances are given in Fig. 51 and Fig. 52. The density parameters used in the simulations are 2.3×10^7 atoms/cm³ and 2.5×10^7 atoms/cm³ respectively. The simulation results for the interaction time dependence of the population of 34s atoms for different Rydberg densities are given in Fig. 53.

In our three-atom model angular dependence of the dipole-dipole interaction is neglected. The next immediate step in refining the model would be to include the angular dependence of the interaction. The model can also be extended to include more atoms, a six-atom model for example. Most importantly, models that take account of $34d$ state atoms in the interaction are needed for simulating the observed catalysis effect. Such models are currently being developed starting with a three-atom model in which two atoms are in the p state and one atom is in the d state initially. A four-atom model in which two atoms are in the p state and two atoms are in the d state initially is also is being developed.

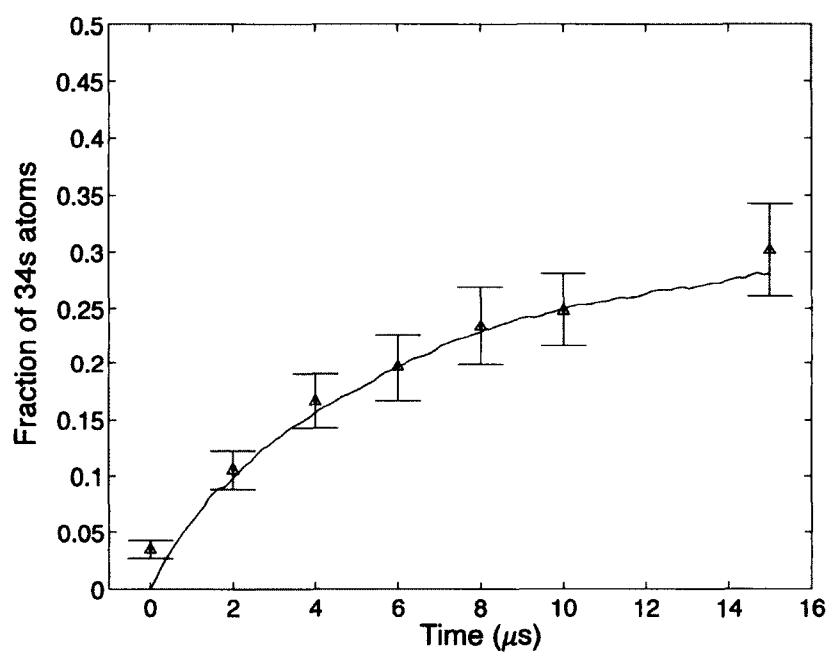


FIG. 50: The experimental and simulation results for the time evolution of the fraction of $34s$ atoms for the energy transfer process $34p_{3/2,|m_j|=1/2} + 34p_{3/2,|m_j|=1/2} \rightarrow 34s_{1/2} + 35s_{1/2}$. The amplitude of the experimental data is scaled to fit.

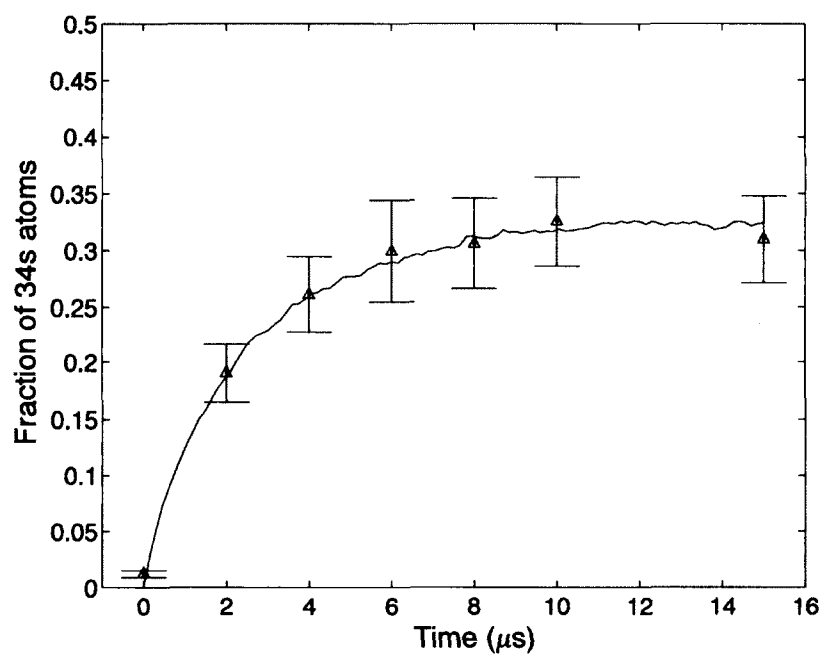


FIG. 51: The experimental and simulation results for the time evolution of the fraction of $34s$ atoms for the energy transfer process $34p_{3/2,|m_j|=3/2} + 34p_{3/2,|m_j|=1/2} \rightarrow 34s_{1/2} + 35s_{1/2}$. The amplitude of the experimental data is scaled to fit.

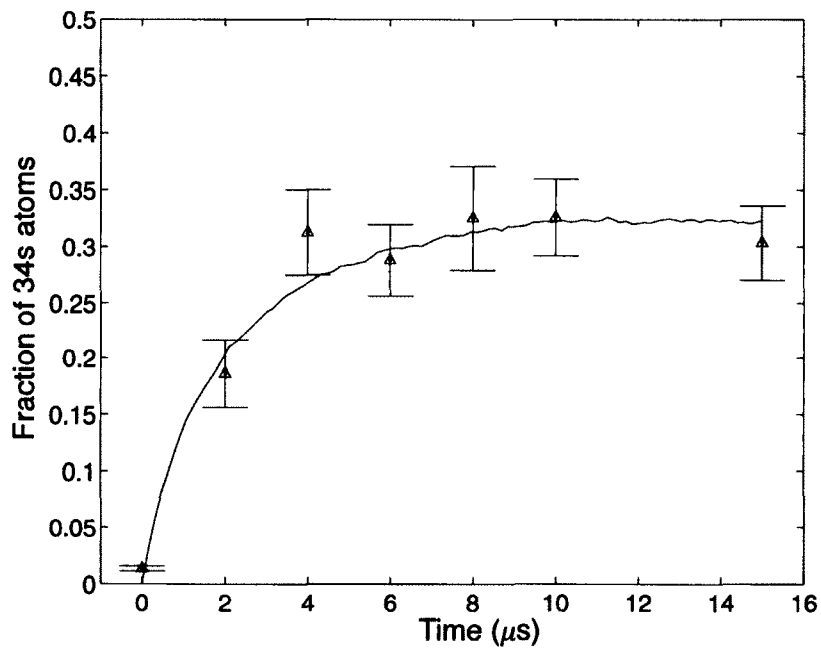


FIG. 52: The experimental and simulation results for the time evolution of the fraction of $34s$ atoms for the energy transfer process $34p_{3/2,|m_j|=3/2} + 34p_{3/2,|m_j|=3/2} \rightarrow 34s_{1/2} + 35s_{1/2}$. The amplitude of the experimental data is scaled to fit.

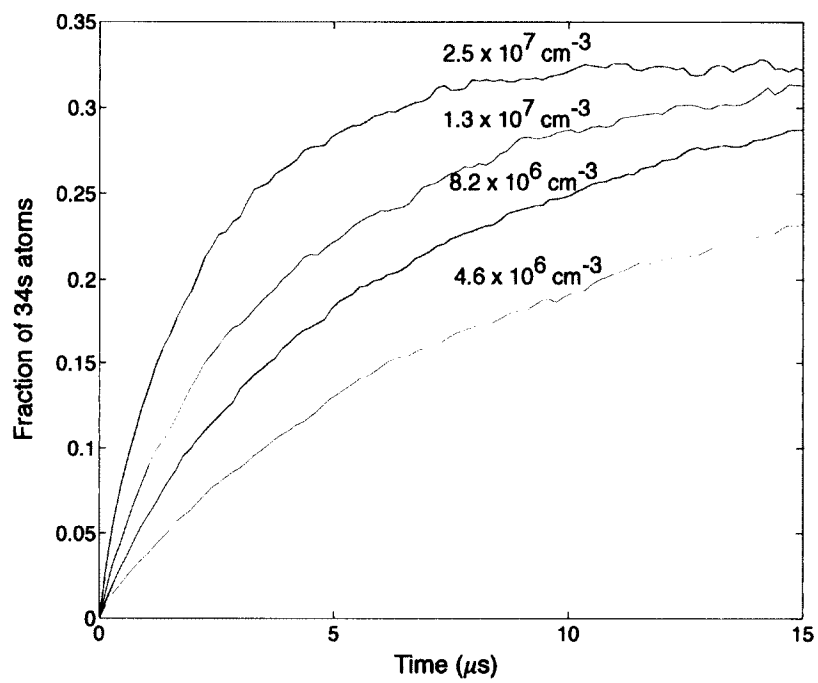


FIG. 53: Interaction time dependence of the population of 34s atoms for different Rydberg densities with the three-atom model.

CHAPTER 5

CONCLUSION AND OUTLOOK

In this dissertation we present the study of the catalysis effect of Rydberg atoms that do not directly participate in the resonant energy transfer interactions. We have investigated the Förster process of $34p + 34p \rightarrow 34s + 35s$, and observed Stark-tuned Förster resonances for different m_j values. When the $34d$ state atoms were included in the interaction, we observed an increase in $34s$ state population. While the $34d$ state does not participate in the process of $34p + 34p \rightarrow 34s + 35s$, it introduces an interaction channel that is resonant for all electric fields: $34p + 34d \rightarrow 34d + 34p$. We have also investigated the time dependence of the resonant interactions, and the experimental results are compared with numerical simulations with simple models that takes into account of always resonant interaction channels. The models use a frozen Rydberg gas approximation for the experimental time scales of a few μs . The simulation results are in good agreement with the experimental results for the interaction without $34d$ state atoms included. We have found that a three-atom model with all atoms initially in p state gives a better fit for the experimental results than a two-atom model. We are currently working on incorporating d state atoms into the model, and also on including more basis states in the current model.

We have described the setup of the experimental apparatus, along with the characterization of the dye lasers used in exciting atoms to desired Rydberg states, and the experimental timing sequences. Detection methods for Rydberg atoms have been discussed and the details of installing an ion detection system in the vacuum chamber have been given. Experiments on Rydberg spectroscopy have been performed both with the fluorescence detection of the trap loss and the ion detection with the field ionization method, and found that the results are in good agreement with the NIST atomic spectra database.

One possible future experiment is to investigate the catalysis effect with different states other than $34d$ state. For example, $33d$ state can be used as the catalyst state instead. The coupling strength of the always resonant interaction is now different. One can, therefore, investigate the coupling strength dependence of the catalysis effect.

BIBLIOGRAPHY

- [1] T. Gallagher, L. Humphrey, W. Cooke, R. Hill, and S. Edelstein, *Phys. Rev. A* **16**, 1098 (1977).
- [2] J. M. Raimond, G. Vitrant, and S. Haroche, *Journal of Physics B: Atomic and Molecular Physics* **14**, L655 (1981).
- [3] V. Sandoghdar, C. I. Sukenik, E. A. Hinds, and S. Haroche, *Phys. Rev. Lett.* **68**, 3432 (1992).
- [4] K. A. Safinya, J. F. Delpech, F. Gounand, W. Sandner, and T. F. Gallagher, *Phys. Rev. Lett.* **47**, 405 (1981).
- [5] R. Kachru, N. H. Tran, and T. F. Gallagher, *Phys. Rev. Lett.* **49**, 191 (1982).
- [6] R. C. Stoneman, M. D. Adams, and T. F. Gallagher, *Phys. Rev. Lett.* **58**, 1324 (1987).
- [7] T. Hänsch and A. Schawlow, *Optics Communications* **13**, 68 (1975).
- [8] D. J. Wineland and H. Dehmelt, *Bull. Am. Phys. Soc.* **20**, 637 (1975).
- [9] E. L. Raab, M. Prentiss, A. Cable, S. Chu, and D. E. Pritchard, *Phys. Rev. Lett.* **59**, 2631 (1987).
- [10] M. H. Anderson, J. R. Ensher, M. R. Matthews, C. E. Wieman, and E. A. Cornell, *Science* **269**, 198 (1995).
- [11] J. Miao, J. Hostetter, G. Stratis, and M. Saffman, *Phys. Rev. A* **89**, 041401 (2014).
- [12] B. DeMarco and D. Jin, *Science* **285** (1999).
- [13] M. Lu, N. Q. Burdick, S. H. Youn, and B. L. Lev, *Phys. Rev. Lett.* **107**, 190401 (2011).
- [14] M. Lu, N. Q. Burdick, and B. L. Lev, *Phys. Rev. Lett.* **108**, 215301 (2012).
- [15] K. Aikawa, A. Frisch, M. Mark, S. Baier, A. Rietzler, R. Grimm, and F. Ferlaino, *Phys. Rev. Lett.* **108**, 210401 (2012).

- [16] K. Aikawa, A. Frisch, M. Mark, S. Baier, R. Grimm, and F. Ferlaino, *Phys. Rev. Lett.* **112**, 010404 (2014).
- [17] T. G. Walker and M. Saffman, *Journal of Physics B: Atomic, Molecular and Optical Physics* **38**, S309 (2005).
- [18] T. Ritz, A. Damjanović, and K. Schulten, *ChemPhysChem* **3**, 243 (2002).
- [19] T. Förster, *Annalen der Physik* **437**, 55 (1948).
- [20] W. R. Anderson, J. R. Veale, and T. F. Gallagher, *Phys. Rev. Lett.* **80**, 249 (1998).
- [21] A. Reinhard, K. C. Younge, and G. Raithel, *Phys. Rev. A* **78**, 060702 (2008).
- [22] I. I. Ryabtsev, D. B. Tretyakov, I. I. Beterov, and V. M. Entin, *Phys. Rev. Lett.* **104**, 073003 (2010).
- [23] E. Altieri, D. P. Fahey, M. W. Noel, R. J. Smith, and T. J. Carroll, *Phys. Rev. A* **84**, 053431 (2011).
- [24] Y. Yu, H. Park, and T. F. Gallagher, *Phys. Rev. Lett.* **111**, 173001 (2013).
- [25] P. Bohlouli-Zanjani, J. A. Petrus, and J. D. D. Martin, *Phys. Rev. Lett.* **98**, 203005 (2007).
- [26] D. B. Tretyakov, V. M. Entin, E. A. Yakshina, I. I. Beterov, C. Andreeva, and I. I. Ryabtsev, *Phys. Rev. A* **90**, 041403 (2014).
- [27] I. Mourachko, D. Comparat, F. de Tomasi, A. Fioretti, P. Nosbaum, V. M. Akulin, and P. Pillet, *Phys. Rev. Lett.* **80**, 253 (1998).
- [28] I. Mourachko, W. Li, and T. F. Gallagher, *Phys. Rev. A* **70**, 031401 (2004).
- [29] W. R. Anderson, M. P. Robinson, J. D. D. Martin, and T. F. Gallagher, *Phys. Rev. A* **65**, 063404 (2002).
- [30] T. J. Carroll, S. Sunder, and M. W. Noel, *Phys. Rev. A* **73**, 032725 (2006).
- [31] J. Han, *Phys. Rev. A* **82**, 052501 (2010).

- [32] J. H. Gurian, P. Cheinet, P. Huillery, A. Fioretti, J. Zhao, P. L. Gould, D. Comparat, and P. Pillet, *Phys. Rev. Lett.* **108**, 023005 (2012).
- [33] D. P. DiVincenzo, *Science* **270**, 255 (1995).
- [34] D. Jaksch, J. I. Cirac, P. Zoller, S. L. Rolston, R. Côté, and M. D. Lukin, *Phys. Rev. Lett.* **85**, 2208 (2000).
- [35] M. Lukin, M. Fleischhauer, R. Cote, L. Duan, D. Jaksch, J. Cirac, and P. Zoller, *Phys. Rev. Lett.* **87**, 037901 (2001).
- [36] M. Saffman, T. G. Walker, and K. Mølmer, *Rev. Mod. Phys.* **82**, 2313 (2010).
- [37] D. Tong, S. M. Farooqi, J. Stanojevic, S. Krishnan, Y. P. Zhang, R. Côté, E. E. Eyler, and P. L. Gould, *Phys. Rev. Lett.* **93**, 063001 (2004).
- [38] K. Singer, M. Reetz-Lamour, T. Amthor, L. Marcassa, and M. Weidemüller, *Phys. Rev. Lett.* **93**, 163001 (2004).
- [39] T. Vogt, M. Viteau, A. Chotia, J. Zhao, D. Comparat, and P. Pillet, *Phys. Rev. Lett.* **99**, 073002 (2007).
- [40] R. Heidemann, U. Raitzsch, V. Bendkowsky, B. Butscher, R. Löw, L. Santos, and T. Pfau, *Phys. Rev. Lett.* **99**, 163601 (2007).
- [41] A. Gaetan, Y. Miroshnychenko, T. Wilk, A. Chotia, M. Viteau, D. Comparat, P. Pillet, A. Browaeys, and P. Grangier, *Nat Phys* **5**, 115 (2009).
- [42] E. Urban, T. A. Johnson, T. Henage, L. Isenhower, D. D. Yavuz, T. G. Walker, and M. Saffman, *Nat Phys* **5**, 110 (2009).
- [43] L. Isenhower, E. Urban, X. L. Zhang, A. T. Gill, T. Henage, T. A. Johnson, T. G. Walker, and M. Saffman, *Phys. Rev. Lett.* **104**, 010503 (2010).
- [44] T. C. Killian, S. Kulin, S. D. Bergeson, L. A. Orozco, C. Orzel, and S. L. Rolston, *Phys. Rev. Lett.* **83**, 4776 (1999).
- [45] T. C. Killian, Y. C. Chen, P. Gupta, S. Laha, Y. N. Martinez, P. G. Mickelson, S. B. Nagel, A. D. Saenz, and C. E. Simien, *Plasma Physics and Controlled Fusion* **47**, 5A (2005).

- [46] E. A. Cummings, J. E. Daily, D. S. Durfee, and S. D. Bergeson, *Phys. Rev. Lett.* **95**, 235001 (2005).
- [47] M. S. Murillo, *Phys. Rev. Lett.* **87**, 115003 (2001).
- [48] C. E. Simien, Y. C. Chen, P. Gupta, S. Laha, Y. N. Martinez, P. G. Mickelson, S. B. Nagel, and T. C. Killian, *Phys. Rev. Lett.* **92**, 143001 (2004).
- [49] S. D. Bergeson, A. Denning, M. Lyon, and F. Robicheaux, *Phys. Rev. A* **83**, 023409 (2011).
- [50] M. P. Robinson, B. L. Tolra, M. W. Noel, T. F. Gallagher, and P. Pillet, *Phys. Rev. Lett.* **85**, 4466 (2000).
- [51] W. Li, M. W. Noel, M. P. Robinson, P. J. Tanner, T. F. Gallagher, D. Comparat, B. Laburthe Tolra, N. Vanhaecke, T. Vogt, N. Zahzam, P. Pillet, and D. A. Tate, *Phys. Rev. A* **70**, 042713 (2004).
- [52] T. Amthor, M. Reetz-Lamour, S. Westermann, J. Denskat, and M. Weidemüller, *Phys. Rev. Lett.* **98**, 023004 (2007).
- [53] T. F. Gallagher, *Rydberg Atoms* (Cambridge University Press, 1994).
- [54] W. Li, I. Mourachko, M. W. Noel, and T. F. Gallagher, *Phys. Rev. A* **67**, 052502 (2003).
- [55] J. Han, Y. Jamil, D. V. L. Norum, P. J. Tanner, and T. F. Gallagher, *Phys. Rev. A* **74**, 054502 (2006).
- [56] N. Bohr, *Philosophical Magazine* **26**, 1 (1913).
- [57] P. J. Mohr, B. N. Taylor, and D. B. Newell, *Rev. Mod. Phys.* **80**, 633 (2008).
- [58] M. Zimmerman, M. Littman, M. Kash, and D. Kleppner, *Phys. Rev. A* **20**, 2251 (1979).
- [59] J. D. Pritchard, *Cooperative Optical Non-linearity in a blockaded Rydberg Ensemble*, Ph.D. thesis, Durham University (2011).
- [60] E. Schrödinger, *Phys. Rev.* **28**, 1049 (1926).

- [61] M. Marinescu, H. R. Sadeghpour, and A. Dalgarno, *Phys. Rev. A* **49**, 982 (1994).
- [62] C. E. Theodosiou, *Phys. Rev. A* **30**, 2881 (1984).
- [63] S. A. Bhatti, C. L. Cromer, and W. E. Cooke, *Phys. Rev. A* **24**, 161 (1981).
- [64] B. V. Numerov, *MNRAS* **84**, 592 (1924).
- [65] M. Weissbluth, *Atoms and Molecules* (Academic Press, 1978).
- [66] C. J. Foot, *Atomic Physics*, Oxford Master Series in Physics (Oxford University Press, 2005).
- [67] T. G. Walker and M. Saffman, *Phys. Rev. A* **77**, 032723 (2008).
- [68] C. Cohen-Tannoudji, B. Diu, and F. Laloë, *Quantum Mechanics*, Vol. 2 (John Wiley & Sons, 1977).
- [69] H. J. Metcalf and P. van der Straten, *Laser Cooling and Trapping* (Springer, 1999).
- [70] D. J. Wineland and W. M. Itano, *Phys. Rev. A* **20**, 1521 (1979).
- [71] S. Chu, L. Hollberg, J. E. Bjorkholm, A. Cable, and A. Ashkin, *Phys. Rev. Lett.* **55**, 48 (1985).
- [72] P. D. Lett, R. N. Watts, C. I. Westbrook, W. D. Phillips, P. L. Gould, and H. J. Metcalf, *Phys. Rev. Lett.* **61**, 169 (1988).
- [73] J. Dalibard and C. Cohen-Tannoudji, *J. Opt. Soc. Am. B* **6**, 2023 (1989).
- [74] D. A. Steck, <http://steck.us/alkalidata/> (2013).
- [75] C. E. Wieman, G. Glowers, and S. Gilbert, *American Journal of Physics* **63**, 317 (1995).
- [76] M. G. Littman and H. J. Metcalf, *Appl. Opt.* **17** (1978).
- [77] K. Harvey and C. J. Myatt, *Optics Letters* **16** (1991).
- [78] S.-Q. Shang and H. J. Metcalf, *Appl. Opt.* **28**, 1618 (1989).

- [79] W. Demtröder, *Laser Spectroscopy*, 3rd ed. (Springer, 2003).
- [80] K. B. MacAdam, A. Steinbach, and C. E. Wieman, *American Journal of Physics* **60**, 1098 (1992).
- [81] M. Minarni, *Investigation of ultracold Rb atoms in a pulsed far off resonance trap*, Ph.D. thesis, Old Dominion University (2006).
- [82] G. Ranjit, *Experimental investigation of long-lived "ZEKE" Rydberg states in ultracold argon*, Ph.D. thesis, Old Dominion University (2010).
- [83] W. Cooke and T. Gallagher, *Phys. Rev. A* **17**, 1226 (1978).
- [84] M. Viteau, A. Chotia, D. Comparat, D. A. Tate, T. F. Gallagher, and P. Pillet, *Phys. Rev. A* **78**, 040704 (2008).
- [85] S. Westermann, T. Amthor, A. d. Oliveirab, J. Deiglmayr, M. Reetz-Lamour, and M. Weidemüller, *Eur. Phys. J. D* **40**, 37 (2006).
- [86] T. Amthor, M. Reetz-Lamour, C. Giese, and M. Weidemüller, *Phys. Rev. A* **76**, 054702 (2007).

VITA

Aye Lu Win
Department of Physics
Old Dominion University
Norfolk, VA 23529

EDUCATION:

Ph.D., Physics, Old Dominion University, May 2015
M.S., Physics, Old Dominion University, May 2008
B.A., Mathematics and Physics, Simpson College, May 2005

PUBLICATION:

“Multiple light scattering on the $F = 1 \rightarrow F' = 0$ transition in a cold and high density ^{87}Rb vapor”, *Journal of Modern Optics*, 61, S. Balik, A.L. Win, and M.D. Havey, 77-84 (2014).

“Near-resonance light scattering from a high-density ultracold atomic ^{87}Rb gas”, S. Balik, A.L. Win, and M.D. Havey, *Physical Review A* 87, 053817 (2013).

“Imaging-based parametric resonance in an optical dipole atom trap”, S. Balik, A.L. Win, and M.D. Havey, *Physical Review A* 80, 023404 (2009).

“Catalysis of Stark-tuned interactions between ultracold Rydberg atoms”, A.L. Win, W.D. Williams, and C.I. Sukenik, in preparation.